Electric Field Measurements in the Vicinity of an ICRF Antenna

Ana Kostic

Doctoral dissertation submitted to obtain the academic degrees of
Doctor of Engineering Physics (UGent) and Doctor Rerum Naturalium (LMU München)

Supervisors

Prof. Kristel Crombé, PhD* - Prof. Hartmut Zohm, PhD** - Prof. Jean-Marie Noterdaeme, PhD***

* Department of Applied Physics
Faculty of Engineering and Architecture, Ghent University

** Ludwig-Maximilians-Universität München, Germany

***Department of Electromechanical, Systems and Metal Engineering
Faculty of Engineering and Architecture, Ghent University

April 2021

GHENT UNIVERSITY

LMU LUDWIG-MAXIMILIANS-UNIVERSITÄT MÜNCHEN

ISBN 978-94-6355-475-6
NUR 926, 924
Wettelijk depot: D/2021/10.500/24

Members of the Examination Board

Chairs

Prof. Patrick De Baets, PhD, Ghent University
Prof. Jörg Schreiber, PhD, Ludwig-Maximilians-Universität München, Germany

Other members entitled to vote

Prof. Otmar Biebel, PhD, Ludwig-Maximilians-Universität München, Germany
Prof. Wolfgang Biel, PhD, Ghent University
Prof. Stéphane Heuraux, PhD, Université de Lorraine, France
Prof. Gregor Morfill, PhD, terraplasma GmbH & Max Planck Institute for Extraterrestrial Physics & Ludwig-Maximilians-Universität München, Germany
Thomas Puetterich, PhD, Ludwig-Maximilians-Universität München, Germany

Supervisors

Prof. Kristel Crombé, PhD, Ghent University
Prof. Hartmut Zohm, PhD, Ludwig-Maximilians-Universität München, Germany

This research was performed at:

Max Planck Institute for Plasma Physics
Boltzmannstraße 2
85748 Garching, Germany

In collaboration with:

Ghent University
Faculty of Engineering and Architecture
Department of Applied Physics
Sint-Pietersnieuwstraat 41
9000 Ghent, Belgium

Ludwig-Maximilians-Universität München
Faculty of Physics
Geschwister-Scholl-Platz 1
80539 München, Germany

FUSION-DC - International Doctoral
College in Fusion Science and Engineering
Erasmus Mundus Programme
Coordinated by Ghent University

Research Foundation - Flanders (FWO)

Date of the first oral exam (private defence at Ludwig-Maximilians-Universität München): 10.03.2021.
Date of the second oral exam (public defence at Ghent University): 13.04.2021.

Date of the thesis submission at Ludwig-Maximilians-Universität München: 27.01.2021.
Date of the thesis submission at Ghent University: 13.01.2021.

Acknowledgement

I gratefully acknowledge the funding received towards my PhD thesis project - this research has been carried out within the framework of the EUROfusion Consortium and has received funding from the Euratom research and training programme 2014-2018 and 2019-2020 under Grant Agreement No. 633053. This work was also supported by the Research Foundation - Flanders (FWO), with Project No. G0B3115N, and the FUSION-DC scholarship grant.

I wish to thank the members of the thesis examination committee who have dedicated their time to challenge this work, which has significantly stimulated its improvement.

I would also like to extend my deepest gratitude to my academic advisers, Prof. Kristel Crombé, Prof. Jean-Marie Noterdaeme and Prof. Hartmut Zohm for their guidance, unparalleled support and patience that cannot be underestimated.

This thesis was done at the Max Planck Institute for Plasma Physics (IPP) in Garching, and it would not have been possible without the supervision and help from the local scientists. I would like to thank to Dr. Ralph Dux and Dr. Michael Griener, for their incredible patience with me, but above all for sharing their extensive knowledge in the field of optics and plasma spectroscopy. For the scientific discussions on all matters wave and edge plasma related, for brainstorming about the best approaches I should study, and for an overall positive experience during my PhD I would like to thank to the members of the ICRF group at IPP - Dr. Roman Ochoukov, Dr. Vladimir Bobkov, Dr. Wouter Tierens, Dr. Mari Usoltsceva, Dr. Guillermo Suarez Lopez, Dr. Wei Zhang, and Ricacardo Cassagrande. For making sure IShTAR runs smoothly and for helping materialise my visions I thank Dr. Ilya Sestrikov, Herr Friderich Fischer, Herr Gerhard Siegl, Dr. Helmut Faugel, Herr Helmut Fuenfgelder and Herr Fabian Riedl.

Collaboration with colleagues abroad has made it possible to complete this work within a specific timeframe. Having EZSSS code at hand made everything easier, and so my heartfelt thanks go to the colleagues from the Oak Ridge National Laboratory - Dr. Elijah Martin and Dr. Abdullah Zafar. I would like to thank Dr Anton Nikiforov of the Ghent University and Prof. Milorad Kuraica, Ms. Nora Trklja i Mr. Ivan Krstic of the University of Belgrade for generously sharing their knowledge and experience on the measurement of electric fields in Grimm-(and similar) type of glow plasma discharges.

The cover illustration is designed by Milan Maksimovic and represents a unique graphical abstract of this work.

To my family.

Table of Contents

List of Figures

List of Tables

Nederlandse samenvatting –Summary in Dutch–

Efficiënte concepten voor fusiereactoren moeten in de eerste plaats voldoen aan de basiscriteria die door kernfusieprocessen worden opgelegd. Deze criteria houden in dat, om de ontstekingsomstandigheden in een tokamakreactor te bereiken, Ohmse verwarming niet voldoende is en dat er extra verwarmingsvermogen aan het plasma moet worden geleverd. Één van de methoden met het meest experimentele succes bij het verhitten van tokamakplasma's is gebaseerd op de resonante absorptie van golven in het Ioncyclotron frequentiebereik binnen een fundamentele (of de harmonische) cyclotronlaag van de ionensoort in de kern van het plasma. Dit is de ICRF-verwarming.

Om de voortplanting van de gunstige golfmodus binnen dit frequentiebereik (de *Fast Wave*) te garanderen, moet de ICRF-antenne in het vacuümvat van de tokamak, aan de wand en dicht bij de rand van het opgesloten plasma geplaatst worden. Dit introduceert het contactgebied tussen de antenne en het randplasma, wat leidt tot antenne - plasma interacties die resulteren in bepaalde ongewenste effecten op de werking van de antenne. De schadelijke neveneffecten, zoals de toegenomen creatie van de onzuiverheden uit de wand (antenne limiters), vermogensdissipatie, hot-spots op de materiële oppervlakken van de antenne, werden experimenteel waargenomen in verschillende tokamaks. Om deze te beperken werden de verwarmingsscenario's en de antenneontwerpen verbeterd. Echter, een fundamenteel begrip van de processen die plaatsvinden binnen dit interactiegebied is noodzakelijk voor een goede theoretische behandeling, betrouwbare zelf-consistente simulaties en daarmee een veiliger ontwerp van de ICRF-ontlading en het ICRF-systeem voor de lange-puls plasma experimenten met hoog vermogen.

Deze neveneffecten worden toegeschreven aan de door RF geïnduceerde modificatie van de plasma grenslaag (*plasma sheath*) de naar het plasma gerichte oppervlakken van de ICRF-antenne. Zodra het plasma een vast oppervlak (een tegel, een begrenzer) tegenkomt, vormt zich een dun gebied dat slechts enkele elektronen-Debye-lengtes breed is daartussen. Dit is de zogenaamde *plasma sheath*, die gelijke deeltjesfluxen uit het plasma garandeert en de ladingsambipolariteit te behoudt door ionen uit het plasma te versnellen en de elektronen af te remmen. In het kader van het ICRF-onderzoek en de genoemde neveneffecten van de ICRF-werking worden de effecten van de *plasma sheath*, met name de DC-potentiaaldaling over de *sheath*, versterkt door de RF-modu-

latie. Vanwege de enorm verschillende ruimtelijke schalen die nodig zijn om zowel de dynamiek van de grenslaag als de golfpropagatie en de koppeling met het randplasma vast te leggen, laten de theoretische RF-modelleringscodes de eerste weg en vervangen ze de RF-*sheath* doorgaans door een randvoorwaarde die equivalent is met een dunne vacuümlaag met een bepaalde capaciteit. De effecten van de RF gemoduleerde rand worden indirect in aanmerking genomen, en de randpotentiaal wordt bekeken vanaf de plasmakant. De ontbrekende stap in deze procedure is het vergelijken van de resultaten van een dergelijke theoretische benadering met de eigenlijke werking van de antenne en het testen van de validiteit van de aannames in de afleiding van de randvoorwaarden. Hiervoor is een speciale diagnostische apparatuur nodig.

Het doel van deze dissertatie is het ontwikkelen van een specifieke diagnostische apparatuur voor het meten van elektrische velden in de RF gemoduleerde *sheaths* van de plasma-georiënteerde structuren van de ICRF-antenne. De bijzondere moeilijkheden hierbij zijn dat een dergelijke diagnose niet invasief mag zijn, terwijl ook rekening moet worden gehouden met het feit dat de gemiddelde dikte van de *sheath* tussen enkele mm en enkele cm ligt, het moet elektrische velden detecteren binnen het bereik van $0-10\,\mathrm{kV\,cm^{-1}}$, in lage druk (onder 5 Pa) en lage dichtheid (onder $10^{18}\,\mathrm{m^{-3}}$) ontladingsomstandigheden die worden aangetroffen in de onmiddellijke nabijheid van een ICRF-antenne aan de periferie van het tokamakplasma.

Dit onderzoek werd uitgevoerd op IShTAR, een proefopstelling gewijd aan experimentele studies van de interactie tussen de antenne en het plasma. Dit toestel biedt de mogelijkheid om de golven die gelanceerd worden vanaf de ICRF-antenne te koppelen aan een plasma dat representatief is voor de golven die in de nabijheid van de ICRF-antennes in tokamaks worden aangetroffen, zij het in een eenvoudigere configuratie en met een betere diagnostische toegang.

In overeenstemming met de eisen die aan de diagnostiek worden gesteld, wordt gekozen voor optische emissiespectroscopie, een niet-invasieve diagnosetechniek. De elektrische veldvector wordt uit de gemeten spectra geëxtraheerd door de experimenteel geregistreerde verschuiving van de spectrale lijn te vergelijken met de theoretische modellen die gebaseerd zijn op de atoom- en quantumtheorie van het Stark-effect. De theoretische berekening van de atoomstructuur, en de resulterende vorm en golflengte van de spectrale lijn als gevolg van het externe elektrische veld zijn uitgevoerd met behulp van de EZSSS-code (Explicit Zeeman Stark Spectral Simulator), die ook rekening kan houden met de effecten die worden veroorzaakt door een statisch, eenzijdig magnetisch veld (het Zeeman-effect). De golflengteverschuiving van de heliumlijn met 447 nm golflengte, wat overeenkomt met de 4^3D - 2^3P overgang van het neutraal heliumatoom, is de belangrijkste diagnostische parameter.

Deze specifieke parameter en de spectraallijn werden gekozen op basis van de beperkingen van het apparaat en de beperkingen die voortvloeien uit de plasma-omgeving die gunstig is voor experimenteel onderzoek van de ICRF-antenne - plasmarand-interacties. De beperkingen waarmee rekening is gehouden, zijn de volgende. IShTAR kan werken met helium en argon. Het Stark-

effect, d.w.z. de correctie van de veldvrije niet-geperturbeerde atoomenergieniveaus, is gemakkelijker quantummechanisch te behandelen voor helium. In de spectra van helium worden de overgangen van de bovenste toestanden met het "hoofdquantumgeta gelijk of lager dan 3 geacht ongevoelig te zijn voor het elektrisch veld, terwijl voor de bovenste toestanden met $n \geq 4$ alleen de hoge quantumgetallen van het totale impulsmoment behouden moeten blijven (P, D, F)". (W. Hicks). Tenslotte werd de heliumlijn met 447 nm golflengte gevonden als de optimale balans tussen deze voorwaarden, de signaalsterkte zoals gemeten in IShTAR plasma's in de buurt van de antenne, en de detectiemogelijkheden van de spectrometer die gebruikt wordt voor de diagnostische doeleinden. De verschuiving van de spectraallijn vanuit de niet-geperturbeerde positie is de diagnostische parameter bij uitstek, aangezien de andere potentiële diagnostische parameters die vaak worden gebruikt in de Stark spectroscopie van heliumatomen ontoegankelijk zijn onder de ontladingsomstandigheden die zich voordoen in de directe omgeving van een ICRF-antenne. Bovendien is deze parameter niet afhankelijk van het instrument, zodat hij kan worden gebruikt om de resultaten van verschillende experimenten te vergelijken.

In IShTAR zijn twee diagnostische schema's ontwikkeld. Het ene schema laat toe om het volumegeïntegreerde elektrische veld te meten in de *sheath* van de DC-elektrode (dat in dit werk als proof of concept diende), en in het grensgebied van de ICRF-antennebox (aangezien dergelijke gegevens nuttig zijn voor de experimentele vergelijking van de theoretische behandeling van de interactie tussen de antenne en het plasma). Dit gebeurt met behulp van passieve optische emissie spectroscopie, waarbij de spectra op een niet-invasieve (passieve) manier worden gedetecteerd uit de heliumontladingen. Het tweede schema maakt gebruik van de lokale zeer kleine gasinjectie en een spectroscopie met verschillende kanalen om de gegevens over het elektrisch veld over de breedte van de *sheath* naast de ICRF-antennebox ruimtelijk op te meten. Deze installatie maakt het mogelijk om de geldigheid te onderzoeken van de aannames die gemaakt zijn bij het afleiden van de randvoorwaarden voor de toepassing van de RF-*sheath* in de theoretische modelleringscodes.

Om de golflengteverschuivingen van de geselecteerde lijn voor velden die zwakker zijn dan $15\,\mathrm{kV\,cm^{-1}}$ te kunnen detecteren, wordt een *Andor Shamrock 750* spectrometer in een Czerny-Turner opstelling gebruikt, die is uitgerust met een holografisch rooster van 3600 lijnen/mm en een *Andor's iStar 334* iCCD-detector. De instrumentfunctie van de optische opstelling is 0.01 nm, wat overeenkomt met ongeveer 6 pixels.

Het elektrisch veld gemeten in deze configuraties toont een goede overeenkomst met de waarden die voorspeld worden door een eenvoudig DC- en RF-gemoduleerd *sheath*-model, ontwikkeld op basis van dynamische *sheath*- theorieën voor de typische parameters in IShTAR's plasma.

Deutsche Zusammenfassung –Summary in German–

Effiziente Fusionsreaktorkonzepte müssen zunächst den Grundkriterien der Kernfusionsprozesse entsprechen. Nach diesen Kriterien reicht in einem Tokamak-Reaktor die ohmsche Heizung nicht aus, um die Zündbedingungen zu erzielen. Dem Plasma muss zusätzliche Heizleistung zugeführt werden. Eine der Heizmethoden mit dem größten experimentellen Erfolg beruht auf der resonanten Absorption von Wellen im Ionenzyklotron-Frequenzbereich (engl. Ion Cyclotron Range of Frequencies - ICRF) innerhalb einer fundamentalen (oder der harmonischen) Zyklotronschicht der Ionenspezies im Kern des Plasmas. Dies ist die ICRF-Heizung.

Um die Ausbreitung der vorteilhaften Wellenmode innerhalb dieses Frequenzbereichs zu gewährleisten, muss die Schnelle Welle der ICRF-Antenne im Inneren des Vakuumgefäßes des Tokamaks, an der Wand und nahe dem Rand des eingeschlossenen Plasmas platziert werden. In diesem Kontaktbereich zwischen Antenne und Randplasma kommt es zu Antennen-Plasma-Wechselwirkungen, die zu bestimmten unerwünschten Effekten für den Antennenbetrieb führen können. Schädliche Nebenwirkungen, wie z.B. eine verstärkte Erzeugung von Verunreinigungen aus der Wand (Antennen-Limiter), eine hohe Verlustleistung und Hot-Spots auf den Materialoberflächen der Antenne wurden experimentell in verschiedenen Tokamaks untersucht. Um diese zu vermindern, wurden Heizszenarien und Antennendesigns verbessert. Für eine korrekte theoretische Behandlung, zuverlässige autarke Simulationen und damit ein sichereres Design der ICRF- Entladung und des ICRF-Systems für lange brennende Plasmaexperimente ist jedoch ein grundlegendes Verständnis der Prozesse, die in diesem Wechselwirkungsbereich ablaufen, notwendig.

Diese Nebenwirkungen werden auf die Hochfrequenz (HF)-induzierte Modifikation der Plasmarandschicht nahe der plasmazugewandten Oberflächen der ICRF-Antenne zurückgeführt. Sobald das Plasma auf eine feste Oberfläche (eine Kachel, eine Gefäßwand oder einen Limiter) trifft, bildet sich zwischen diesen eine dünne Region von nur wenigen Elektronen-Debyelängen Breite. Dies ist die so genannte Debyeschicht, die dazu dient, gleiche Teilchenflüsse aus dem Plasma zu gewährleisten und die Ladungsambipolarität durch Beschleunigung der Ionen aus dem Plasma und Abbremsung der Elektronen zu erhalten. Im Rahmen der ICRF-Forschung und der genannten Nebenwirkungen des ICRF-Betriebes wird davon ausgegangen, dass die Effekte in der Debyeschicht,

insbesondere der Gleichstrom-Potentialabfall über der Schicht, durch die HF-Modulation verstärkt werden. Aufgrund der sehr unterschiedlichen räumlichen Skalen, die erforderlich sind, um sowohl die Dynamik der Schicht als auch die Wellenausbreitung und ihre Kopplung an das Randplasma zu erfassen, verzichten theoretische HF-Modellierungscodes auf Ersteres und ersetzen die HF-Schicht typischerweise durch die Randbedingungen, die einer dünnen Vakuumschicht mit einer bestimmten Kapazität entsprechen (anstatt sofort die Randbedingungen einzuführen, die nur der leitenden Wand entsprechen). Die Auswirkungen der RF modulierten Schicht werden indirekt berücksichtigt.Das Potential wird von der Plasmaseite der Debyeschichtgenommen. In diesem Verfahren fehlt der Schritt, die Ergebnisse eines solchen theoretischen Ansatzes mit dem tatsächlichen Antennenbetrieb zu vergleichen und die Gültigkeit der bei der Ableitung der Randbedingungen getroffenen Annahmen zu prüfen. Zur experimentellen Überprüfung dieser Annahmen wird eine dedizierte Diagnostik benötigt.

Das Ziel dieser Doktorarbeit ist die Entwicklung einer Diagnostik, die sich der Messung elektrischer Felder widmet, die sich innerhalb der HF-modulierten Randschichten der Plasma-zugewandten Strukturen der ICRF-Antenne aufbauen. Besondere Herausforderungen bestehen darin, dass eine solche Diagnostik nicht invasiv sein darf, sondern auch berücksichtigt werden muss, dass die durchschnittliche Schichtdicke zwischen einigen mm und einigen cm liegt und dass elektrische Felder im Bereich von $0-10\,\mathrm{kV\,cm^{-1}}$ bei niedrigem Druck (unter 5 Pa) und niedriger Dichte (unter $10^{18}\,\mathrm{m^{-3}}$) unter Entladungsbedingungen erfasst werden sollen, die in unmittelbarer Nähe einer ICRF-Antenne an der Peripherie des Tokamak-Plasmas auftreten.

Diese Forschung wurde an IShTAR durchgeführt, einem Prüfstand, der experimentellen Studien von Antennen-Plasma-Wechselwirkungen gewidmet ist. Dieses Gerät bietet die Möglichkeit, die von der ICRF-Antenne ausgestrahlten Wellen mit einem Plasma zu koppeln, das repräsentativ für diejenigen Plasmen ist, die in Tokamaks in der Nähe der ICRF-Antennen gefunden werden, wenn auch in einer einfacheren Konfiguration aber mit verbessertem diagnostischem Zugang.

Gemessen an den Anforderungen, die an die Diagnostik gestellt werden, wird die optische Emissionsspektroskopie als nicht-invasives Diagnoseverfahren gewählt. Der Vektor des elektrischen Feldes wird aus den gemessenen Spektren extrahiert, indem die experimentell aufgezeichnete Verschiebung der Spektrallinie mit den theoretischen Modellen, die auf der Atom- und Quantentheorie des Stark-Effekts basieren, verglichen wird. Die theoretische Berechnung der atomaren Struktur und die daraus resultierende Form und Wellenlänge der Spektrallinie aufgrund des externen elektrischen Feldes wurden unter Verwendung des EZSSS-Codes (Explicit Zeeman Stark Spectral Simulator) durchgeführt, der auch die durch ein statisches, unidirektionales Magnetfeld (dem Zeeman-Effekt) verursachten Effekte berücksichtigen kann. Die Wellenlängenverschiebung der Heliumlinie mit einer Wellenlänge von 447 nm, die dem 4^3D - 2^3P Strahlungsübergang des neutralen Heliumatoms entspricht, ist der wichtigste diagnosti-

sche Parameter.

Dieser spezielle Parameter und die Spektrallinie wurden auf der Grundlage der durch das Messgerät gesetzten Grenzen und der Einschränkungen gewählt, die von der Plasmaumgebung herrühren, welche für die experimentelle Untersuchung der ICRF-Antennen-Plasmarand-Wechselwirkungen günstig ist. Die berücksichtigten Einschränkungen sind die folgenden. IShTAR kann mit Helium und Argon betrieben werden. Der Stark-Effekt, d.h. die Korrektur auf die feldfreien ungestörten Atomenergieniveaus, ist für Helium quantenmechanisch leichter zu behandeln. In den Spektren von Helium gelten die Übergänge von den oberen Zuständen mit der "Hauptquantenzahl gleich oder kleiner 3 als unempfindlich gegenüber dem elektrischen Feld, während bei den oberen Zuständen mit $n \geq 4$ nur die hohen Drehimpulszustände erhalten bleiben sollten (P, D, F)" (W. Hicks). Schließlich wurde festgestellt, dass die Helium Spektrallinie mit einer Wellenlänge von 447 nm das optimale Gleichgewicht zwischen den genannten Einschränkungen, der Signalstärke, die von IShTARs Plasma in der Nähe der Antenne aufgezeichnet wird, und den Eigenschaften des für die Diagnostik verwendeten Spektrometers darstellt. Der diagnostische Parameter der Wahl ist die Spektrallinienverschiebung aus ihrer ungestörten Position, da die anderen potentiellen diagnostischen Parameter, die häufig in der Stark-Spektroskopie von Heliumatomen verwendet werden, unter Entladungsbedingungen in unmittelbarer Nähe einer ICRF-Antenne unzugänglich sind. Außerdem hängt dieser Parameter nicht vom Messinstrument ab, so dass er zum Vergleich der Ergebnisse aus verschiedenen Experimenten verwendet werden kann.

In IShTAR wurden zwei Diagnoseschemata entwickelt. Ein Schema erlaubt die Messung des volumenintegrierten elektrischen Feldes im Schichtbereich der gleichstrombetriebenen Elektrode (was in dieser Arbeit als Proof-of-Concept diente) und im Schichtbereich der ICRF-Antennenbox (da solche Daten für den experimentellen Benchmark der theoretischen Behandlung der Antennen-Plasma-Wechselwirkung von Nutzen sind). Dies geschieht mit der passiven optischen Emissionsspektroskopie, bei der die Spektren passiv von den Heliumentladungen aufgenommen werden. Das zweite Schema nutzt die lokale Injektion eines Diagnostikgases (Helium) und eine Mehrkanalspektroskopie, um räumlich aufgelöste Daten des elektrischen Feldes über die Breite der Schicht neben der ICRF-Antennenbox zu ermöglichen. Dieser Teil ermöglicht die Untersuchung der Gültigkeit der Annahmen, die bei der Ableitung der Randbedingungen für die Implementierung der HF-Randschicht in den theoretischen Modellierungscodes getroffen wurden.

Um die Wellenlängenverschiebungen der ausgewählten Linie für Felder unter $15\,\mathrm{kV\,cm^{-1}}$ aufzulösen, wird das Czerny-Turner-Spektrometer *Andor Shamrock 750* verwendet, das mit einem holographischen Gitter von 3600 $^{\text{Linien}}/_{\text{mm}}$ und einem iCCD-Detektor *Andor's iStar 334* ausgestattet ist. Die Instrumentenfunktion der optischen Anordnung beträgt 0.01 nm, was in etwa 6 Pixeln entspricht.

Das in diesen Anordnungen gemessene elektrische Feld zeigt eine gute Übereinstimmung mit den Werten, die von einem einfachen DC- und HF-modu-

lierten Plasmarandschichtmodell, das auf der Grundlage der Theorien zur Plasmarandschichtdynamik entwickelt wurde, für den Parameterraum im IShTAR-Plasma vorhergesagt werden.

English summary

Efficient fusion reactor concepts must first be in line with the basic criteria imposed by nuclear fusion processes. Those criteria imply that, in order to achieve ignition conditions in a tokamak-type reactor, Ohmic heating is not sufficient and additional heating power must be supplied to the plasma. One of the methods with the most experimental success in heating tokamak plasmas is based on the resonant absorption of waves in Ion Cyclotron Range of Frequencies within a fundamental (or the harmonic) cyclotron layer of the ion species in the core of the plasma. This is the ICRF heating.

To ensure the propagation of the favourable wave mode within this frequency range - the Fast Wave, the wave launcher (i.e. an ICRF antenna) must be placed inside the vacuum vessel of the tokamak, at the wall and close to the edge of the confined plasma. This introduces the contact region between the antenna and the edge plasma, which leads to antenna - plasma interactions that result in certain unwanted effects to the antenna operation. The harmful side effects, such as the enhanced generation of the impurities from the wall (antenna limiters), power dissipation and hot-spots formation on the material surfaces of the antenna, were observed experimentally in various tokamaks. To mitigate these, the heating scenarios and the antenna designs were improved. However, a fundamental understanding of the processes taking place within this interaction region is necessary for proper theoretical treatment, reliable self-sufficient simulations and, with that, a more confident designing of the ICRF discharge and the ICRF system for the long-pulse burning plasma experiments.

These side effects are attributed to the RF-induced modification of the sheath layer adjacent to the plasma-facing surfaces of the ICRF antenna. Once plasma encounters a solid surface (a tile, a vessel wall, or a limiter) a thin, few electron-Debye-lengths wide, region forms sandwiched between them. This is the so-called sheath layer, which serves to ensure equal particle fluxes from the plasma, and to preserve the charge ambipolarity by accelerating ions from the plasma and decelerating the electrons. Within the framework of the ICRF research and said side effects to the ICRF operation, the effects of the plasma sheaths, particularly the DC potential drop across the sheath, are believed to be enhanced by the RF modulation. Owing to the vastly different spatial scales needed to capture both the dynamics of the sheath layer and the wave propagation and its coupling to the edge plasma, theoretical RF modelling codes omit the former and typically substitute the RF sheath with the boundary conditions equivalent to a thin vacuum layer of a certain capacitance (instead of immediately intro-

ducing the boundary conditions corresponding solely to the conducting wall). The effects of the RF modulated sheath are accounted for indirectly. The sheath potential is taken from the plasma side of the plasma-sheath boundary. The missing step in this procedure is to benchmark the results of such theoretical approach with the actual antenna operation and test the validity of the assumptions made in the derivation of the boundary conditions. For this purpose, a dedicated diagnostic equipment is required.

The goal of this doctoral thesis is to develop a diagnostic dedicated to the measurement of electric fields established within the RF modulated sheaths of the plasma-facing structures of the ICRF antenna. The particular difficulties attributed to this task are that such diagnostic must not be invasive, while also taking into consideration that the average sheath thickness is between a few mm to a few cm, it should detect electric fields within the $0-10\,\mathrm{kV\,cm^{-1}}$ range, in low pressure (below 5 Pa) and low density (below $10^{18}\,\mathrm{m^{-3}}$) discharge conditions encountered in the immediate vicinity of an ICRF antenna at the periphery of the tokamak plasma.

The research was carried out on IShTAR, a test stand dedicated to experimental studies of antenna-plasma interactions. This device offers the possibility of coupling the waves launched from the ICRF antenna to a plasma representative of those found in the vicinity of the ICRF antennas in tokamaks, albeit in a simpler configuration and with improved diagnostics access.

Gauged against the requirements imposed on the diagnostic, optical emission spectroscopy is chosen as a diagnostic technique for being non-invasive. The electric field vector is extracted from the measured spectra by comparing the experimentally recorded shift of the spectral line with the theoretical models based on the atomic and quantum theory of the Stark effect. The theoretical calculation of the atomic structure, and the resulting spectral line shape and wavelength, due to the external electric field were carried out using the EZSSS (Explicit Zeeman Stark Spectral Simulator) code, which can also account for the effects caused by static, unidirectional magnetic field (the Zeeman effect). The wavelength shift of helium line with 447 nm wavelength, corresponding to 4^3D - 2^3P transition of neutral helium atom, is the main diagnostic parameter.

This particular parameter and the spectral line were chosen on the basis of the limitations placed by the device and the constrains stemming form the plasma environment that is favourable for experimental investigation of the interactions between an ICRF antenna and the plasma edge. The limitations taken into account are the following. IShTAR can operate with helium and argon. The Stark effect, i.e. the correction to the field-free unperturbed atomic energy levels, is easier to treat quantum-mechanically for helium. In the spectra of helium, the transitions from the upper states with the "principle quantum number, n, equal or lower than 3 are considered insensitive to the electric field, while for those with the upper states having $n \geq 4$, only the high angular momentum states should be retained (P, D, F)" (W. Hicks). Finally, the helium line with 447 nm wavelength was found to be the optimal balance between these concerns, the signal strength recorded from IShTAR's plasma in the vicinity of

the antenna, and the detection capabilities of the spectrometer used for the diagnostic purposes. The spectral line shift from its unperturbed position is the diagnostic parameter of choice given that the other potential diagnostic parameters which are often used in Stark spectroscopy of helium atoms are inaccessible under the discharge conditions encountered in the immediate vicinity of an ICRF antenna. Furthermore, this parameter does not depend on the instrument, so it can be used to compare the results obtained from different experiments.

In IShTAR, two diagnostic schemes were developed. One scheme allows for measuring the volume-integrated electric field in the sheath region of the DC powered electrode (which served as a proof of concept in this work), and in the sheath region of the ICRF antenna box (as such data is of use for the experimental benchmark of the theoretical treatment of the antenna-plasma interaction). This is done with the passive optical emission spectroscopy, where the spectra are recorded passively from the helium discharges. The second scheme makes use of the local trace-gas injection and a multi-channel spectroscopy to allow for the spatially resolved data on electric field across the width of the sheath adjacent to the ICRF antenna box. This instalment allows for investigation of the validity of the assumptions made when deriving the boundary conditions for the RF sheath implementation in the theoretical modelling codes.

To resolve the wavelength shifts of the selected line for fields that are below $15\,\mathrm{kV\,cm^{-1}}$, the *Andor Shamrock 750* spectrometer in the Czerny-Turner mount is used, which is equipped with a holographic grating of 3600 lines/mm and an *Andor's iStar 334* iCCD detector. The instrumental function of the optical arrangement is 0.01 nm, or about 6 pixels.

The electric field measured in these configurations shows good agreement with the values predicted by a simple DC and RF-modulated sheath model, developed based on the sheath dynamics theories, for the parameter space in IShTAR's plasma.

1 Introduction

The past century has witnessed a persistent scientific and technological endeavour to develop the conditions for controlled terrestrial nuclear fusion. The sole aim is to provide a peaceful and safe use of nuclear energy for our rapidly developing and growing civilisation.

The mounting evidence suggests that our habits of the energy production and the energy use are the leading cause of the altering environmental conditions to which the Earth's biosphere, thus our very existence, is fine-tuned[1]. To satisfy the ever-increasing energy consumption *and* stimulate sustainable development of the entire world while, at the same time, completely abandoning polluting energy sources, nuclear energy, both fission and fusion, emerge as the *sui generis* solution[2].

Nuclear fission power has been commercialised since 1956[3]. It is the source with the highest production of energy per unit mass of fuel and relatively small environmental impact. Nevertheless, it contributes with a mere 11% to the global electricity production [1.4]. Due to numerous factors that govern the use of nuclear fission power plants, it is unlikely that this percentage will increase. The main elements driving the public and investor attitudes away from

[1] "For their efforts to build up and disseminate greater knowledge about man-made climate change, and to lay the foundations for the measures that are needed to counteract such change" Intergovernmental Panel on Climate Change (IPCC) and Albert Arnold (Al) Gore Jr. were awarded The Nobel Peace Prize in 2007 [1.1].

[2] An extensive analysis of this complex issue may be found in [1.2].

[3] World's first full scale nuclear power station, Calder Hall, was connected to the grid in August 1956 [1.3].

nuclear fission are the perceived negative record of operational safety, nuclear proliferation and waste disposal, along with rising costs of nuclear power plants compared to renewable energy sources.

Nuclear fusion, on the other hand, shares the same benefits of the energy production introduced by nuclear fission, while avoiding (or at least minimising) the negative concerns that follow it [1.5].

Fusing lighter atomic nuclei produces energy due to the difference in mass of the fusion reaction product compared to the combined mass of the reactant nuclei[4]. This continues to be the case until the combined mass reaches the mass of iron. Therefore, nuclear fusion reactions cover a whole range of combinations. Only a few among these are considered for exploiting nuclear fusion for power production on Earth. The most accessible fusion reaction, in terms of required input energy, is the one occurring between the two isotopes of hydrogen - deuterium (D) and tritium (T):

$$\mathrm{D} + \mathrm{T} \rightarrow \mathrm{He}^4 + \mathrm{n} + 17.6\,\mathrm{MeV}.$$

This reaction yields 17.6 MeV[5] of energy which is carried by the reaction products - a helium nucleus (He^4) and a neutron (n).

As the half-life of tritium is 12.32 ± 0.02 years, it has to be produced, which can be achieved with a neutron activation of lithium-6 and -7, in a process called tritium breeding. The "raw" fuel (deuterium and lithium) is one of the advantages of nuclear fusion as a power source: it is worldwide abundant, inexhaustible, does not require large-scale extraction procedures, and it yields high energy density per fuel mass. The next advantage is that the problem of radioactive waste is reduced to short- to medium-term waste management when compared with fission processes (albeit with a comparable volume), since the fusion reactors' structural components are activated by bombardment with high-energy neutrons. Another motivating advantage of using fusion processes for the energy production is that the D-T fusion reaction, including tritium breeding, does not produce greenhouse gases, nitrogen- and sulphate-oxides nor particulate emission.

All these points together are the main motivation behind the unprecedented international efforts in research, development, demonstration and deployment of nuclear fusion power production.

[4] This mass-to-energy conversion is captured within the well-known $E = mc^2$, or to be precise the $\Delta E = \Delta mc^2$ where Δ symbol is referring to the surplus of the given quantity.

[5] Through this manuscript, electronvolt (eV) is used as a unit of energy ($1\,\mathrm{eV} = 1.6 \times 10^{-19}\,\mathrm{J}$) and also as a unit of temperature ($1\,\mathrm{eV} = 1.16 \times 10^4\,\mathrm{K}$).

1.1 Basic requirements for controlled fusion power production

The difficulties of any strategy to fusion power production originate from the elemental conditions coupled in the process's power balance. Numerous textbooks [1.6–1.10] and studies [1.11, 1.12] discuss this matter in elaborate detail. This section is their short summary.

The natural starting point are the parameters defining the nuclear reaction - the reaction energy and the reaction probability. The first consists of an input energy that the reactant nuclei need to overcome the Coulomb barrier (because they are the particles of the same charge), and the output energy from a fusion reaction that not only has to balance the input one, but is sufficiently much larger.

Even if the circumstances ensure that the nuclei can overcome the Coulomb barrier, they are much more likely to scatter off each other. The Coulomb-scattering issue requires that the fusion fuel is kept in a volume for a sufficiently long time to allow for enough attempts to be made, which is known as *the confinement*. Confining particles at the energies required for the largest reaction probability, or the cross-section, sets the conditions for a thermonuclear plasma. In the plasma domain, the system's energy is described by its temperature, which introduces the dependence on this quantity into a fusion reaction cross section.

In the situation where a number of fusion nuclei are confined within a volume, the reaction cross section is averaged taking into account the Maxwellian distribution of relative particle velocity, defined as the averaged reactivity $\langle \sigma v \rangle$. The peak averaged reactivity of a D-T fusion reaction is reached at about 60 keV[6]. The averaged reactivity of the "top three" fusion reactions, D-T, D-D and D-He^3 at the temperature of the system of 60 keV are compared in the Table 1.1, together with the fusion energy gain from each.

Even at the temperatures much lower than 60 keV, the average reactivity of a D-T reaction is orders of magnitude larger than that of the other two. With these reasons the fusion fuel choice is set to deuterium and tritium.

Maintaining the pressure placed on the "walls" of a "container" by plasma particles within reasonable limits for such high plasma temperatures means that the particle density must be rather low[7]. To ensure optimum power generation from fusion reactions, on the other end, the plasma density should not be too low. The particle density in a practical reactor should be around $n_e \approx 10^{20}$ particles/m^3.

[6] The temperature dependency of averaged reactivity for several fusion reactions is given in the A.1.

[7] The other possibility is compressing the fuel mixture with laser or particle beams to allow for very high density for a very short time pulses, an approach known as the inertial confinement which will not be discussed here.

	Fuel	Output	Energy gain MeV	Averaged reactivity cm^3s^{-1}
1	D+T	He^4 + n	17.6	8.7×10^{-16}
2	D+D	T + p; He^3 + n	3.7	1.6×10^{-17}
3	D+He^3	He^4 + p	18.3	7×10^{-17}

Table 1.1: Practical fusion fuels for energy production, ordered according to their feasibility rank.

Power balance

Finally, in order for any fusion device to be useful for practical applications (which would distinguish between a physics experiment and a reactor concept), the reaction processes must be able to achieve a positive power balance ($P_{out} \gg P_{in}$). Once the plasma temperature is sufficiently high for fusion reactions to occur at a reasonable rate, the energy remaining in the plasma must be high enough to at least maintain this temperature. Comparing the fusion power generated with the additional heating required to contrast the losses is an important analysis for assessing the efficiency of the fusion power production or for measuring the progress of current experimental devices.

To facilitate this analysis, a number of simplifying assumptions are made. First, the plasma is hydrogenic with high level of purity - the fuel is fully ionized 50%/50% D-T mixture, with a small contribution of fusion-born helium nuclei (the α-particles) and negligible concentration of impurities. This implies the following: $n_D + n_T = n_i = n_e$, $n_\alpha \ll n_e$, $Z_{eff} \approx 1$, where n_x is denoting the density of the plasma particle species (deuterium and tritium nuclei, ions as a collective, electrons and the α-particles, in the order of appearance) and Z_{eff} is the effective atomic number of the plasma[8]. Second, the fusion plasma is assumed thermalized: $T_D = T_T = T_e = T$, where T_x referrers to the temperature of deuterium and tritium ions and the plasma electrons, respectively. For the fully ionized fuel that is in thermal equilibrium, the energy stored in plasma is then simply $W = 3n_eT$.

The power balance under such assumptions is:

$$\frac{d}{dt}W = P_{aux}V + P_\alpha V - P_L V - P_B V.$$

The rate of change of the stored energy in a plasma, W, is influenced by several

[8]This quantity is defined as $Z_{eff} = \sum_{\text{ions }(i)} (n_i \overline{Z_i}^2)/n_e$, where $\overline{Z_i}$ is the average charge state of the ion species and the summation is over every ion species in the plasma.

sources and sinks of power within its volume, V. The first term on the right-hand side of the above equation is the external power density, $\mathrm{P}_{\mathrm{aux}}$, invested in heating the plasma volume. The second term, P_α, is a fraction of power density produced by nuclear fusion reactions that is carried by the fusion-born helium nuclei which stays confined within plasma. The power sinks are the losses through heat conduction and particle transport, P_L, and the radiation losses through Bremsstrahlung, P_B.

Assuming stationary state, $\mathrm{d}W/\mathrm{d}t = 0$, the above equation reads:

$$\mathrm{P}_{\mathrm{aux}} + \mathrm{P}_\alpha = \mathrm{P}_L + \mathrm{P}_B. \tag{1.1}$$

The total power generated from fusion reactions per unit time in unit volume of plasma as assumed above, each releasing E_f amount of energy is given by:

$$\mathrm{P}_f = n_{\mathrm{D}} n_{\mathrm{T}} \langle \sigma v \rangle_{DT} E_f = \frac{1}{4} n_e^2 \langle \sigma v \rangle_{DT} E_f,$$

where $\langle \sigma v \rangle_{DT}$ is the average reactivity. Each fusion event releases E_f amount of energy. One fifth of this energy remains confined in the plasma, carried by the fusion-generated α-particle, E_α. The α-power, P_α, in Eq. 1.1 is evaluated as:

$$\mathrm{P}_\alpha = n_{\mathrm{D}} n_{\mathrm{T}} \langle \sigma v \rangle_{DT} E_\alpha = \frac{1}{4} n_e^2 \langle \sigma v \rangle_{DT} E_\alpha.$$

P_L is a macroscopic quantity that encapsulates the power losses through heat conduction and particle transport. It is defined in terms of the energy stored in the plasma and the overall energy confinement time, τ_E, which can be understood as quantifying the thermal insulation of plasma:

$$\mathrm{P}_L = \frac{W}{\tau_E} = \frac{3 n_e T}{\tau_E}.$$

In addition to the power "leakage" through heat conduction and particle transport, an important power loss mechanism is the Bremsstrahlung radiation emission:

$$\mathrm{P}_B = c_B n_e^2 T^{1/2} Z_{\mathrm{eff}},$$

with c_B denoting the Bremsstrahlung constant.

With the constituents of the fusion plasma power balance established, it is possible to take a closer look at the requirements for certain plasma parameters to achieve a regime when the plasma power is self-sufficient. The power losses are offset by the α-power in this case, called *ignition*, and no external heating is required any longer ($\mathrm{P}_{\mathrm{aux}} = 0$):

$$\mathrm{P}_\alpha = \mathrm{P}_L + \mathrm{P}_B.$$

Upon replacing the appropriate expressions for the power sources and losses, the above equation provides the following criterion for ignition of pure deuterium-tritium plasma specified by the premises stated at the beginning of this analysis:

$$(n_e\tau_E)_{\text{ign}} = \frac{12T}{\langle\sigma v\rangle_{DT}E_\alpha - 4c_B T^{1/2}}. \tag{1.2}$$

There are other power-related thresholds before ignition is achieved that are critical in the fusion community. Such milestones are expressed in terms of the fusion energy gain[9] $Q \equiv {}^{P_f}/_{\text{P}_{\text{aux}}}$:

$$n_e\tau_E = \frac{12T}{\langle\sigma v\rangle_{DT}E_\alpha\,({}^5/_Q + 1) - 4c_B T^{1/2}} = \mathscr{F}(T). \tag{1.3}$$

One of these milestones is the *break-even*, when the reactor achieves as much fusion power release as auxiliary heating power is invested into the plasma: $P_f = \text{P}_{\text{aux}}$ and $Q = 1$.

All operational variables of the Eq. 1.3, i.e. the density and confinement time as a measure of the confinement quality, and the temperature need to be large for the ignition to occur. The temperature at which the function $\mathscr{F}(T)$ reaches its minimum is in the interval between $10-20\,\text{keV}$.

1.2 Magnetic confinement fusion devices - Tokamaks

Everything outlined in the previous section were the known facts prior to the 1960s. Over the following decades a number of approaches to fusion power production have been disclosed, attempted or proposed. The most effective method with respect to the discussion of the previous section was, and still is, a magnetically confined plasma in a tokamak [1.8]. So far, tokamaks have been the only devices capable of attaining values of fusion energy gain factor greater than $Q = 0.1$, with the highest[10] $Q \approx 0.67$ achieved by the JET (Joint European Torus) tokamak. The first fusion experiment that is designed to demonstrate the engineering feasibility of fusion power production and achieve $Q = 10$ milestone, ITER, is also a tokamak.

The idea behind the magnetic confinement fusion (MCF) devices is that the charged plasma particles are bound to the magnetic field lines by the Lorentz force, following a spiral trajectory. The magnetic field, therefore, ensures that the charged particles are confined, but only in a plane perpendicular to it.

One way to avoid losses of particles parallel to the magnetic field is to attempt to close the field lines back on themselves, in a toroidal loop. This is

[9] For the case of ignition, $Q \to \infty$.
[10] As of the date of this manuscript.

achieved with a system of magnetic field coils wrapped around a toroidal vessel to introduce the magnetic field throughout the device, which is the foundation of a tokamak and stellarator design. Since the magnetic field created in this manner will no longer be homogeneous, but curved, it will cause drifts of the charged particles, namely the curvature and the *grad*-B drift. These lead to the separation and accumulation of charges at the vertical edges of a vessel, thereby causing vertical electric field that introduces another - $E \times B$ particle drift. The final effect is the loss of particle confinement in the radial direction of the plasma cross-section and towards the horizontal edges of the vessel.

In order to save the confinement in the closed-field-line configuration, an additional magnetic field must be created in a poloidal plane - perpendicular to the toroidal field, which will short-circuit the charge accumulation on the vertical edges of a vessel. The poloidal field can be generated in two ways - by driving a current through the (toroidally confined) plasma, which is the operating principle of a tokamak, and by breaking the axial symmetry, as in stellarator-type devices.

Tokamaks have been thoroughly studied over the previous decades, leading to further optimizations and improvements, but also well-defined issues that are an immediate focus of the contemporary fusion community [1.13]. By contrast, the stellarator concept is still at its infancy. In this perspective, although the content of this thesis can possibly be applied to stellarators, the further discussion will be limited to tokamaks. This is additionally motivated by the overall consensus in the community that tokamaks can effectively generate net energy.

Figure 1.1 displays a schematic illustration of a typical tokamak. The toroidal field coils, that create the toroidal magnetic field B_ϕ, are indicated, together with the vacuum vessel around which they are looped. The current flowing through the plasma, I_p, is generated by the transformer action. The main elements for this are the primary of a transformer circuit - the central solenoid located in the hole of a toroid, and the plasma itself, as a closed loop of charged particles, being the secondary of a transformer circuit. The flux swing in the primary induces a magnetic flux which produces a current in the secondary, i.e. the plasma. In turn, this current creates the poloidal B_θ magnetic field. The resulting magnetic field lines are helical. Tokamaks have an additional set of coils following the vessel's toroidal curvature. These are the outer poloidal field coils that are used to control the plasma's position and shape.

The inherent property of tokamaks is that, due to the resistivity of the plasma medium, the current flowing through it to establish confinement is also heating the plasma inductively. Since plasma resistivity is a temperature-dependent quantity, $\eta \propto T^{-3/2}$, and will thus decrease with temperature, this, also called "Ohmic" heating, method is effective in reaching only a few keV. In addition, the current pulses in the central solenoid are a technological limitation on the

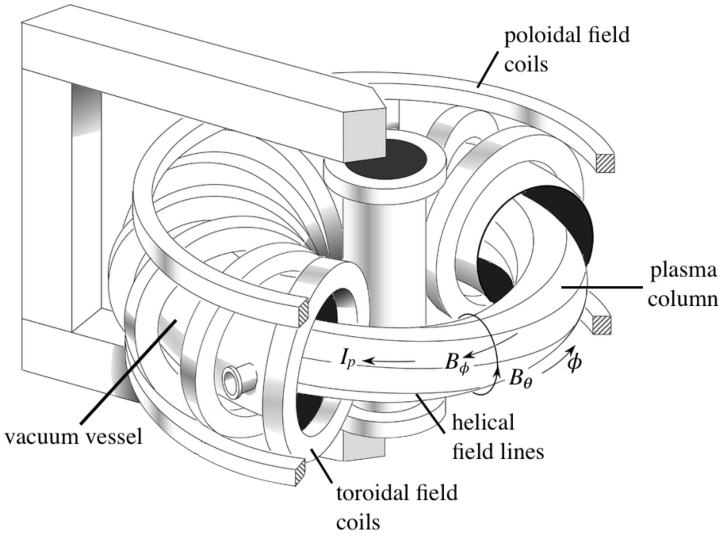

Figure 1.1: Schematic illustration of a tokamak. Adapted from [1.14].

discharge duration - a feature which makes tokamaks operating only in pulses.

1.3 Heating tokamak plasma with waves in the ion cyclotron range of frequencies

It has been shown in Section 1.1 that, because the rate of fusion reactions depends on the temperature, this quantity must be sufficiently high prior to achieving the power balance. Heating methods additional to the Ohmic one are therefore necessary.

Throughout the decades of tokamak development, various additional heating systems have been proposed and several have proved to be reliable and effective in increasing the plasma temperature[11]. Beside injection of a neutral beam of particles (NBI, Neutral Beam Injection, heating) and launching microwaves (ERCH, Electron Cyclotron Resonance Heating), using electromagnetic waves in the Ion Cyclotron Range of Frequencies, ICRF, is one of the methods that has been used in major experiments over the years and is foreseen for ITER [1.15]. This is expected to be one of the heating and current-drive systems in the next step fusion devices as well.

ICRF systems in MCF devices consist of a transmission line (a coaxial line for

[11]The heating methods named in the paragraph are also applied in various different ways - they are used to give rise to additional plasma current, which is useful to prolong tokamak pulses, they can be used as a part of a diagnostic scheme, or to target and control localised instabilities [1.15].

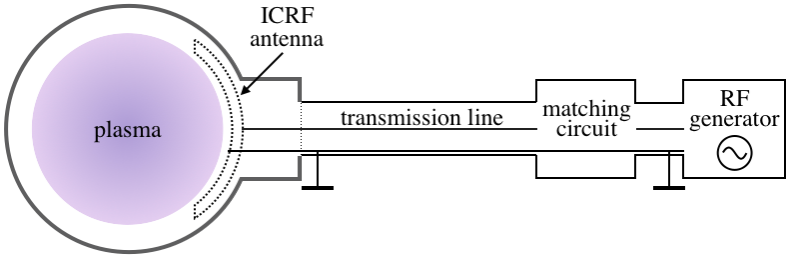

Figure 1.2: Schematic representation of an ICRF system of a tokamak.

this particular range of frequencies) which guides the electromagnetic waves from an external generator to the wave launcher placed inside of the vacuum vessel. At the interface of the launcher, i.e the current strap of the ICRF antenna, the electromagnetic wave is converted to a particular mode able to propagate in the plasma. It deposits its energy in a specific location through resonant absorption. The wave's energy is further distributed in the plasma volume through collisions. A simplified scheme of a typical ICRF system is illustrated in Fig. 1.2.

For a wave to be able to travel through a plasma, and for it to deposit its energy into a specific layer, its frequency and wavelength must satisfy the plasma dispersion relation, while the wave absorption layer must match the plasma resonance. Magnetized plasmas host a large number of wave modes that can be used to transfer the energy. Because choosing the correct mode and the frequency range of the electromagnetic wave requires a complex strategy, it helps to simplify it if it is analysed by going from the absorption mechanism back to the launcher.

The mechanism of wave absorption, i.e. the energy transfer, through resonance corresponds to a situation where the electric field of the wave has the right frequency and the right polarisation to provide a constant force felt by a specific charged particle species in a plasma. In this kinetic picture of wave-particle interaction the wave frequency from the reference frame of a particle is Doppler-shifted. A particle is accelerated once the wave frequency it "feels" becomes either zero or a multiple of a cyclotron frequency, which is a gyration frequency of a magnetically confined charged particle while it follows the helical path along the magnetic field line ($\Omega_{c,s} = {}^{q_s B}/_{m_s}$, with q_s being the charge of the particle of mass m_s, in a magnetic field B). This is defined as a resonance condition:

$$\omega - \vec{k} \cdot \vec{v} = \mathrm{H}\Omega_{c,s} = \mathrm{H}\frac{q_s B}{m_s},$$

where ω is the frequency of the wave, $\vec{k}$ is the wavevector, $\vec{v}$ is the particle velocity, and $\mathrm{H} = 0, 1, 2, ...$ is the harmonic. The velocity dependence makes the

resonance a layer of a certain width, situated in a specific region of the plasma volume. This region is accessed through the dependency of the cyclotron frequency on the magnetic field strength as it is a function of the radial coordinate. The half-width of the resonance absorption layer is proportional to $\propto {}^{Tm_s^{-1}}/_{\omega k_\parallel^{-1}}$ [1.16].

ICRF heating relies on resonances with ion species, which occur at the Ion Cyclotron Resonance frequency. The frequency range of the chosen wave is then:

$$f_{c,i} = \frac{\Omega_{c,i}}{2\pi} \approx 15.25 \times B \,[\text{MHz per T}]$$

for hydrogen ions [1.17].

To select a wave that propagates in a specific geometry in the plasma in the presence of a magnetic field, the fluid model of plasma must be considered. In this framework, propagative wave modes are the ones representing the real solutions of a dispersion relation.

A cold magnetized plasma model is typically used to derive the conditions under which the waves can exist and propagate in tokamak edge plasmas. This model assumes fixed background magnetic field and fixed plasma density, and ignores the thermal motion of particles. The dispersion relation is derived in a standard manner, by transforming in Fourier analysis in space and time, linearising and than combining the Ampere's and Faraday's law into a single, "wave", equation:

$$\vec{k} \times (\vec{k} \times \vec{E}) + i\omega\mu_0 \vec{J} + \frac{\omega^2}{c^2}\vec{E} = 0. \tag{1.4}$$

Using a general form of the Ohm's law to express the current density in terms of the electric field ($\vec{J} = \overline{\overline{\sigma}} \cdot \vec{E}$, with $\overline{\overline{\sigma}}$ as a conductivity tensor), it is further convenient to introduce the dielectric tensor in the expression:

$$\overline{\overline{\epsilon}} = \overline{\overline{I}} + \frac{i\mu_0 c^2}{\omega}\overline{\overline{\sigma}}. \tag{1.5}$$

With this, the wave equation becomes:

$$\vec{k}(\vec{k} \cdot \vec{E}) - k^2\vec{E} + \frac{\omega^2}{c^2}\overline{\overline{\epsilon}}\vec{E} = 0 \tag{1.6}$$

or:

$$[A]\vec{E} = 0, \tag{1.7}$$

where $[A] = \vec{k}\vec{k} - k^2\overline{\overline{I}} + \frac{\omega^2}{c^2}\overline{\overline{\epsilon}}$.

The non-trivial solutions of the Eq. 1.7, $\vec{E} \neq 0$, are those for which the determinant of the matrix $[A]$ is zero. This condition yields a dispersion relation which defines the possible wavevectors of waves in the plasma.

It is customary to track how the wave's phase velocity in plasma compares to the speed of light in that medium, which is achieved by the refractive index $N = \frac{kc}{\omega}$. It is also useful to construct a dimensionless vector that has the magnitude of a refractive index and is aligned along the vector of wave propagation, $\vec{N} = \frac{c}{\omega}\vec{k}$. The dispersion relation can then be expressed in terms of $\vec{N}$. If the analysis is examining the propagation of waves in the xz plane, and the background magnetic field is parallel to the z axis[12], then $N_\parallel = N_z = N\cos\theta, N_\perp = N_x = N\sin\theta, N_y = 0$, where θ is denoting the angle between $\vec{N}$ and $\vec{B}$. This gives the dispersion relation in the following form:

$$\begin{aligned} N_\perp^4\left(1-\sum_s \frac{\omega_{p,s}^2}{(\omega^2-\Omega_{c,s}^2)}\right)- \\ -N_\perp^2\left(\left(\sum_s \frac{i\omega_{p,s}^2\Omega_{c,s}}{\omega(\Omega_{c,s}^2-\omega^2)}\right)^2+\left(1-\sum_s \frac{\omega_{p,s}^2}{(\omega^2-\Omega_{c,s}^2)}-N_\parallel^2\right)\left(2-\sum_s \frac{\omega_{p,s}^2\Omega_{c,s}^2}{\omega^2(\omega^2-\Omega_{c,s}^2)}\right)\right)+ \\ +\left(1-\sum_s \frac{\omega_{p,s}^2}{\omega^2}\right)\left(\left(\sum_s \frac{i\omega_{p,s}^2\Omega_{c,s}}{\omega(\Omega_{c,s}^2-\omega^2)}\right)^2+\left(1-\sum_s \frac{\omega_{p,s}^2}{(\omega^2-\Omega_{c,s}^2)}-N_\parallel^2\right)^2\right)=0. \end{aligned} \tag{1.8}$$

The cold plasma dielectric tensor is here unfolded. The dispersion relation written in this form clearly shows how the propagation of the wave in a particular direction (the square of the refractive index must be greater than 0) will depend on the plasma parameters such as the density of different charged species (s) through the plasma and gyration angular frequencies of the particles as defined by:

$$\omega_{p,s} = \sqrt{\frac{n_s q^2}{m_s \epsilon_0}}$$
$$\Omega_{c,s} = \frac{|q_s|B}{m_s}.$$

In the frequency range of several tenths of a MHz, ($\omega \approx \Omega_{c,i} \ll \omega_{p,i} \ll \omega_{p,e}$), further simplification of Eq. 1.8 leads to a dispersion relation which describes a fast wave [13] [1.19] - a preferred mode for ion cyclotron heating schemes [1.6]:

[12] z is a toroidal, and x radial direction in a tokamak geometry.
[13] The adjective refers to the phase velocity [1.18].

$$N_\perp^2 = \frac{\left(\sum_s \frac{\omega_{p,s}^2}{\Omega_{c,s}(\omega+\Omega_{c,s})} - N_\parallel^2\right)\left(\sum_s \frac{\omega_{p,s}^2}{\Omega_{c,s}(\omega-\Omega_{c,s})} + N_\parallel^2\right)}{\left(\sum_s \frac{\omega_{p,s}^2}{(\omega^2+\Omega_{c,s}^2)} + N_\parallel^2\right)}. \tag{1.9}$$

However, the fast wave can not propagate through regions where the electron plasma density is below a certain value. This is seen in the Eq. 1.9, when the requirement that $N_\perp^2 > 0$ is imposed. For typical tokamak parameters it can be shown that the fast wave has a cut-off at $n_e \approx 10^{18}\,\mathrm{m}^{-3}$. Tokamak plasmas have radial profiles of electron density with a gradient towards the edge that are fortunately steep enough for the wave to tunnel through. For this reason, the wave launcher has to be placed inside the vacuum chamber, near the confined plasma [1.8].

The launcher itself is a metal strap (the number of straps differs depending on the ICRF scenario used in different devices) through which an oscillating current will flow, short-circuited at one end to generate the fast-wave-inducing magnetic field. To minimize the strong electric fields in the proximity of an antenna, created by the antenna itself, which would accelerate the ions onto the antenna surfaces, a Faraday screen is placed in front of the strap(s). This is typically a set of horizontal bars arranged in a direction parallel to the confining magnetic field (or the dominant toroidal component). The whole arrangement is framed with the limiter tiles, with the purpose of restricting the stretch of the plasma column further radially outwards. A typical ICRF antenna box is depicted in Fig. 1.3.

Even though ICRF antennas would ideally launch a pure fast wave, with a dominating orientation of the electric field vector perpendicular to the lines of a confining magnetic field, and a negligible component parallel to it, in practice this is often not the case. During the ICRF antenna operation in tokamak plasmas, some portion of the power delivered to the launcher is coupled to the slow wave branch. This is a wave mode with a significant electric field component parallel to the confining magnetic field. It is evanescent at high electron densities but propagative at the lower ones, such as those found at the edge of the tokamak plasmas towards the vessel walls and in the near vicinity of the ICRF antenna. The slow wave is generated either by the antenna itself or from a mode conversion of the fast wave in the low-density region.

The existence of the slow wave in the vicinity of the antenna and the surrounding passive structures leads to enhanced sputtering of the material and the coating from the limiter tiles, erosion and damage of the material and the launcher, and power dissipation on the surrounding surfaces instead of it propagating to the core of the plasma. These side-effects to ICRF operation have been observed in various experiments as increased impurity concentration in

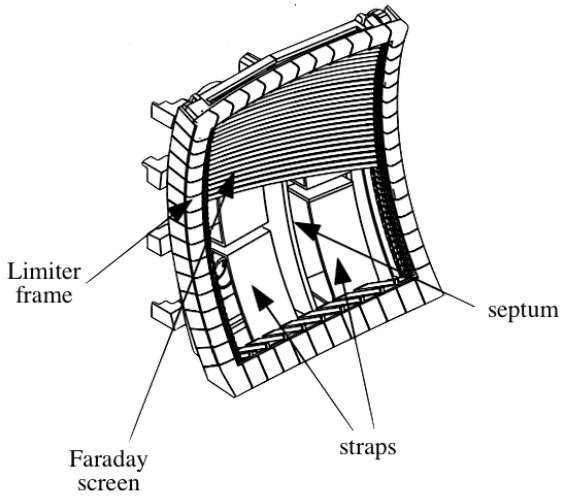

Figure 1.3: Typical two-strap ICRF antenna box and its constituents.

the plasma, rapid density rise, hot spots on the antenna box, or missing RF power [1.20, and references therein]. They all lead to the limited proper functionality and endurance of the ICRF antenna, even more so in the long-pulse burning plasma experiments [1.20].

How can only a fraction of RF power coupled to a parasitic wave mode contribute to such detrimental effects? The contemporary hypothesis is concentrated on a thin interface region between the plasma and the material surfaces, called the sheath [1.21]. The sheath that forms around the plasma-facing structures of an ICRF antenna has RF-driven properties (elaborated in the Chapter 2 of this manuscript). The parallel component of the RF electric field will introduce large RF sheath potential and, in order to conserve the charge ambipolarity, this oscillating sheath potential is rectified generating a time-independent potential in the sheath. This large potential restricts the electrons to the plasma while accelerating ions to the surfaces and may lead to increased sputtering of the surface material.

1.4 IShTAR - Ion Cyclotron Sheath Test Arrangement

Testing the hypothesis that RF sheath formation reduces the functionality of ICRF antennas is challenging in their natural environments inside of a tokamak plasma. This is mainly due to a lack of access to the region of interest, but also to a complex geometry.

Solving these issues are often the benefits of small specialized devices located in universities and laboratories adjacent to fusion experiments. IShTAR, Ion Cyclotron Sheath Test Arrangement, is one such facility operating at the Max Planck Institute for Plasma Physics in Garching, Germany. It is designed with a particular focus on the systematic study of the interaction between ICRF antennas and plasma. In order to do this, it offers the possibility to couple the waves launched from an ICRF antenna to a plasma representative of those found in the vicinity of the ICRF antennas in tokamaks, albeit in a simpler configuration and with improved diagnostics access.

The conditions that mimic the tokamak environment in IShTAR are a vacuum vessel with a curved wall, an ICRF antenna with RF ports, and a magnetized plasma near the antenna. The simplifications are a single-strap antenna with minimalistic casing and straight magnetic field lines perpendicular to the normal of the surface of the strap.

The plasma parameters must be kept relevant for the study, and affect the design of the plasma source and the ICRF operations. These are mainly the gas type, the magnetic field strength, plasma density and temperature. In order to remain in the relevant regime, the neutral gas pressure must be very low (at the order of, and below, 1 Pa). However, the formation of a low-pressure plasma in small linear devices is a non-trivial task, particularly when electron densities are required to match those found in the vicinity of the tokamak antenna. For these reasons the plasma breakdown in IShTAR is done in a helicon plasma source. Due to the fact that most of the research on the helicon discharges was carried out for argon or helium as the primary gas, and that there are not so many for hydrogen, IShTAR uses the first two. The preference of the main gas, in turn, determines the ICRF spectrum and, in order for the argon/helium plasma to remain relevant to the tokamak case, the plasma parameters are adjusted on the basis of Eq. 1.9 to match the dispersion relation of the fast wave for hydrogenic ions. This is further elaborated in [1.22], where choices of practical and plasma parameters for IShTAR are justified and specific values are tabulated.

As a result, IShTAR consists of two main compartments, as depicted in Fig. 1.4: the main vacuum vessel where the ICRF antenna is located and attached to transmission lines for ICRF power, and the helicon plasma source which is connected to the main vacuum vessel via an open port in such a way that the plasma it generates propagates as a column in front of the ICRF antenna.

The main vacuum vessel is a cylinder of a diameter of 1 m and a length of 1.126 m. There are 6 ports on its curved surface - on the antenna-side there are 3 horizontal ports where one is used for connecting to the RF transmission line, the other for vacuum pumps and pressure gauges, and the third is a window where the optical elements for the emission spectroscopy diagnostic are located (Chapter 3 of this manuscript). On the opposing side there is one hori-

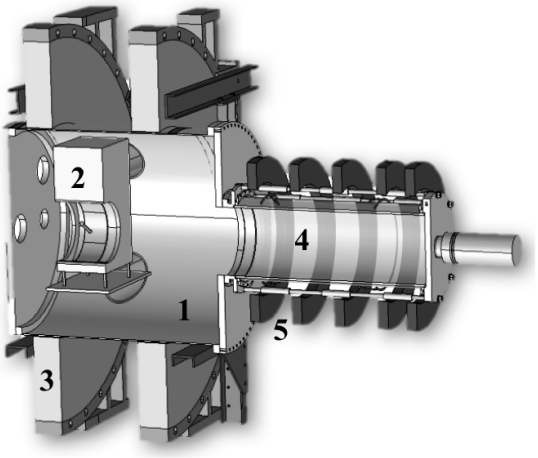

Figure 1.4: Illustration of IShTAR experimental device - an axial cut, to expose the in-vessel components: 1 - main vacuum vessel, 2 - ICRF antenna, 3 - "Big Coils", 4 - plasma source, 5 - "Small Coils".

zontal window and two ports angled at 30° - the upper is used for a radial manipulator mount, and the lower one is re-purposed as needed. The back flange has additional ports to further enable the access of diagnostic tools towards the ICRF antenna.

The magnetic field in the main vacuum vessel is produced by a set of two magnetic field coils looped around it in the Helmholtz configuration (referred to as the "Big Coils"). That way, the magnetic field lines are along the main axis of the vessel. The coils are attached to the central high current supply of the institute and operate with current pulses of up to 4 kA over 10 s to create a magnetic field up to 0.275 T in the center of the vessel.

The plasma source is a glass tube (0.4 m in diameter and 1 m in length) with 5 magnetic field coils ("Small Coils"), a helicon antenna with a matching system, a power supply and a gas injection valve. The power supply for the five Small Coils provides up to 1 kA, generating a magnetic field of 0.068 T in the middle of the plasma source. This magnetic field is superimposed to the one created by the Big Coils, and the combination of the two affects the plasma performance and the topology of the field lines in the vicinity of the ICRF antenna [1.23]. Helicon antenna itself delivers up to 700 W of power during the pre-amplification, in the "Low Power" phase and up to 3 kW when amplified, in the "High Power" phase, at a frequency of about 12 MHz.

The typical plasma electron density found in the main vacuum vessel of IShTAR is $n_e \approx 10^{17}\,\mathrm{m}^{-3}$ and electron temperature close to $T_e \approx 10\,\mathrm{eV}$.

The downside of having to use a plasma source with a helicon antenna is that it adds a new RF wave inside the plasma, which can make the interpretation of the purely experimental results complicated.

The vacuum system consists of a pre-vacuum pump which is efficient in lowering the pressure to $p_0 = 1\,\text{Pa}$ and a turbo-molecular pump for creating a high vacuum and $p_0 = 10^{-4}\,\text{Pa}$.

IShTAR's ICRF antenna is a curved single-strap antenna which follows the shape of the plasma column. The maximum RF power delivered to the ICRF antenna is 1 kW. The frequency of the ICRF waves is matched in vacuum to 5.9 MHz.

The diagnostic to characterize the ICRF antenna operation during the experiments performed for the purpose of this thesis was a voltage probe installed in the unmatched transmission (coaxial) line in combination with a directional coupler. The probe is installed about 5 m from the RF feeding port on IShTAR. The directional coupler is used to sample a small amount of the RF power to characterize the power coupled to the transmission line. The tandem of these two devices provide a qualitative estimate of the voltage standing wave ratio (VSWR) in the coaxial line of the ICRF system. A more precise estimate of the VSWR can allow for computing the loading resistance of the ICRF strap and eventually to estimate of the coupled power from the ICRF antenna to the plasma. However, the precise quantitative estimate of the VSWR was not possible in IShTAR without either a full array of voltage probes in the unmatched transmission line, or a pair of voltage and current probe at the same location.

1.5 Thesis objectives and scope

Understanding the phenomenon of the RF-induced rectified sheath potential at a fundamental level is an important step towards further optimization of the operational parameter space of ICRF antennas for the next-step fusion devices. Theoretical models for describing the RF sheaths around the plasma-facing antenna structures are under development. However, in order to verify the theoretical description of the parasitic effects to antenna activity against its actual operation, there is a lack of experimental information on the electric field in the sheath.

The aim of this doctoral thesis is to address that gap by designing an adequate diagnostic tool and methodology to provide experimental data on electric fields in the ICRF antenna sheaths.

The first stage of the project is a thorough review of the available measurement techniques. Among these, plasma spectroscopy is identified as the most appropriate option based on the conditions encountered in the vicinity of an ICRF antenna, which are, in the view of diagnostic development, considered

here to be a fundamental limiting factor for diagnostic applicability.

The use of spectroscopic methods to measure electric fields in low-pressure ($p_0 < 1\,\mathrm{Pa}$) low-density ($n_e < 10^{18}\,\mathrm{m}^{-3}$) plasmas is a rather unexplored domain. For this reason, the second stage of the thesis is a further analysis of the properties of emission spectra recorded in IShTAR's plasma. The purpose of the second stage is to define the possible diagnostic parameter that can be used to determine the electric field intensity directly from the measured spectra, and, thus also, the most optimal spectroscopic line(s). The additional requirement included into the assessment of the diagnostic parameter is that it should be independent of the optics used for diagnostic, i.e. the instrument. This means that the experimental profiles can be directly compared, if necessary, between different devices.

The third stage is a feasibility study in IShTAR, with a high-resolution spectrometer as the main component of the system. Only after the recorded spectra have shown that the available equipment is capable of detecting small wavelength shifts in high resolution, two operating schemes have been developed.

The diagnostic is developed in such a way that electric fields are measured in *i)* a configuration that provides sheath-integrated data (space-wise) and, *ii)* when aided by local trace-gas injection, a multi channel spectroscopy obtains data across the width of the sheath adjacent to the ICRF antenna in IShTAR. Given the fact that IShTAR was designed to match the parameter space found in the vicinity of ICRF antennas in tokamaks, the diagnostic method developed for the purpose of this thesis can thus be applied to any of these devices in a plug and play manner.

The focus of this project goes as far as the diagnostic development is concerned. Due to the lack of the RF sheath models tailored for geometry and parameters in IShTAR, the limit of the scope is set not to breach into comparing different available modelling codes.

1.6 Dissertation structure

Considering the objectives of this thesis, Section 1 of Chapter 2 sets out a comprehensive description of the sheath theory which gives rise to the electric field in question. A simple model of the expected electric field strengths is also presented here.

Existing diagnostic techniques are reviewed in Section 2 of Chapter 2, where they are gauged against the conditions found in the vicinity of the ICRF antenna in IShTAR and in tokamaks. This review pointed to the method that can be adopted to the specified conditions, thereby attempting to create another bridge in the knowledge base. This section presents a detailed rationale for choosing the diagnostic parameter for the application of Stark spectroscopy,

along with the choice on the spectroscopic line that is the focus of the diagnostic.

As the experimentally measured wavelength shifts due to an electric field in the studied medium are compared to the theoretical treatment of the Stark effect for reliable and direct measurements, the introduction to the effect from the point of view of atomic and quantum theory is given in Section 3 of Chapter 2. The task of theoretical calculations of the spectral line profile under the influence of the external electric (and magnetic) field is offloaded to the already existing code, EZSSS (Explicit Zeeman Stark Spectral Simulator) [1.24]. The theoretical description of the Stark effect is therefore presented through the calculation steps performed by this code, in particular when applied to the specific line and the parameter space of use for the research in this thesis.

The scientific contribution of this work is discussed in Chapter 3 where the experimental implementation of the diagnostic, and the data it provided, is shown for two configurations. The volume-integrated measurements in the sheath of the DC-powered electrode and in the sheath of an ICRF antenna are described in Section 3.1. The former is a proof of concept and the latter is the first such installation on any ICRF antenna. Section 3.2 outlines a diagnostic set-up and the data processing that go a step further, allowing spatially-resolved measurements of electric field across the width of the ICRF antenna sheath in IShTAR, which has never been done before. These two sections closely follow the publications [1.25] and [1.26]. The results of the Chapter are summarised in Section 3.3, where they are compared with the predictions of the model from Section 1 of the Chapter 2.

Chapter 4 presents the steps taken to improve the spectral resolution of the system, which lead to the improved resolution for the electric field measurements. These refer to the optimization in the calibration of the wavelength axis of the spectrometer's output, but also to the use of a derivative-free function optimization algorithm for the spectral line fitting and extraction of a more accurate wavelength from the experimental data. The Chapter ends with a step-by-step description and analysis of the different sources of uncertainty and how they propagate to the uncertainty in the measured electric field strength.

Following the concluding remarks, the outlook for the diagnostic as it is and further developments are proposed in the final chapter of the thesis.

References

[1] Nobel Media AB 2020 (n.a.). *The Nobel Peace Prize 2007*. https://www.nobelprize.org/prizes/peace/2007/summary/. [Online; accessed 02.11.2020.].

[2] David J.C. MacKay. *Sustainable Energy - without the hot air*. UIT Cambridge, 2008.

[3] BBC News (n.a.). *On This Day: October 17 (1956: Queen switches on nuclear power)*. http://news.bbc.co.uk/onthisday/hi/dates/stories/october/17/newsid_3147000/3147145.stm. [Online; accessed 02.11.2020.].

[4] World Nuclear Association. *World Nuclear Performance Report 2018*. Technical report, World Nuclear Association, aug 2018.

[5] J. Ongena and G. Van Oost. *Energy for Future Centuries: Prospects for Fusion Power as a Future Energy Source*. Fusion Science and Technology, 61(2T), 2012.

[6] Weston M Stacey. *Fusion Plasma Physics*. WILEY-VCH Verlag GmbH & Co. KGaA, Weinheim, second edition, 2012.

[7] Weston M Stacey. *Fusion*. WILEY-VCH Verlag GmbH & Co. KGaA, Weinheim, second edition, 2010.

[8] John Wesson. *Tokamaks. 3rd ed.*, volume 118. Oxford: Clarendon Press, 3rd ed. edition, 2004.

[9] Samuel Glasstone and Ralph H Lovberg. *Controlled thermonuclear reactions*. Van Nostrand Reinhold Co.Glasstone1960, Princeton, N.J., 1960.

[10] Amasa Stone Bishop. *Project Sherwood: The U.S. Program in Controlled Fusion*. Addison-Wesley Pub. Co, 1958.

[11] A.E. Costley, J. Hugill, and P.F. Buxton. *On the power and size of tokamak fusion pilot plants and reactors*. Nuclear Fusion, 55(3):033001, mar 2015.

[12] J. D. Lawson. *Some Criteria for a Power Producing Thermonuclear Reactor*. Proceedings of the Physical Society. Section B, 70(1):6–10, jan 1957.

[13] S.V. Mirnov. *Tokamak evolution and view to future*. Nuclear Fusion, 59(1):015001, jan 2019.

[14] A. S. Sharma, D. J. N. Limebeer, I. M. Jaimoukha, and J. B. Lister. *Modeling and control of TCV*. IEEE Transactions on Control Systems Technology, 13(3):356–369, 2005.

[15] ITER Physics Expert Group on Energetic Particles, Heating and Current Drive and ITER Physics Basis Editors. *Chapter 6: Plasma auxiliary heating and current drive.* Nuclear Fusion, 39(12):2495–2539, dec 1999.

[16] H. Takahashi. *ICRF heating in tokamaks.* Le Journal de Physique Colloques, 38(C6):C6–171–C6–190, dec 1977.

[17] A. Becoulet. *Heating and current drive regimes in the ion cyclotron range of frequency.* Plasma Physics and Controlled Fusion, 38(12A):A1–A11, dec 1996.

[18] T.H. Stix. *Waves in Plasmas.* American Inst. of Physics, 1992.

[19] R.A. Cairns. *Radiofrequency heating of plasmas.* Adam Hilger series on plasma physics. A. Hilger, 1991.

[20] V. Bobkov et al. *Impact of ICRF on the scrape-off layer and on plasma wall interactions: From present experiments to fusion reactor.* Nuclear Materials and Energy, 18(July 2018):131–140, jan 2019.

[21] J.R Myra, D.A D'Ippolito, D.A Russell, L.A Berry, E.F Jaeger, and M.D Carter. *Nonlinear ICRF-plasma interactions.* Nuclear Fusion, 46(7):S455–S468, jul 2006.

[22] Kristel Crombé et al. *A Test Facility to Investigate Sheath Effects during Ion Cyclotron Resonance Heating.* In Plasma science and technology : basic fundamentals and modern applications. IntechOpen, 2019.

[23] I. Shesterikov, K Crombe, A Kostic, D A Sitnikov, M Usoltceva, R Ochoukov, S Heuraux, J. Moritz, E. Faudot, F. Fischer, H. Faugel, H. Fünfgelder, G. Siegl, and J.-M. Noterdaeme. *IShTAR: A test facility to study the interaction between RF wave and edge plasmas.* Review of Scientific Instruments, 90(8):083506, aug 2019.

[24] *Electric field measurements of the capacitively coupled magnetized RF sheath utilizing passive optical emission spectroscopy.* Doctor of philosophy, North Carolina State University, 2014.

[25] A. Kostic, R. Dux, K. Crombé, A. Nikiforov, R. Ochoukov, I. Shesterikov, E. H. Martin, and J.-M. Noterdaeme. *Development of a spectroscopic diagnostic tool for electric field measurements in IShTAR (Ion cyclotron Sheath Test ARrangement).* Review of Scientific Instruments, 89(10):10D115, oct 2018.

[26] A. Kostic, K. Crombé, R. Dux, M. Griener, R. Ochoukov, I. Shesterikov, G. Suárez López, M. Usoltceva, R. Casagrande, E. H. Martin, and J.-M. Noterdaeme. *Polarization Stark spectroscopy for spatially resolved measurements of electric fields in the sheaths of ICRF antenna.* Review of Scientific Instruments, 90(12):123101, dec 2019.

2
Theoretical foundation

The material of this chapter is divided into three sections. The first consists of a review of the plasma sheaths, the RF-induced modifications of the sheath properties and the electric field which is the focus of the thesis objective. At the end of the section, a simple analytical model of the DC and RF-modulated sheath is given for the parameter space found in the IShTAR experiment. The choice of the diagnostic method and the diagnostic parameter for measuring the electric fields in the vicinity of an ICRF antenna is argued in the second section, with particular reference to the literature review on the subject. The aim of the third section is to provide the necessary contextual information on the atomic physics and Stark effect, as a diagnostic principle, that is used for optical assessment of electric fields. This information is given in the form of a brief guide to the EZSSS code used in the calculation of the synthetic spectra.

2.1 Plasma sheaths

In devices with magnetic confinement, plasmas are, as the name would suggest, enclosed by an externally-imposed magnetic field. Nevertheless, it is unavoidable that there is an interface where plasma encounters a material boundary (often simply referred to as *a wall*, even though this can be an electrode, a limiter surface, or the wall of the vacuum vessel).

Due to the large difference in their masses the thermal flux of electrons leaving the plasma towards the wall is much larger than that of the ions (Γ_e and Γ_i respectively):

$$\Gamma_e = \frac{n_e u_{T,e}}{4} = n_e \sqrt{\frac{kT_e}{2\pi m_e}}, \tag{2.1a}$$

$$\Gamma_i = \frac{n_i u_{T,i}}{4} = n_i \sqrt{\frac{kT_i}{2\pi m_i}} \tag{2.1b}$$

where $n_{e(i)}$ is denoting the density of the particle species, $m_{e(i)}$ their mass, $T_{e(i)}$ temperature and $u_{T,e(i)}$ thermal velocity of electrons (or ions), k is the Boltzmann constant, and the ions are assumed to be singly charged.

As the wall[1] accumulates the negative charges more rapidly, the plasma bulk becomes positively charged with respect to the material boundary, resulting in the formation of a positive potential barrier that restricts the electrons within the plasma and ensures equal charge flows to the material boundary, $\Gamma_e \approx \Gamma_i$. The wall potential for achieving this steady state of balanced fluxes is referred to as the *DC floating potential* [2.1–2.3].

The region through which the potential reaches zero in the plasma bulk, from a negative value at the wall, is of the order of few electron Debye lengths ($\lambda_{D,e}[cm] = 7.43 \times 10^2 \sqrt{T_e[eV]/n_e[cm^{-3}]}$ [2.4]) thick and is defined by the violated quasi-neutrality. The name for this layer - *sheath*, was coined by Irving Langmuir [2.5] even 5 years before he coined the term *plasma* [2.6].

With the negative potential established at the material boundary, the ions are accelerated into the wall, while most of the electrons (those with the average thermal velocity) are reflected off the potential barrier. The electron pressure gradient is therefore balanced by the electric field, E, that forces the electrons back into the plasma:

[1] Here it is assumed that the wall is electrically floating, i.e. that no direct bias is applied to the surface and that there is no possibility for the charges to drain away from the surface.

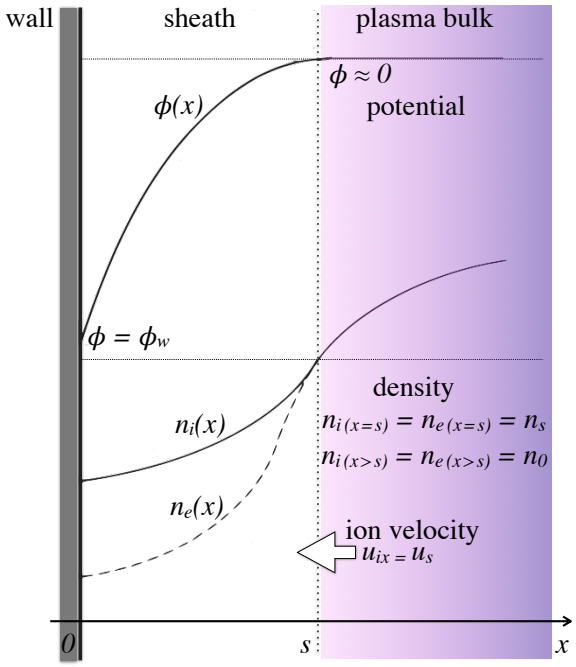

Figure 2.1: The behaviour of the potential ($\phi(x)$) and electron and ion densities ($n_e(x)$ and $n_i(x)$ respectively) in the sheath region ($0 < x < s$) nested between the plasma ($x > s$) and the adjacent wall ($x = 0$). Adapted from [2.1].

$$kT_e \frac{dn_e}{dx} = -n_e eE = n_e e \frac{d\phi}{dx}, \tag{2.2}$$

which leads to the Boltzmann equilibrium for the electron density

$$n_e(x) = n_s e^{e\phi(x)/kT_e}, \tag{2.3}$$

where n_s is density of the charges at the plasma-sheath interface, and ϕ is the potential.

When arriving to the sheath from the boundary between the sheath and the plasma $x = s$, where the particle density is $n_i = n_e = n_s$ and the potential $\phi \approx 0$, as shown in Figure 2.1, the ions, assumed to be a collision-free fluid, obey the dynamics that satisfy the continuity and momentum equations (here taken in one dimension only):

$$\frac{d}{dx}(n_i u_{i,x}) = 0 \Rightarrow n_i(x) u_{i,x}(x) = \text{const.} = n_s u_s, \tag{2.4}$$

$$\frac{1}{2}m_i u_{i,x}^2(x) = \frac{1}{2}m_i u_s^2 - e\phi(x) \Rightarrow u_{i,x}(x) = \sqrt{u_s^2 - \frac{2e\phi(x)}{m_i}}. \tag{2.5}$$

From the two, it follows that if the ions come out of the plasma bulk to the wall at a certain velocity u_s at the plasma-sheath interface $x = s$, due to the negative wall potential, the velocity of the ions as they fall through the sheath, $u_{i,x}(x)$, increases while their density decreases:

$$n_i(x) = \frac{n_s u_s}{u_{i,x}} = \frac{n_s}{\sqrt{1 - \frac{2e\phi(x)}{m_i u_s^2}}}. \tag{2.6}$$

The space charge in the sheath is thus, following the Boltzmann relation, Eq. 2.3, and Eq. 2.6 given as:

$$\rho = e(n_i(x) - n_e(x)) = en_s \left(\frac{1}{\sqrt{1 - \frac{2e\phi(x)}{m_i u_s^2}}} - e^{e\phi(x)/kT_e} \right). \tag{2.7}$$

The Poisson equation in one dimension, assuming that the potential is small ($|e\phi| \ll kT_e$), then reads as:

$$\begin{aligned} \frac{d^2\phi}{dx^2} &= -\frac{\rho}{\epsilon_0} = \frac{en_s}{\epsilon_0}\frac{e\phi(x)}{kT_e}\left(1 - \frac{T_e}{m_i u_s^2}\right) + \mathcal{O}\left(\left[\frac{e\phi}{kT_e}\right]^2\right) \\ \frac{d^2\phi}{dx^2} &= \frac{\phi(x)}{\lambda_{D,e}^2}\left(1 - \frac{v_s^2}{u_s^2}\right) + \mathcal{O}\left(\left[\frac{e\phi}{kT_e}\right]^2\right), \end{aligned} \tag{2.8}$$

where

$$\lambda_{D,e} = \sqrt{\frac{\epsilon_0 kT_e}{n_s e^2}} \tag{2.9}$$

is the electron Debye length in the proximity of the sheath-plasma interface, and

$$v_s = \sqrt{\frac{T_e}{m_i}} \tag{2.10}$$

is the sound speed of ions, assuming isothermal electrons and cold ions [2].

The non-oscillatory solution of the Poisson equation, Eq. 2.8, is that for which $v_s^2/u_s^2 > 1$ and yields the potential of the following structure:

[2] The general formula for the ion sound speed includes both the ion and electron temperatures against the mass of ions: $c_s = \sqrt{\gamma_e T_e + \gamma_i T_i / m_i}$, with $\gamma_{e,i}$ as the adiabatic indexes. However, in most of the laboratory plasmas $T_e \gg T_i \approx 0$ and for the constant electron temperature $\gamma_e = 1$.

$$\phi(x) \approx \phi_w e^{(x/\lambda_{D,e})\sqrt{1-v_s^2/u_s^2}}. \tag{2.11}$$

The negative potential that develops on the material boundary adjacent to plasma, ϕ_w, relaxes exponentially over the distance of the Debye length.

For the sheath to form it is necessary, as follows from the above derivation, for the ions to reach the sound speed when accelerated out of the plasma:

$$u_s = \sqrt{\frac{T_e}{m_i}} = u_B. \tag{2.12}$$

This is known as the Bohm sheath criterion [2.1, 2.3], with u_B denoting the Bohm velocity. It follows from here that a *pre-sheath* region of a small but non-zero potential is formed to allow the ions to accelerate to the sound speed indicated by the Bohm criterion.

It is useful to evaluate what is the potential drop, $\Delta\phi$, required to accelerate plasma ions from rest to Bohm velocity, u_B. Since in the plasma the ions are assumed heavy, cold and therefore presumed to be at rest, and the plasma potential is $\phi \approx 0$, the momentum equation for the ions in the plasma is:

$$\frac{1}{2} m_i u_{i,x}^2(x) + e\phi(x) = 0, \qquad \text{for} \quad x > s. \tag{2.13}$$

Substituting $\Delta\phi$ for ϕ and Eq. 2.12 for $u_{i,x}(x)$ yields:

$$\Delta\phi = \frac{kT_e}{2e}. \tag{2.14}$$

Therefore, in order to meet the Bohm criterion from the plasma side, the potential difference between the center of the plasma bulk and the boundary between the plasma and the sheath must be as found in Eq. 2.14. Since for $x > s$ the Boltzmann distribution for ions still holds, this argument suggests that the ion density at the plasma-sheath boundary, n_s, is ≈ 60% of the value found in the center n_0:

$$\frac{n_s}{n_0} = e^{\left(-\frac{1}{2}\right)} \approx 0.6. \tag{2.15}$$

Under these conditions, the particle flux balance can be re-examined to evaluate the steady-state DC floating potential of the wall, V_f^{DC}. The ion flux from the plasma to the sheath, Γ_i must be equal to the flux of ions at the wall, Γ_w:

$$\Gamma_i = n_s u_B = \Gamma_w. \tag{2.16}$$

On the other hand, the electron flux, Γ_e is:

$$\Gamma_e = n_s \sqrt{\frac{kT_e}{2\pi m_e}} e^{eV_f^{DC}/kTe}. \tag{2.17}$$

The particle flux balance, $\Gamma_e = \Gamma_i$, leads to the formula for the floating potential of the wall adjacent to the plasma, with respect to the potential at the plasma - sheath interface:

$$V_f^{DC} = \frac{kT_e}{e}\frac{1}{2}\ln\left(\frac{2\pi m_e}{m_i}\right) \tag{2.18}$$

The resulting electric field in the sheath is directed towards the material boundary, with an intensity of $\approx kT_e/e\lambda_{D,e}$. The electric field in the pre-sheath region is non-zero, however very small.

In this description, there is no magnetic field imposed on the plasma. If it existed, the orientation of the magnetic field vector that would be of interest to the work presented in this manuscript is parallel to the normal of the plasma-facing surface of the wall. In that case, the above geometry does not change, as the magnetic field does not influence the parallel motion of the confined particles, and thus the one-dimensional limitation would be maintained. The only addition, which would be for an oblique angle between the magnetic field and the normal of the surface, is the so-called *magnetic* or *Chodura pre-sheath* extending the width of the intermediate region between the quasi-neutral bulk plasma and the electron-depleted sheath [2.7].

2.1.1 The influence of the RF on the sheath properties

Sheath dynamics will be introduced once an RF voltage is applied across the material boundary facing the plasma [2.1].

However, since "RF" is a term that encompasses a whole spectrum of frequencies, the sheath dynamics may vary depending on the frequency of the applied voltage signal relative to electron and ion plasma frequencies, as different plasma particles are less or more responsive to the oscillating potential due to their inertia. A frequency classification is therefore helpful. The main parameters for this are the electron and ion plasma frequencies, and how they compare to the frequency of the applied modulation:

$$f_{p,e}[\mathrm{Hz}] = \frac{\omega_{p,e}}{2\pi} = \frac{1}{2\pi}\sqrt{\frac{n_{0,e}e^2}{m_e\epsilon_0}} \approx 9\sqrt{n_{0,e}[\mathrm{m}^{-3}]}, \tag{2.19}$$

$$f_{p,i}[\mathrm{Hz}] = \frac{\omega_{p,i}}{2\pi} = \frac{1}{2\pi}\sqrt{\frac{n_{0,i}Z^2e^2}{m_i\epsilon_0}}. \tag{2.20}$$

Table 2.1 lists the ion plasma frequency for singly ionized argon, helium and hydrogen plasmas, for the particle density in the plasma close the sheath within

plasma	$f_{p,i}$ [MHz]
Ar	$0.104 - 3.32$
He	$0.332 - 10.5$
H	$0.662 - 20.9$

Table 2.1: Ion plasma frequency of plasmas relevant for this thesis, with dominant singly-ionized species, for the ion density near the sheath of the order of $n_{0,e} = n_{0,i} = 10^{13} - 10^{16}\, m^{-3}$.

the following range $n_e = n_i = 10^{13} - 10^{16}\,\mathrm{m}^{-3}$. In tokamaks, the applied ICRF frequency is typically several tens of MHz, and in smaller devices such as IShTAR (Section 1.4) it is of the order of 5 MHz for argon and helium plasma. The electron plasma frequency of such plasmas is in the GHz range.

For the cases considered in this work that are relevant to the operation of ICRF systems in fusion devices, the standard ordering of the frequencies is therefore $\omega_{p,i} < \omega \ll \omega_{p,e}$. This is referred to as *the high-frequency region* [2.1] and, if a collision-less sheath is assumed for the purpose of a qualitative description, the plasma ions can not follow the frequency of an oscillating RF field. This implies that the ion dynamic is determined by the time-averaged electric field in the sheath, i.e the average sheath potential. On the other hand, the electrons instantly follow the changes, due to a Boltzmann distribution, which carries a dependency on an instantaneous potential ϕ, Eq. 2.3.

So does the sheath-plasma boundary. With the periodic movement of this boundary, the displacement of charges[3] averages to zero. However, the particle currents, i.e. the electron/ion fluxes, do not need to average to a net-zero value over an RF cycle. In order to ensure that no net-current passes through the sheath region, the conditions emerge to equate the RF-cycle-averaged electron flux to the steady state flux of ions.

In the steady state (DC) sheath conditions, these fluxes are balanced when the wall potential reaches the value referred to as the DC floating potential, V_f^{DC}, Eq. 2.18.

In the case when an RF voltage $V\sin(\omega t)$ is supplied to the surface, the balance of the particle fluxes becomes:

$$\left\langle n_s \sqrt{\frac{kT_e}{2\pi m_e}}\, e^{e(V\sin(\omega t)+V_f^{RF})/kT_e} \right\rangle_{(2\pi/\omega)} = n_s u_B,$$

where the electron flux, the left-hand side of the equation, is an average over an RF period, $2\pi/\omega$, and contains an additional term - the to-be-determined

[3] E.g. the density of electrons pushed back into the plasma with a certain velocity.

RF floating potential, V_f^{RF}. The expression between the angled brackets is an integral of the form

$$\omega/2\pi \int_0^{2\pi/\omega} e^{\mathrm{a}\sin(\omega t)}\, dt = I_0(\mathrm{a}),$$

where $I_0(\mathrm{a})$ is a modified Bessel function of the zeroth order[4]. The property of this solution is that such function tends to unity for the small values of an argument, and becomes an exponential for the large ones.

This leads to the floating potential of the surface due to the RF bias to adopt the following form:

$$V_f^{RF} = \frac{kT_e}{e}\left[\frac{1}{2}\ln\left(\frac{2\pi m_e}{m_i}\right) - \ln\left(I_0\left(\frac{eV}{kT_e}\right)\right)\right]. \tag{2.21}$$

Compared to the DC floating potential and resulting from the RF voltage supplied to the surface, Eq. 2.21 has an additional DC term in order to adjust the potential barrier across the sheath and equalize the particle fluxes from the plasma. This is referred to as the *RF self-bias*. Due to the shape of the $I_0(\mathrm{a})$ function, the floating potential is close to the DC value for $V < kT_e/e$ and approaches the RF amplitude for $V \gg kT_e/e$.

The contemporary ICRF community is interested in this RF-induced DC potential drop or, more specifically, its gradient, i.e. the DC electric field across the sheath. This electric field accelerates the plasma ion species beyond the Bohm velocity towards the material surfaces, leading to detrimental effects for both the core reactor plasma (by generating impurities due to increased sputtering of the material structures of the antenna box) and the antenna itself (as it can cause the hot spots).

However, in the domain of an ICRF antenna - plasma interaction studies, the presented modification of the sheath potential is not only due to the direct supply of the RF voltage to the structures. The non-zero oscillating electric field of an ICRF wave at the plasma-sheath boundary, that is parallel to the electric field within the steady state DC sheath also directly influences the sheath potential in a way that is descriptively the same as if the surface was powered with an RF voltage, even when that surface is "passive". The term *sheath-rectification* [2.8] is used to label this type of the RF-caused change on the sheath potential that occurs from an ICRF wave-induced oscillating sheath-plasma boundary. This phenomenon is illustrated in Fig. 2.2. It depicts the current of the particles on the wall for various values of the potential difference between the plasma and the wall.

The effect of the operation of the ICRF antenna on the potential through the sheath surrounding antenna's passive structures is therefore indirect. To account numerically for these effects, the modelling codes would ideally have to

[4]The shape of the single order modified Bessel function, $I_0(\mathrm{a})$, and the solution of Eq. 2.21 are given in the Appendix, A.2.

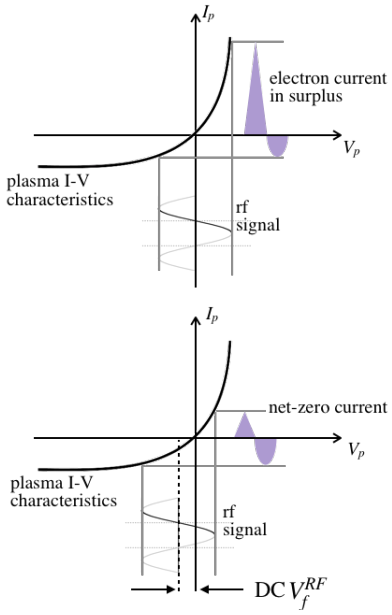

Figure 2.2: Sheath rectification on the current-voltage characteristics, showing the adjusted potential to preserve net-zero current. Adapted from [2.8].

treat the sheath kinetics (within a few Debye lengths) along with the wave propagation at the edge of the tokamak plasma (Section 1.3), at the spatial scales orders of magnitude different. The issue of scales is typically bypassed by incorporating the RF sheath effects (such as the enhanced potential) as constrains imposed by a set of boundary conditions [2.9, 2.10].

In the models with this approach, the sheath is introduced as a thin vacuum layer of a certain effective impedance in between the perfectly conductive wall and the plasma. This layer covers a certain area A in an yz plane (normal to the x-direction in Fig.2.1). The sheath boundary condition that enters the simulations codes modelling the behaviour of the RF waves and their interaction with the edge plasma has the following general form[5], according to [2.10]:

$$\vec{E}_t = -\nabla_t V_s h = \nabla_t \left(\frac{\omega}{4\pi i} D_n Z \right), \tag{2.22}$$

where the tangential (to the sheath-plasma interface, thus here laying in the yz plane) electric field is evaluated on the plasma side of the sheath-plasma boundary and is given as the (tangential) gradient of the sheath potential which is also taken from the plasma side of the boundary. This potential is expressed

[5]Typically the codes that do implement the sheath boundary conditions can handle only a 2D simulation domain, which implies a one-dimensional boundaries.

through the total current density across the sheath, $J = J_n$, related to the normal component of the electric displacement D_n by $D_n = J_n 4\pi i/\omega$, and the effective RF sheath impedance Z. This quantity $Z(\omega)$ is defined in a way to include both the capacitive and resistive impedance. In the limit of $Z = 0$ the typical boundary conditions for the perfectly conducting wall: $\vec{E}_t = 0$ are retrieved, [2.10], as if the sheath does not exist.

Changes in the potential across the sheath that are due to the activity of the RF wave at the frequency ω are seen from the plasma side and in the plane tangential to the sheath-plasma boundary. For the experimental verification of these boundary conditions, it is essential to provide data on the corresponding rectified electric field. In addition, the distribution of this electric field across the width of the sheath is equally important in order to understand the rectification processes in the ICRF antenna sheaths and to examine the validity of the assumptions made in the derivation and implementation of the sheath boundary conditions.

2.1.2 Basic analytical model of electrostatic and RF-modulated sheath

Although sophisticated models of the sheath and the particle dynamics in the sheath exist and are continuously improving, it is important to survey the expected values and behaviours for quantities which are to be determined experimentally. A basic analysis (which mainly follows [2.1]) is therefore presented in this section and applied to the parameters encountered in IShTAR (Section 1.4 and the box below), while still staying within the scope of this thesis.

For the rest of the analysis, the following plasma configuration is assumed, unless other values for a given parameter are explicitly stated.

- Either Ar or He is used as working gasses.
- The neutral gas pressure is $p = 0.01\,\text{Pa}$.
- The electron plasma density is $n_0 = 10^{16}\,\text{m}^{-3}$. The density at the plasma-sheath boundary is calculated according to Eq. 2.15: $n_s = 0.6 n_0$.

One of the most important features of the laboratory-made cold, low-pressure plasma which is sustained by an external ionization source, such as the one created in IShTAR, is that it is far from the thermodynamic equilibrium. As a consequence, the electrons have temperatures between 2 and 10 eV, while the ions remain close to the neutral gas temperature ($\approx 0.05\,\text{eV}$).

- The plasma in the crude model used for the sheath analysis in this sec-

tion is presumed to have the same behaviour, with the electron temperature $kT_e = 5\,\text{eV}$ and the ion temperature $kT_i = 0.05\,\text{eV}$.

This further implies the following parameters:

- The electron Debye length is $\lambda_{D,e} = 0.1662\,\text{mm}$,
- The electron plasma frequency is $\omega_{p,e} = 5.64 \times 10^9\,\text{s}^{-1}$
  - or $f_{p,e} = 0.9\,\text{GHz}$,
  - and the electron response time, $\tau_e = \omega_{p,e}^{-1} = 0.018\,\text{ns}$,
- The ion plasma frequency in argon plasma is $\omega_{p,i}^{Ar} = 2.0906 \times 10^7\,\text{s}^{-1}$
  - or $f_{p,i}^{Ar} = 3.3272\,\text{MHz}$,
  - and the response time of the argon ion $\tau_i^{Ar} = 47.83\,\text{ns}$,
- The ion plasma frequency in helium plasma is $\omega_{p,i}^{He} = 6.6045 \times 10^7\,\text{s}^{-1}$
  - or $f_{p,i}^{He} = 1.0511\,\text{MHz}$,
  - and the response time of the helium ion $\tau_i^{He} = 15.14\,\text{ns}$.

The geometry of the problem is like that in Fig. 2.1. It is one-dimensional and restricted to the wall ($x = 0$), the sheath ($0 < x < s$) and the immediate surroundings of the sheath-plasma boundary ($x \geqslant s$). The center of the plasma, where $n_i = n_e = n_0$, is considered to be far enough ($x \gg s$).

The first set of simplifications is to assume that ionization processes are far away from the sheath, stating that the mean free path for ionization collisions is greater than the sheath width. Elastic collisions are also assumed to be unimportant, which means that the sheath is narrower even when compared to the mean free path for elastic collisions. The wall is an infinite plane perpendicular to the x-axis, following the geometry sketched in Fig. 2.1. As discussed in Section 2.1, plasma potential is assumed to be at $V_p = 0$.

The concept of the sheath that is used for this analysis is referred to as *the homogeneous sheath model*. The adjective refers to the ion density in the sheath, which is assumed to be constant and equal to that present at the sheath-plasma boundary:

$$n_i(x < s) = n_i(x \geqslant s) = n_s. \tag{2.23}$$

This concept is sometimes referred to as the "ion-matrix sheath", or the "step-function sheath", as it assumes that the ions make a uniform matrix of space charge across the sheath, while the potential of the wall is already large enough to sweep away all the electrons from the sheath region. The electron density is

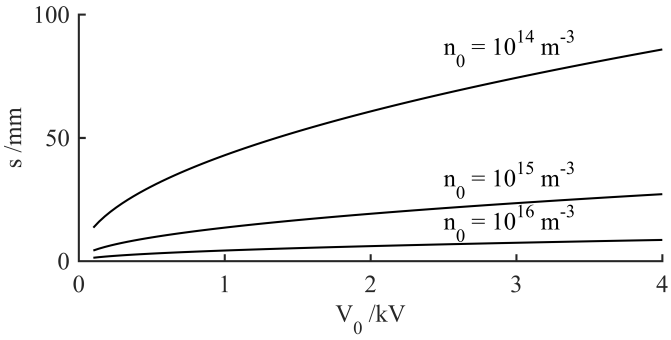

Figure 2.3: The width of an electrostatic (DC) sheath as a function of an imposed voltage at the wall, for various plasma densities.

assumed to be equal to the ion density at the sheath-plasma boundary:

$$\begin{aligned} n_e(x) &= 0, \qquad \text{for} \quad x < s, \\ &= n_s, \qquad \text{for} \quad x \geqslant s. \end{aligned} \tag{2.24}$$

Already from Eq. 2.3, it can be seen that, in order to reduce the electron density as much as to the 1% of its value at the sheath-plasma boundary ($n_e = {}^{n_s}/_{100}$), the imposed potential at the wall is:

$$V_0 = \ln\left(\frac{1}{100}\right)\frac{kT_e}{e} = -4.6\frac{kT_e}{e}, \tag{2.25}$$

which for $kT_e = 5\,\text{eV}$ is already at $V_0 = 23\,\text{V}$. Because the values of the applied potential at the wall are typically far greater than this value, electron density in the modelled plasma sheath can be safely ignored.

On the other hand, the Poisson equation Eq. 2.8 must be satisfied, now with the re-defined charge density ρ.

For $\rho = en_s$, the Poisson equation becomes:

$$\frac{d^2\phi}{dx^2} = -\frac{en_s}{\epsilon_0}. \tag{2.26}$$

The electric field ($E = -{}^{d\phi}/_{dx}$) is assumed to vanish at the sheath-plasma boundary $x = s$, and the potential in the plasma and its boundary with the sheath is set to $V_p = \phi(x \geqslant s) = 0$. These constraints are the boundary conditions for the two-times integrated Poisson equation, which gives the following form of the potential through the homogeneous sheath:

$$\phi(x) = -\frac{en_s}{2\epsilon_0}(x-s)^2. \tag{2.27}$$

When the potential at the wall is set to $\phi(0) = -V_0$ with respect to the plasma, Eq. 2.27 gives an estimate of the width of the electrostatic (DC) sheath:

$$s = \sqrt{\frac{2V_0\epsilon_0}{en_s}}. \tag{2.28}$$

Figure 2.3 is a graphical representation of this relation, where s is given as a function of the wall potential evaluated at several fixed values of plasma density.

RF-modulated sheath

The geometry of the problem of the RF modulation imposed on the homogeneous sheath can be sketched as in Fig. 2.4 with the sheath-plasma boundary oscillating in time, $s(t)$.

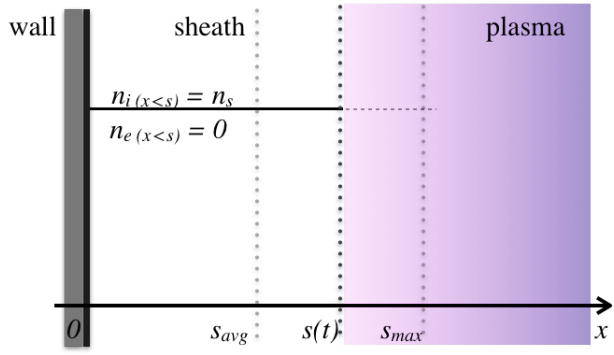

Figure 2.4: RF-modulated homogeneous sheath ($n_e(x < s(t)) = 0$ and $n_i(x < s(t)) = n_s$) with time-varying sheath-plasma boundary. s_{max} and s_{avg} denote the maximum outstretch of the sheath from the electrode, and the average sheath width, respectively.

Integrating the Gauss law for the homogeneous sheath:

$$\frac{\partial E}{\partial x} = \frac{n_s e}{\epsilon_0}\left(1 - e^{\frac{e\phi}{kT_e}}\right), \tag{2.29}$$

under the assumption that $E = 0$ at the sheath-plasma boundary $x = s(t)$, gives the following expression for the electric field at any point of time and space:

$$E(x,t) = \frac{n_s e}{\epsilon_0}\left(x - s(t)\right). \tag{2.30}$$

The sheath-plasma boundary, $s(t)$, must be described prior to obtaining an equation for the time-averaged electric field in the RF modulated sheath.

In order to examine the condition that is most likely to occur in the sheaths of an ICRF antenna, a choice is made to impose a current-driven, instead of the

voltage-driven, RF modulation of the sheath properties. It can be presumed that the current density which passes through the sheath has a sinusoidal waveform:

$$J(t) = -j_0 \sin(\omega t). \tag{2.31}$$

This leads to the Maxwell's displacement current defined as:

$$\epsilon_0 \frac{\partial E}{\partial t} = -n_s e \frac{ds}{dt} = -j_0 \sin(\omega t). \tag{2.32}$$

It follows therefore, that the sheath-plasma boundary oscillates as

$$s(t) = s_{avg} - s_0 \cos(\omega t), \tag{2.33}$$

with an amplitude

$$s_0 = \frac{j_0}{n_s e \omega}. \tag{2.34}$$

If the externally imposed RF current is sufficiently high, the sheath boundary motion will follow the oscillations of this high current and, as a consequence, the sheath will collapse once per each cycle. When this occurs, there is no potential difference between the wall and the plasma, so that

$$s_{avg} = s_0 = \frac{j_0}{n_s e \omega}, \tag{2.35}$$

which leads to a simplified expression for $s(t)$, and with that to:

$$E(x,t) = \frac{n_s e}{\epsilon_0} \left(x - s_0(1 - \cos(\omega t))\right), \qquad \text{for} \quad x < s(t). \tag{2.36}$$

To set the boundary conditions for the integration with respect to ωt, only half of the cycle can be considered, while enforcing that at $\omega t = 0$ the sheath collapses and at $\omega t = \pi$ it reaches its maximum width. At a distinct instance of time, t', the sheath-plasma boundary, where the electric field vanishes, is given as $\omega t' = \cos^{-1}\left(\frac{s_0 - x}{s_0}\right)$. Therefore, to obtain the time-averaged electric field inside the sheath, Eq. 2.36 is integrated from $\omega t = \omega t'$ to $\omega t = \pi$:

$$\begin{aligned} \bar{E}(x) &= \frac{1}{\pi} \int_{\cos^{-1}\left(\frac{s_0 - x}{s_0}\right)}^{\pi} E(x,t), \mathrm{d}(\omega t) \\ &= \frac{n_s e}{\pi \epsilon_0} \left[-s_0 \sqrt{\frac{(2s_0 - x)x}{s_0^2}} - (s_0 - x)\left(\pi - \cos^{-1}\left(1 - \frac{x}{s_0}\right)\right)\right]. \end{aligned} \tag{2.37}$$

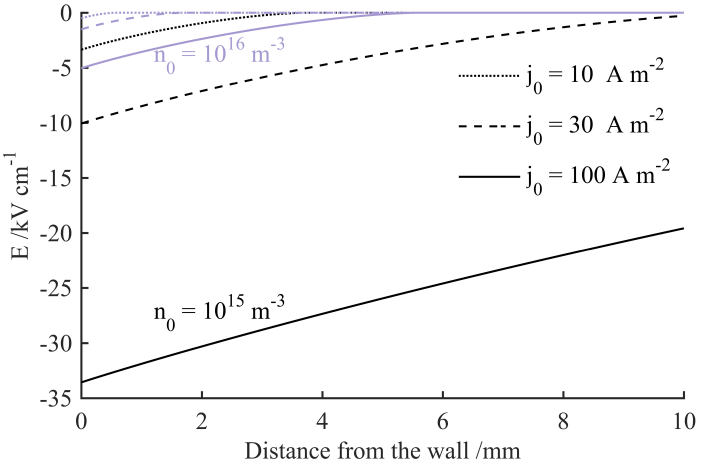

Figure 2.5: The time-averaged electric field evaluated, according to Eq. 2.36, within the first 10 *mm from the wall for three values of current density,* $j_0 = 10, 30$ *and* $100\,Am^{-2}$*, represented with the dotted, dashed, and a solid line shape respectively, and for two values of plasma density for which the results are colour-coded -* $n_0 = 10^{15}$ *and* $10^{16}\,m^{-3}$ *in black and purple, respectively.*

Figure 2.5 shows the spatial distribution of the time-averaged electric field within the first 10 mm from the wall. Eq. 2.37 is solved for two values of plasma density, $n_0 = 10^{15}\,\mathrm{m}^{-3}$ and $n_0 = 10^{16}\,\mathrm{m}^{-3}$, and each of these for three increments of the amplitude of the RF current, $j_0 = 10, 30$ and $100\,\mathrm{Am}^{-2}$. The oscillation frequency was set as equal to the frequency of an ICRF antenna in IShTAR, $\omega = 2\pi \times 5.94\,\mathrm{MHz}$. The limit $E = 0\,\mathrm{kV\,cm}^{-1}$ conveniently also shows how plasma density and the current amplitude affect the average sheath width.

The values calculated or derived in this section are used to qualitatively gauge the experimental results in Chapter 3.

2.2 Spectroscopic measurements of electric fields

When an electric field is present in the medium, it induces anisotropy throughout the area of its effect. These anisotropies, such as the change in the refractive index of a transparent material (the basis of the electro-optical methods [2.11–2.13]), the externally-induced separation of charges in an electrically conductive material (in some electrostatic probes and sensors [2.14]), or the modified optical spectra (as shown in the following discussion), are quantifiable and are the established basis of the sensors and diagnostics for measuring the strength of the imposed electric field. The argument for selecting the appropriate diagnostic method for the task addressed in this thesis, and an accompanied diagnostic parameter, is presented in this section.

The first-order restrictions that help to filter out the unsuitable methods are imposed by the RF sheath rectification phenomenon in the vicinity of the ICRF antenna. These are:

1. The intensity of the electric field in the sheath is between 0 and a few tens of kV/cm.

2. The sheath width on the frame of an ICRF antenna is between a few tenths of a mm to a few cm.

3. The diagnostic must not be invasive.

For these reasons, plasma spectroscopy is chosen as already a standard tool to measure electric fields in the sheath region in different types of discharges.

Plasma spectroscopy is an experimental field concerned with the emission, absorption or scattering of the electromagnetic radiation by atoms, molecules or ions contained in the region of interest [2.15]. The information collected is presented as a spectrum: a measure of radiation intensity as a function of wavelength, frequency or wave number. With proper interpretation of the recorded spectra, spectroscopy goes beyond its initial role in the development of atomic physics and quantum theory, becoming a powerful set of diagnostic methods for plasma parameters. The diagnostic method discussed trough this thesis manuscript is based on passive optical emission spectroscopy (Section 3.1, and [2.16]) and active optical emission spectroscopy, using locally injected helium gas as a probe (Section 3.2, and [2.17]).

It may seem surprising to attempt to use diagnostic methods that rely on the existence of emissive species to characterize the plasma sheath which is defined as a predominantly dark region of a discharge. However, the experimental studies on the particle dynamics in the RF-driven sheaths suggest that the electron-impact excitation of the main ion and atom species in the sheath is likely to

occur throughout most of the RF cycle, while the heavy-particle collisional excitation is also a mechanism which induces ample emission to use spectroscopy as a tool to characterize RF sheaths [2.18].

Diagnostic parameter

Several properties of emission spectra can be used as a diagnostic parameter to measure the external electric fields present in the edge regions of the plasma. The emission spectrum changes with the electric field strength at the location of the emitter. These changes include changes in relative intensities, splitting of spectral lines, the appearance of new spectral lines, and shifts in the line's wavelength. This dependence of the emission spectrum on the electric field strength is called the Stark effect. Various spectroscopic methods based on the Stark effect have been developed for measuring electric fields in plasmas [2.19–2.22].

The choices of the appropriate diagnostic parameter and the correct spectroscopic technique are directly related to the second-order constraints imposed on a diagnostic for measuring electric fields in the sheaths adjacent to the passive structures of the ICRF antennas - the plasma and sheath environment itself. Plasma and sheath parameters influence emission spectra and, in some cases, pose a constraint.

Gas pressure is a factor limiting the use of laser techniques in the experiments presented in this dissertation. These diagnostic tools are developed for, and widely used in, high pressure glow discharge plasmas, at pressures of up to $10^2 - 10^4$ Pa. Such high pressures ensure high enough density of the atomic species, especially those in the excited (metastable) states needed to absorb the laser light by a reliable amount for a good spectroscopic signal intensity. A notable exception here is the work of K. Takiyama and colleagues, [2.23], who have developed a method for using Stark spectroscopy with a laser induced fluorescence (LIF) for tokamak edge plasma conditions, albeit with a pulsed supersonic helium beam injection system that provides sufficient density of helium atoms (10^{20} atoms cm^{-2} s^{-1}). In comparison, the operating base gas pressures in the experiments relevant to the ICRF sheath studies are at the order of, and sometimes far below, 1 Pa (in the immediate vicinity of ICRF antennas) [2.24, 2.25].

Gas pressure is affecting the topic on ICRF sheaths through the treatment of collisions. As noted in [2.26] and [2.2], Liebermann indicated that the collisional limit of the RF sheath applies when the gas pressure is greater than 5 Pa, at which point the ion mean free path becomes much smaller than the sheath width. Thus the treatment of the two experimental regimes is different, and the diagnostic method must be consistent with conditions assumed in the physics description of the RF sheath rectification and the sheath models. Moreover,

as discussed in Section 1.4, IShTAR is designed to come as close as possible to the neutral pressure encountered in the tokamak plasma periphery in order to maintain the relevant and comparable conditions.

The electron density is the other limiting parameter. It was observed experimentally that, in addition to causing Stark broadening (influenced by the electric field from the surrounding charged particles in a plasma) in the high electron density region, when this parameter is below $n_e \leq 10^{20}\,\mathrm{m}^{-3}$, the intensity of new spectral components (known as the *forbidden* lines) as well as the dip between them and the corresponding allowed component on the spectra show a strong dependency on the electron density [2.27–2.30]. As a result, these "forbidden" components are inaccessible in plasma environments relevant to fundamental investigation of ICRF antenna behaviour, and so are the spectroscopic methods that rely on them, due to very low plasma density.

The other plasma parameters, such as ion and electron temperature and the temperature of the injected trace gas, have an effect on the spectral line profile, but do not limit the applicability of the methods.

Based on the above limitations, the diagnostic parameter chosen for the purpose of this thesis project is the wavelength shift of the *allowed* line from its unperturbed value. It is experimentally determined from the position of the peak of the line profile and is compared between the value measured in the experiment and the position of the line, attributed to the same atomic transition, emitted from the calibration lamp source (referred to as the *unperturbed wavelength*). This parameter does not depend on the instrument, so it can be used to compare the results obtained from different experiments.

In the region of interest, for the measurements in the vicinity of an ICRF antenna, this parameter is not affected by the $E \times B$ drift as the emission is obtained from the neutral atom species and the vectors of the two fields are parallel to each other. Furthermore, while the magnetic field is present in the vicinity of IShTAR's ICRF antenna, its magnitude is too low to induce visible changes in the spectral line profile described by the Zeeman effect. Therefore, in all cases studied within the scope of this thesis, only the external uni-directional electric field is considered as being able to modify the chosen diagnostic parameter - the shift of the allowed component of the spectra.

As shown in Chapter 3, the electric field is extracted from the measured spectra by comparing the experimental spectral line shift with the theoretical models based on the atomic and quantum theory of the Stark effect.

Line selection

Another important element that needs to be addressed is the choice of the emitter and the spectral wavelength used for the diagnostic purposes. With the previous discussion on method and parameter in mind, both the atomic theory and

the experiment themselves influence the selection of the appropriate atomic species. The Stark effect on the spectrum of atoms of light elements is easier to calculate, being analytically accurate in the case of hydrogen, while some assumptions must already be made in the case of helium (this will be discussed in the following section).

On the practical side, argon and helium are the only two gasses that are available at IShTAR. In order to be treated as a hydrogen-like ion (isoelectronic with hydrogen), the argon atom must be ionized to lose 17 of its electrons and is therefore impractical as an atomic probe for active diagnostic. On the other hand, helium is routinely used as a trace gas for spectroscopy in tokamaks (which is a prospect of this work, Chapter 4), where the bulk plasma consists of hydrogen species.

As the choice of the emitter is set to helium, the final point is the selection of the spectral line that is the focus of the diagnostic. W. Hicks outlined in [2.31] the main points that are to be considered when choosing a helium spectral line for diagnostic purposes. From the perspective of atomic theory, the following must be taken into account when considering the Stark effect on the spectrum of neutral helium:

1. The singlet and triplet states are considered separately.
2. The states with the principle quantum number $n \leq 3$ are considered insensitive to electric fields.
3. For the states with $n \geq 4$, only the high angular momentum states should be retained (P, D, F, ...).

On the other hand, limited by the emission spectra in IShTAR's plasma and the optical range of the instrument, the choice is narrowed to the spectral line corresponding to the 4^3D - 2^3P transition of a neutral helium atom. Here the optical transition occurs from the energy level with $n = 4$ to the one $n = 2$, both described with a triplet state. The transition between their singlet counterparts is outside of the optical range of the spectroscopic system used for this thesis.

2.3 Theoretical treatment of the Stark effect

Optical emission spectroscopy, particularly the passive technique, relies on the spontaneous emission of electromagnetic radiation from a radiating particle species in a plasma. Spontaneous emission is a process of de-excitation during which an atom relaxes from a quantum state with a higher energy (E_H) to a state with a lower energy (E_L) through the emission of a photon with $E = E_H - E_L$. The resulting central wavelength[6] of this light emission is given by

$$\lambda_0 = \frac{hc}{E_H - E_L}. \tag{2.38}$$

This formula highlights a strong relation between the emission spectra and the atomic structure. The latter is theoretically defined with the aid of quantum mechanics, where the wave functions as a solution to the Schrödinger equation describe a stationary state of an atom with a definite energy. The energies of an upper and lower level of the above system, E_H and E_L respectively, are the result of such calculations.

In most of plasma spectroscopy applications the energy structure of an emitter is assumed given [2.32]. Nevertheless, the calculation of the energy structure and transition probabilities is critical in the case of the Stark effect spectroscopy. This is because the effect results in shifting and splitting of the energy levels of an emitter when it is placed in an external electric field.

For this thesis, the theoretical calculation of the atomic structure, and the resulting spectral line shape, due to the external electric and magnetic field were carried out using the EZSSS (Explicit Zeeman Stark Spectral Simulator) code, developed at the Oak Ridge National Laboratory, Oak Ridge, USA, and described in detail in [2.33]. What follows is a brief description of the three stages of EZSSS computation of spectral line profile and wavelength.

Step One: External fields as perturbations

In this context, the Schrödinger equation is typically solved using the perturbation theory. In that case, it is assumed that the Hamiltonian H can be separated into a sum of H^0 , for which the corresponding Schrödinger equation can be precisely solved, and the terms considered to be perturbations. The Schrödinger equation of the one-electron atom in external magnetic and electric field has, in general, the following form:

$$i\hbar\frac{\partial\Phi}{\partial t} = H\Phi, \tag{2.39}$$

[6]The spectral line is in fact not infinitely narrow, but has a certain width and a characteristic shape.

where Φ is the wavefunction and the Hamiltonian is defined as:

$$H = H^0 + H^B + H^E. \tag{2.40}$$

The unperturbed, or field-free, Hamiltonian H^0, contains the information on the electron spin, relativity and quantum electrodynamics, in addition to the terms describing the second electron in a helium atom and its interaction with the first. The form of this Hamiltonian is irrelevant, as EZSSS takes the unperturbed, field-free, energy eigenstates from the NIST atomic database [2.32]. The other two terms contributing to the total Hamiltonian are the Hamiltonians associated with the external magnetic $\vec{B}$ and electric fields $\vec{E}$:

$$H^B = -\vec{\mu} \cdot \vec{B} \tag{2.41}$$

describes the interaction between the magnetic field and the total magnetic moment of an atom, $\vec{\mu}$, and

$$H^E = -\vec{d} \cdot \vec{E} = e\vec{r} \cdot \vec{E} \tag{2.42}$$

is the interaction energy operator associated with the presence of an external electric field, where $\vec{d}$ is the electric dipole moment which appears as the atom becomes polarized by the field in a particular direction of the field.

In the cases considered in this thesis and its outlook, both the magnetic field which may be present in the vicinity of the ICRF antenna, and the electric field which is enhanced by the RF sheath rectification, induce changes to the atomic energy levels which are far greater than the relative splitting in the Fine (or Hyperfine) Structure of an atom[7]. It is therefore safe to apply perturbation theory for the theoretical treatment of the Stark effect[8].

As both fields are presumed to be static through this thesis, the dependence on the temporal coordinate in Eq. 2.39 can be omitted[9].

The field-free Hamiltonian, H^0, yields an exact solution of the Schrödinger equation in the case of a hydrogen atom. This is because the problem of relative motion of one electron (with mass m_e) and a nucleus (with mass of one proton, m_p) is translated into a motion of a single particle with a reduced mass, $\mu = \frac{m_e m_p}{m_e + m_p}$, in the Coulomb field. Nevertheless, the H^0 term for the poly-electronic atoms must take into account the Coulomb repulsion between all possible pairs

[7] Fine Structure will be a comparison in the case of a hydrogen atom and the hyperfine for the case of helium.

[8] For weak electric and magnetic fields the Stark/Zeeman splitting of energy levels is comparable to Fine (Hyperfine) splitting of the unperturbed levels. In these cases, the theoretical treatment must account for the Stark effect on the Fine (Hyperfine) levels.

[9] The EZSSS code, on the other hand, can handle temporal variations in electric fields, and distinguishes between the so-called "quasi-static" case used in this work and the "Floquet method" which calculates the Stark effect with time-dependent perturbations based on the Floquet theorem.

of electrons. As a consequence, their unperturbed Hamiltonian can not be written as a sum of contributions from each electron, and the associated Schrödinger equation can not be solved unless approximations are made.

This already applies for the atom of helium, which has two electrons orbiting a nucleus. One of its electrons remains in the ground state, in the vast majority of cases, while the other is excited (for this reason they are called the *inner* and the *optical* electron, respectively) [2.31, 2.34]. In addition, the first excited state of helium is already at a significant energy difference from the ground state. Therefore, in order to describe the electron states in the helium atom, an approximation is made that considers the optical electron as if it moves in a centrally symmetrical field created by the nucleus and the inner electron. This is a so-called *self-consistent field approximation* and it allows for the unperturbed wave functions of helium to be approximated as hydrogenic.

The repulsion of the inner electron felt by the optical one is reflected in the energies of electronic orbitals, which are not only functions of the prime quantum number n, but also depend on the orbital angular momentum quantum number l [2.31]. This is the main difference from the hydrogen atom, where the energy of the quantum state of a system is uniquely determined by n and does not depend on l and the magnetic quantum number m[10]. As a consequence of such dependences, when the perturbed Schrödinger equation is solved for an external electric field as a perturbation, the magnitude of the splitting of the levels into sub-components is proportional to the square of the electric field in the case of helium, and linear with the field strength in the case of hydrogen. Moreover, while the Stark effect on the shapes of spectral lines of hydrogen is always symmetrical, in the case of helium, certain levels (those with the total angular momentum $J = 0$ and $J = 1/2$) do not split and only undergo shifting [2.35].

EZSSS solves the starting Schrödinger equation in a coupled basis set, as these are the eigenfunctions of the unperturbed, field-free, Hamiltonian. The associated wave functions are represented in a bra-ket notation:

$$\phi = |n, L, S, J, M\rangle \,. \tag{2.43}$$

The quantum numbers are labelled corresponding to the case of poly-electron atom of helium. With this basis set, an eigenvalue problem can be constructed for the unperturbed i-th quantum state (associated with the i-th wave function), as:

$$H^0 \phi_i = E_i \phi_i, \tag{2.44}$$

where the energy eigenvalues are simply taken from the NIST atomic database, as indicated earlier, which makes the form of the unperturbed field-free Hamil-

[10] $l(l+1)$ and m are the eigenvalues of the square root of the orbital angular momentum and its z component, respectively.

tonian unnecessary for the calculations. Similarly, when the field-dependent Hamiltonians H^B and H^E act on the coupled basis set:

$$H^B\phi_i = \sum_{k=1}^{N} E^B_{ik}\phi_k, \tag{2.45}$$

and

$$H^E\phi_i = \sum_{k=1}^{N} E^E_{ik}\phi_k. \tag{2.46}$$

The energy eigenvalues, E^B_{ik} and E^E_{ik} in Eqs. 2.45 and 2.46 are the matrix elements of the associated Hamiltonians, H^B and H^E respectively. The Hamiltonian matrices have size $N \times N$, where N is the number of sub-states for a given principal quantum number, and the matrix element are found from:

$$E^B_{ik} = \langle \phi_k | H^B | \phi_i \rangle, \tag{2.47}$$

and

$$E^E_{ik} = \langle \phi_k | H^E | \phi_i \rangle, \tag{2.48}$$

where $\phi_k = |n', L', S', J', M'\rangle$ and $\phi_i = |n, L, S, J, M\rangle$ are the k-th and i-th wave functions. The detailed calculation of these matrix elements is given in detail in the Appendices of [2.36] and [2.33].

Due to the orthogonality of the coupled basis set, the eigenvalue equation for the complete Hamiltonian H defined with Eq. 2.40 becomes:

$$(H^0 + H^B + H^E)\Phi_i = E_i\Phi_i, \tag{2.49}$$

yielding N distinct eigenvalue - eigenvector pairs, i.e the energies and the wave functions E_i and Φ_i, of the perturbed quantum states of an atom exposed to strong external electric and magnetic field.

Figure 2.6 shows by how much the energy eigenvalues of the total Hamiltonian change from the field-free one, when the strength of an external electric field is increased to $5\,\mathrm{kVcm}^{-1}$. The computation was performed for the sub-states of two states of helium atom: the upper sub-figure shows the 48 sub-states associated with n=4 state of a triplet ($S = 1$) helium, and the lower sub-figure represents the energy change of 12 sub-states associated with n=2 state of a triplet helium. It clearly demonstrates as valid the guidelines suggested by W. Hicks ([2.31]) and listed in the previous section: the upper level ($n = 4$) sub-levels with higher angular momentum quantum number ($l = 2, 3$, i.e $l =$ "D","F") are more sensitive to the perturbing electric field.

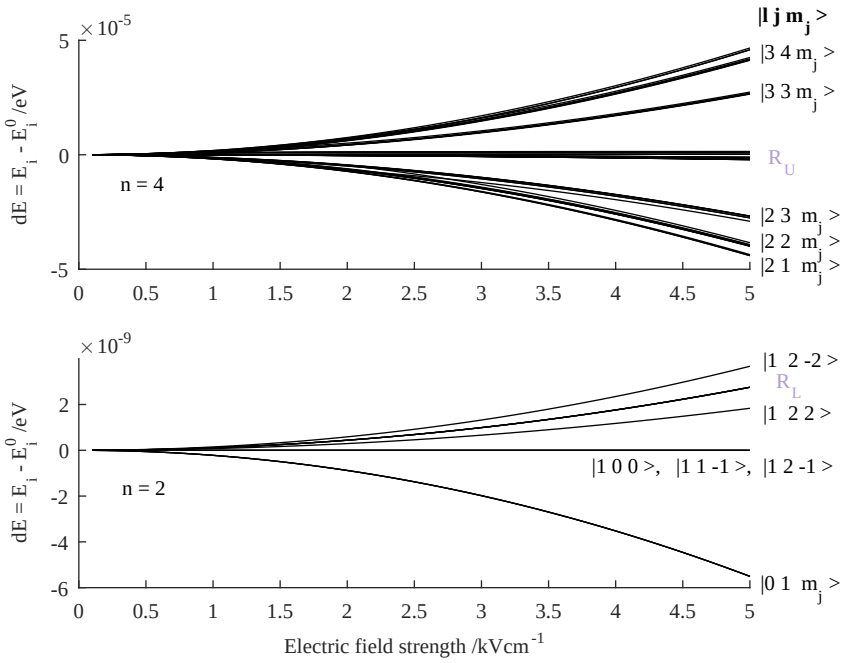

Figure 2.6: The energy difference of the total Hamiltonian from the energies associated with the field-free Hamiltonian, for the levels associated with the n=4 and n=2 of the triplet, S=1, states of helium when the external electric field strength is increased to $5\,kVcm^{-1}$. *Magnetic field was not considered for the calculation resulting in this figure, for simplicity of representation. The remaining good quantum numbers of the basis set, l j,* m_j, *are given on the righ side of the figure, tracing each state. The upper figure shows 48 sub-states assosiated with the n=4 state, and the lower figure the 12 sub-states within the n=2. The states grouped under the* R_U *and* R_L *label in the upper and lower levels respectively, are referring to the allowed combination of the quantum numbers that are spaced too close together for a distinguished label.*

Step Two: Theoretical spectral line

The next step in the theoretical treatment of the Stark effect on the spectral line profile is the estimation of the transition probabilities associated with the calculated perturbed energy levels.

In order to simulate the spontaneous emission process, which is the focus of the diagnostic described within this manuscript, EZSSS uses time-dependent perturbation theory. This way, the code deals with the behaviour of an atom perturbed by external magnetic and electric field (a system solved in the previous step) undergoing a radiative transition. The consequence of the expansion of the total Hamiltonian by a small time-dependent perturbation is that a system which was initially in state Φ_i will at the time t be found in another eigenstate Φ_f, as Φ_i is no longer the eigenstate of the total Hamiltonian. The time-dependent perturbation thus introduces the temporal evolution of the system so that it can make a transition between its various energy states.

The new Schrödinger equation is then:

$$i\hbar\frac{\partial\Theta}{\partial t} = (H + \hat{H})\Theta, \tag{2.50}$$

At $t = 0$ the wave function describing the initial state of the system is given as a linear combination of the perturbed Φ, obtained from Eq. 2.49:

$$\Theta(0) = \sum_{i=1}^{N} \Gamma_i \Phi_i, \tag{2.51}$$

where Γ_i are the complex expansion coefficients, and the sum is again over all N sub-states of a state associated with a given principle quantum number n. The assumption made in the EZSSS calculations is that the mixing of the states with different principle quantum number is negligible (which is justified for the electric field strengths below $100\,\mathrm{kV/cm}$ as is the case within the scope of this work).

If $\hat{H} = 0$, the time evolution of Θ wave function is:

$$\Theta(t) = \sum_{i=1}^{N} \Gamma_i e^{-iE_i t/\hbar} \Phi_i, \tag{2.52}$$

and the probability of finding the system in a f state at time t is the same as the probability of fining it there at $t = 0$:

$$P_f(t) = \left|\langle \Phi_f | \Theta \rangle\right|^2 = \left|\Gamma_f e^{-iE_f t/\hbar}\right|^2 = \left|\Gamma_f\right|^2 = P_f(0). \tag{2.53}$$

However, when $\hat{H} \neq 0$ the expansion coefficient Γ_f and the probability P_f are given a temporal component.

Equation 2.50 can be rewritten as:

$$\sum_{i=1}^{N}\left(i\hbar\frac{d\Gamma_i}{dt}+\Gamma_i E_i\right)e^{-iE_i t/\hbar}\Phi_i=\sum_{i=1}^{N}\Gamma_i e^{-iE_i t/\hbar}\left(E_i+\hat{H}\right)\Phi_i, \tag{2.54}$$

Assuming that the set of wave functions Φ is orthonormal, $\langle\Phi_i|\Phi_f\rangle=\delta_{if}$, the time evolution of the expansion coefficients follows from the above equation, and with that - the probability of finding the system in a new state at time t:

$$i\hbar\frac{d\Gamma_f}{dt}=\sum_{i=1}^{N}\hat{H}_{fi}e^{i\omega_{fi}t}\Gamma_i, \tag{2.55}$$

where $\hat{H}_{fi}=\langle\Phi_f|\hat{H}|\Phi_i\rangle$ and $\omega_{fi}=(E_f-E_i)/\hbar$.

Equation 2.55 represents a set of N-coupled first-order differential equations. To solve them beyond a two-level case, certain approximations must be made. The first is to assume the system was in a completely different initial state at $t=0$, and set that as a boundary condition for the iterative substitution into the right hand side of Eq. 2.55. The exact solution is approximated here by stopping the iteration after obtaining the first order expansion. With that, the probability of finding the system in an energy state f at time t, if it was initially in a completely different energy state i, is found to be:

$$P_{if}(t)=|\Gamma_f(t)|^2=\left|-\frac{i}{\hbar}\int_0^t\hat{H}_{fi}(\tau)e^{i\omega_{fi}\tau}\mathrm{d}\tau\right|^2, \tag{2.56}$$

which is valid provided that $P_{if}(t)\ll 1$.

As the perturbation[11] is supposed to simulate the emission of the electromagnetic radiation, the above can be expanded around a small harmonic perturbation. Furthermore, such perturbation should represent a linearly polarized, monochromatic, plane wave[12]. This implies the vector potential in the following form:

$$\vec{A}=A_0\vec{\epsilon}\cos\left(\vec{k}\cdot\vec{r}-\omega t\right), \tag{2.57}$$

where $\vec{k}$ is a wave vector, and $\vec{\epsilon}$ is a unit vector indicating the direction of polarization. The scalar potential in this case simply vanishes.

This leads to the Hamiltonian of the time-dependent harmonic perturbation to be approximated as (neglecting the second order terms and higher):

$$\hat{H}(t)=Fe^{i\omega t}+F^{\dagger}e^{-i\omega t}\approx-\frac{eA_0\vec{\epsilon}\cdot\vec{p}}{2m_e}\left(e^{(i\vec{k}\cdot\vec{r}-i\omega t)}+e^{(-i\vec{k}\cdot\vec{r}+i\omega t)}\right). \tag{2.58}$$

[11] Spontaneous emission in this analysis allows for an interaction between an excited atom (in the $E_i>E_f$) and a photon that would exist if the atom was not excited.

[12] The recipe for designing a Hamiltonian of a particle, with a charge $q=-e$, in a quantized electromagnetic field is to express the momentum in terms of a vector potential ($\vec{A}$): $\vec{p}\rightarrow\vec{p}-e\vec{A}$, and the total Hamiltonian in terms of a scalar potential (ϕ): $H\rightarrow H+e\phi$.

EZSSS is constrained to calculate the relative values of the emission intensities, and with that all of the constants are ignored. This reduces the problem of finding the transition probabilities described by Eq. 2.56 to calculating the matrix elements of $\langle \Phi_f | F | \Phi_i \rangle$:

$$\langle \Phi_f | F | \Phi_i \rangle \propto \langle \Phi_f | \vec{\epsilon} \cdot \vec{p} e^{i\vec{k}\cdot\vec{r}} | \Phi_i \rangle . \tag{2.59}$$

As the wavelength of an electromagnetic wave emitted during the transition between two energy levels of an atom is typically far greater than the size of an atom, $e^{i\vec{k}\cdot\vec{r}}$ can be expanded in a Maclaurin series, and thereby approximated as $e^{i\vec{k}\cdot\vec{r}} \approx 1$. This is known as an electric dipole approximation.

In the electric dipole approximation therefore:

$$\langle \Phi_f | F | \Phi_i \rangle \propto \vec{\epsilon} \cdot \langle \Phi_f | \vec{p} | \Phi_i \rangle . \tag{2.60}$$

This further becomes

$$\vec{\epsilon} \cdot \langle \Phi_f | \vec{p} | \Phi_i \rangle = -\frac{i m_e}{\hbar} \vec{\epsilon} \cdot \langle \Phi_f | [\vec{r}, H] | \Phi_i \rangle = i m_e \omega_{fi} \langle \Phi_f | \vec{r} | \Phi_i \rangle = \frac{i m_e}{e} \langle \Phi_f | \vec{d_{if}} | \Phi_i \rangle , \tag{2.61}$$

by making use of the commutator operator of the position and the Hamiltonian operators, the fact that the matrix elements of the Hamiltonian H have been calculated in the **Step One** and by defining an effective dipole moment of an atom in transition from the initial to the final state, $\vec{d_{if}}$:

$$d_{if} = \langle \Phi_f | e\vec{r} | \Phi_i \rangle . \tag{2.62}$$

Thereby, the matrix elements the code is calculating are the projections of the atomic dipole moment onto a specific direction of the polarization, which is defined with respect to the externally applied macroscopic electric field.

As the Stark effect resolves the otherwise degenerate energy levels into the sub-levels that are differentiated by the orientation of the angular momentum of the state[13], the m (also called *magnetic*) quantum number, the Stark shifts of the corresponding spectroscopic transitions show a strong dependency on the orientation of the polarization with respect to the external electric field.

[13] Specifically, the z-component of the orbital angular momentum of an atom in the Coulomb field in a state nlm (there are $2l+1$ values of m). When talking about helium atoms, an approximation is made where the electrostatic interaction between the electrons in an atom is considered to be a dominant one over the spin-orbit interaction (the LS coupling approximation). When this is the case, care must be taken about the mutual orientation of orbital angular momenta, encapsulated in the quantum number L which is the total orbital angular momentum. The new sub-levels that emerge from splitting, characterized by both L and S, the total spin, differ in how the total angular momentum J is oriented in space, measured by the quantum number M instead of m.

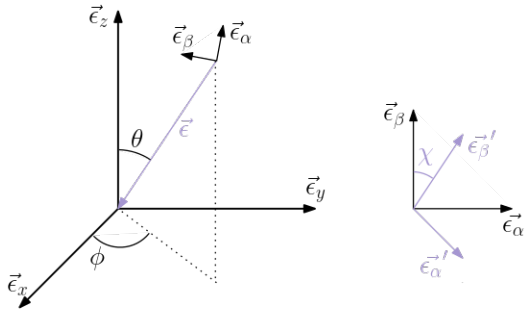

Figure 2.7: Geometry of the view line (left) and the rotation of the polarization vector coordinate system within the coordinate system defining the collection optics view plane (right). Adapted from [2.33].

It has been experimentally observed and verified by the Stark effect theory [2.20, 2.37] that the wavelength shift is more pronounced for the spectral components associated with the parallel orientation of the polarization vector to the macroscopic electric field (these are the radiative transitions with no change in magnetic quantum number: $\Delta m = 0$) than for those associated with the polarization perpendicular to the field (the transitions with $\Delta m = \pm 1$). The spectral line components with the polarization parallel to the background electric field are typically referred to as the π components, while those with the polarization perpendicular to the electric field vector are called the σ components[14].

The EZSSS code calculates the polarization vector based on its projection on the $\epsilon_\alpha - \epsilon_\beta$ plane (the collection optics view plane) in Fig. 2.7, where the unit vectors $\vec{\epsilon}_\alpha$ and $\vec{\epsilon}_\beta$ are defined with respect to the θ and ϕ angles of the view line in the experiment [2.33]:

$$\begin{aligned} \vec{\epsilon}_\alpha &= -\cos\phi\cos\theta\vec{\epsilon}_x - \sin\phi\cos\theta\vec{\epsilon}_y + \sin\theta\vec{\epsilon}_z \\ \vec{\epsilon}_\beta &= -\sin\phi\vec{\epsilon}_x + \cos\theta\vec{\epsilon}_y. \end{aligned} \tag{2.63}$$

Furthermore, as those angles are typically fixed (the position of the collection optics is usually well described and rarely undergoes any change during the experiments), the π and σ components of the spectral line profile are experimentally accessed with a polarizing optical element. This optical element is used to transmit a specific polarization state. Within the EZSSS a polariser is taken as transmitting along two orthogonal polarization axes, with specified value of corresponding transmission fractions, in a plane defined by the unit

[14] Letter π is here referring to "p" in "parallel", while the letter σ stands in stead of "s" in "senkrecht" - a German word for "perpendicular".

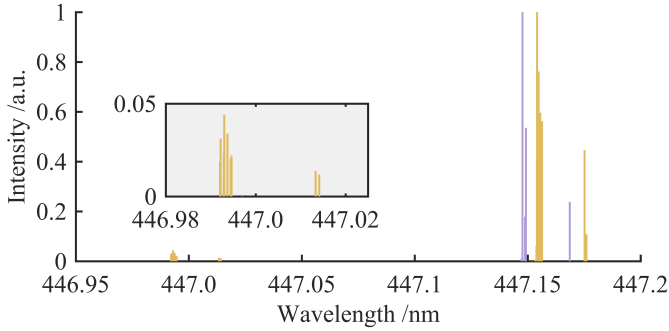

Figure 2.8: Discrete spectral lines resulting from the EZSSS calculation of the probable radiative transitions between the sub-levels of $n = 4$ and $n = 2$ levels of triplet, $S = 1$, helium. The two cases presented here are for $E = 0\ kV\ cm^{-1}$ (an unperturbed, field-free system) in purple, and in yellow are the lines originating from a transition of the atom in an $E = 5\ kV\ cm^{-1}$, with the polarization in the π direction. The magnetics field was set to $B = 0\ T$, for simplicity. The energy difference of the contributing energy levels is corresponding to the Fig. 2.6

vectors $\vec{\epsilon}'_\alpha$ and $\vec{\epsilon}'_\beta$. The polarization plane is laying on the observation plane $\epsilon_\alpha - \epsilon_\beta$, where it can be rotated by the angle χ, Fig. 2.7.

Based on the calculated matrix elements associated with the electric dipole operator, $\hat{H}$, the probability for a transition with a spontaneous emission per unit time, i.e. the transition rate for a spontaneous emission, is given by a Fermi's golden rule [2.29]:

$$w_{if} = \frac{\pi\omega_{if}^3}{\hbar\epsilon_0 c^3}\left|\vec{\epsilon}\cdot\vec{d}_{if}\right|^2, \tag{2.64}$$

where ω_{if} is the (angular) frequency of an emitted photon.

Finally, as output after the second stage of the calculations, EZSSS produces discrete spectral data: the number of non-degenerate transitions for which the modulus squared of the associated dipole moment is non-zero, associated energies (wavelengths) and their relative intensities. An example of a discrete spectra is shown in Fig. 2.8. The relative intensities, I_{if} are obtained by differentiating w_{if} per unit solid angle dΩ. The discrete theoretical spectral line is computed by summing over all N sub-states:

$$I_D(\lambda) = \sum_{i=1}^{N}\sum_{f=1}^{N} I_{if}(\lambda), \tag{2.65}$$

where the wavelength of the emitted photon is now found as $\lambda = {}^{2\pi c}/_{\omega}$.

Step Three: Continuous spectral line profile

Since the result of the second stage of the EZSSS spectra calculation is a discrete series of $\delta-$functions, it is possible to construct a continuous line profile with the convolution of discrete lines, $I_D(\lambda_0)$, with the profile of the instrument function, $I_I(\lambda)$, and the Doppler broadening associated with the motion of the emitter, $I_{DB}(\lambda)$:

$$I(\lambda) = \iint_{-\infty}^{+\infty} I_D(\lambda_0) I_{DB}(\Lambda - \lambda_0) \mathrm{d}\lambda_0 I_I(\lambda - \Lambda) \mathrm{d}\Lambda. \tag{2.66}$$

The instrument function is experimentally determined and fitted in a separate routine in the procedure that is outlined in Chapter 4. Due to the equipment used for this PhD thesis, specifically the intensifier in front of the CCD detector, the instrument function has Lorentzian wings, but can be accurately represented with a pseudo-Voigt profile, i.e as a linear combination of a Gaussian and Lorentzian.

However, EZSSS can only take into account either pure Gaussian or pure Lorentzian shapes of the instrumental function. Given that the Lorentzian contribution is more pronounced in the wings and Gaussian near the top of the line profile, while both are centred around the same wavelength (symmetric profile), the influence of the Lorentzian contribution on the full width at half the maximum of the peak (FWHM), and the position of the center of the peak, is negligible. It is therefore safe to proceed with the EZSSS convolution assuming a Gaussian profile.

In addition, since the geometry of the measurements (mutual orientation of the magnetic and electric field vectors, with respect to the view line connecting the measuring optics and the location of interest, and the orientation of the polarizing plane) is typically fixed (and known, or can be deduced) in every experiment, it is possible to use the wavelength shift of the main peak of the synthetic spectral line profile calculated with the EZSSS code for various electric field intensities.

The thermal Doppler broadening, associated with the Gaussian function as well, is based on the transition of interest and the temperature of the emitter.

Therefore the continuous spectral line profile $I_C(\lambda)$ is found by convolution of an array of discrete spectral lines $I_D(\lambda_0)$ with the summation of Gaussian functions representing instrumental broadening $I_I(\lambda)$ and Doppler broadening $I_{DB}(\lambda)$, with the broadening parameter σ in the following form:

$$\sigma = \sqrt{\frac{kT}{Mc^2}\lambda_0^2 + \sigma_I^2}, \tag{2.67}$$

where kT is the temperature of the emissive species of particles, given in the units of eV, M is their mass, and σ_I is the standard deviation of the Gaussian

representing the instrumental broadening.

Synthetic spectra of 447.1 nm line of neutral helium

To calculate the synthetic spectra emitted by helium atoms in the magnetic and electric fields present in the ICRF antenna sheath in IShTAR, specifically the effect of the fields on the 447.1 nm spectral line, EZSSS requires a set of input parameters to be specified. These parameters are namely the intensity of the static magnetic field (always aligned along the z axis), the x, y and z components of the static electric field, the polar and azimuth angles specifying the line of sight towards the collection optics, the polarization parameters and the emitter. The input provided in this section corresponds to the experimental geometry and the conditions discussed in the publication [2.17] and elaborated in Section 3.3 of this manuscript. The inputs describing the viewing geometry must be adjusted based on the particular set-up and equipment used in the experiments (an example of a differing one is outlined in Section 3.1).

The static background magnetic field in IShTAR was approximately 100 mT near the ICRF antenna for most of the experiments treated in this thesis and research contributions. The default orientation of the magnetic field vector in EZSSS is along the z axis so the coordinate system of the experimental geometry must be rotated accordingly. This implies that the electric field, as oriented parallel to the magnetic field will have only a component along the z axis.

For the calculations presented in this section the viewing geometry is set in such a way that the line of sight connecting the area of interest with the collection optics is oriented perpendicular to the electric field vector (azimuth angle is set to $\phi = 0°$). Thus, the observation plane is positioned parallel to the electric field vector, with the polarization plane rotated in either π or σ configuration (the polarizer transmits completely parallel or perpendicular to the electric field, respectively).

As far as the information on the emitter is concerned, the unperturbed eigenvalues are selected from the NIST tables [2.32] based on the atom and whether the Fine Structure is accounted for (this is the default and only option in the case of helium, where the states are considered as degenerate within the magnetic quantum number). Specifying the total spin indicates either a singlet or a triplet state of neutral helium atom. The spectral line is accessed through the associated transition by specifying the principal quantum numbers of the final and initial state of the atom.

The input parameters that would focus the calculations of the EZSSS on the selected spectral line, 447.1 nm of neutral helium, are provided in the Table 2.2.

Finally, information on the broadening parameters must be provided. In order to match the experimentally recorded spectra, the Gaussian shape due to Doppler broadening is set to be symmetric, with the standard deviation calcu-

Atom	Spin	Fine Structure	$N = [n_f, n_i]$
He	$S = 1$	*yes*	$n_f = 2, n_i = 4$

Table 2.2: Input values defining the spectral line of interest.

lated for the temperature of the radiator $T = 0.05\,\text{eV}$. An additional Gaussian is convoluted, with the $\sigma_G = 0.01\,\text{nm}$ to match the FWHM of the synthetic spectral line to the experimentally recorded line. The FWHM of the continuous line is 0.01 nm.

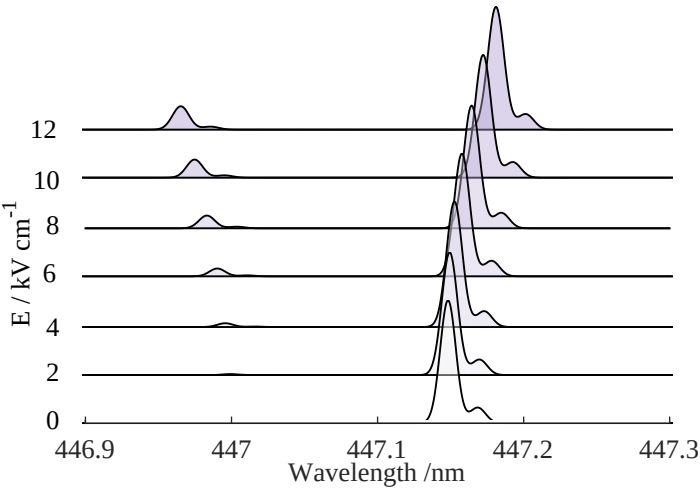

Figure 2.9: Wavelength shifts of 4^3D - 2^3P π components, calculated with the EZSSS for different electric field strength.

The final output, in the form of a continuous spectral line of a finite width, is achieved by fixing all input parameters except the electric field intensity (its $z-$component) for two critical orientations of the polarizer. Figure 2.9 shows the shift of the calculated continuous spectra focused on the line of interest as the strength of the electric field increases. The polarizer is placed in the π orientation. As the intensity of the electric field increases, the "forbidden" component of the spectra begins to appear on the left side of the dominant line due to perturbed level 4^3F and breaking of the parity selection rule ($\Delta l = \pm 1$). This spectral line corresponds to the 4^3F - 2^3P transition. However, as mentioned earlier, the relative intensity of the forbidden component with respect to the allowed one is strongly dependent on the plasma density, which is not observable in Fig. 2.9 due to the fact that the calculations are based on the perturbation theory and therefore independent from the plasma parameters.

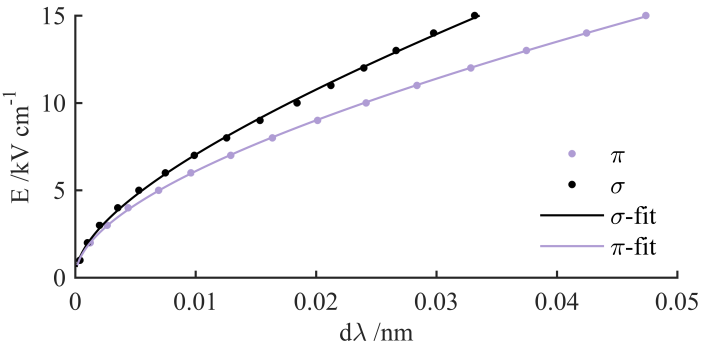

Figure 2.10: Comparison of the calculated wavelength shifts of π and σ components with increasing electric field strength, as published in [2.17].

To put this into a practical use for diagnostic purposes, the experimentally measured quantity is the position of the spectral line in the recorded spectra and the sought-out parameter is the electric field. Therefore, one must regard the inverse of the above discussion - the Stark shift, $\mathrm{d}\lambda$, of the spectral line which corresponds to the 4^3D - 2^3P transition in neutral helium atom is connected to the field intensity that caused it, $\mathrm{E} = \mathscr{F}(\mathrm{d}\lambda)$. The theoretical curve based on the EZSSS output is given in Fig. 2.10. The shift of the line from its unperturbed wavelength, is shown against the electric field strength, for two critical polarization geometries, π and σ. The other input parameters are kept fixed, at the values indicated in the previous discussion. It becomes apparent from the Fig. 2.10 that the sensitivity of the diagnostic would benefit from the π polarization. The relation describing the fit throught the points of the EZSSS output for the π polarization is the following:

$$\mathrm{E}(\mathrm{d}\lambda)\Big|_{\lambda_0} = 65.91 \times \mathrm{d}\lambda + 54.35 \times \mathrm{d}\lambda^{0.5}, \tag{2.68}$$

with E in the units of kV cm^{-1}, and $\mathrm{d}\lambda$ in nm, evaluated for $\lambda_0 = 447.147$ nm.

In this manner, the Stark effect theory is applied to experimentally recorded spectra for determining electric fields in the vicinity of ICRF antenna in the experiments discussed in the following chapter.

References

[1] Pascal Chabert and Nicholas Braithwaite. *Physics of Radio-Frequency Plasmas*. Cambridge University Press, Cambridge, 2011.

[2] Michael A. Lieberman and Allan J. Lichetnberg. *Principles of Plasma Discharges and Materials Processing*. John Wiley & Sons, Inc., 2005.

[3] Francis F Chen. *Introduction to Plasma Physics*. Springer US, Boston, MA, 1974.

[4] A. S. Richardson. *2009 NRL Plasma Formulary*. The Office of Naval Research, 2019.

[5] I. Langmuir. *Positive Ion Currents from the Positive Column of Murcury Arcs*. Science, 58(1502):290–291, oct 1923.

[6] I. Langmuir. *Oscillations in Ionized Gases*. Proceedings of the National Academy of Sciences, 14(8):627–637, aug 1928.

[7] Peter C. Stangeby. *The Plasma Boundary of Magnetic Fusion Devices*. IOP Publishing Ltd, 2000.

[8] H. S. Butler and G. S. Kino. *Plasma Sheath Formation by Radio-Frequency Fields*. Physics of Fluids, 6(9):1346, 1963.

[9] D. A. D'Ippolito and J. R. Myra. *A generalized BC for radio-frequency sheaths*. AIP Conference Proceedings, 1689:1–5, 2015.

[10] J. R. Myra and D. A. D'Ippolito. *Radio frequency sheaths in an oblique magnetic field*. Physics of Plasmas, 22(6):062507, jun 2015.

[11] Elmar Slikboer, Kishor Acharya, Ana Sobota, Enric Garcia-Caurel, and Olivier Guaitella. *Revealing Plasma-Surface Interaction at Atmospheric Pressure: Imaging of Electric Field and Temperature inside the Targeted Material*. Scientific Reports, 10(1):2712, dec 2020.

[12] Elmar Slikboer, Ana Sobota, Olivier Guaitella, and Enric Garcia-Caurel. *Electric field and temperature in a target induced by a plasma jet imaged using Mueller polarimetry*. Journal of Physics D: Applied Physics, 51(2):025204, jan 2018.

[13] Gwenael Gaborit, Jean Dahdah, Frederic Lecoche, Thibaud Treve, Pierre Jarrige, Laurane Gillette, Jerome Piquet, and Lionel Duvillaret. *Optical sensor for the vectorial analysis of the plasma induced electric field*. In 2015 IEEE International Conference on Plasma Sciences (ICOPS), volume 1, pages 1–1. IEEE, may 2015.

[14] Andreas Kainz, Harald Steiner, Johannes Schalko, Artur Jachimowicz, Franz Kohl, Michael Stifter, Roman Beigelbeck, Franz Keplinger, and Wilfried Hortschitz. *Distortion-free measurement of electric field strength with a MEMS sensor.* Nature Electronics, 1(1):68–73, jan 2018.

[15] J Michael Hollas. *Modern Spectroscopy.* John Wiley & Sons Ltd, fourth edi edition, 2004.

[16] A. Kostic, R. Dux, K. Crombé, A. Nikiforov, R. Ochoukov, I. Shesterikov, E. H. Martin, and J.-M. Noterdaeme. *Development of a spectroscopic diagnostic tool for electric field measurements in IShTAR (Ion cyclotron Sheath Test ARrangement).* Review of Scientific Instruments, 89(10):10D115, oct 2018.

[17] A. Kostic, K. Crombé, R. Dux, M. Griener, R. Ochoukov, I. Shesterikov, G. Suárez López, M. Usoltceva, R. Casagrande, E. H. Martin, and J.-M. Noterdaeme. *Polarization Stark spectroscopy for spatially resolved measurements of electric fields in the sheaths of ICRF antenna.* Review of Scientific Instruments, 90(12):123101, dec 2019.

[18] T. Gans, V. Schulz-von der Gathen, and H. F. Döbele. *Prospects of Phase Resolved Optical Emission Spectroscopy as a Powerful Diagnostic Tool for RF-Discharges.* Contributions to Plasma Physics, 44(56):523–528, sep 2004.

[19] L. Chérigier-Kovacic, P Ström, A Lejeune, and F Doveil. *Electric field induced Lyman- α emission of a hydrogen beam for electric field measurements.* Review of Scientific Instruments, 86(6):063504, jun 2015.

[20] N. Cvetanović, M. M. Martinović, B. M. Obradović, and M. M. Kuraica. *Electric field measurement in gas discharges using stark shifts of He I lines and their forbidden counterparts.* Journal of Physics D: Applied Physics, 48(20):205201, 2015.

[21] Minja Gemišić Adamov, Andreas Steiger, Klaus Grützmacher, and Joachim Seidel. *Doppler-free Stark spectroscopy of the second excited level of atomic hydrogen for measurements of electric fields.* Physical Review A, 75(1):013409, jan 2007.

[22] U. Czarnetzki, D. Luggenhölscher, and H. F. Döbele. *Sensitive Electric Field Measurement by Fluorescence-Dip Spectroscopy of Rydberg States of Atomic Hydrogen.* Physical Review Letters, 81(21):4592–4595, nov 1998.

[23] K. Takiyama, T. Katsuta, M. Watanabe, S. Li, T. Oda, T. Ogawa, and K. Mizuno. *Spectroscopic method to directly measure electric field distribution in tokamak plasma edge.* Review of Scientific Instruments, 68(1):1028–1031, jan 1997.

[24] S. Devaux, E. Faudot, J. Moritz, and S. Heuraux. *ALINE: A device dedicated to understanding radio-frequency sheaths.* Nuclear Materials and Energy, 12:908–912, aug 2017.

[25] I. Shesterikov, K Crombe, A Kostic, D A Sitnikov, M Usoltceva, R Ochoukov, S Heuraux, J. Moritz, E. Faudot, F. Fischer, H. Faugel, H. Fünfgelder, G. Siegl, and J.-M. Noterdaeme. *IShTAR: A test facility to study the interaction between RF wave and edge plasmas.* Review of Scientific Instruments, 90(8):083506, aug 2019.

[26] R. P. Brinkmann. *From electron depletion to quasi-neutrality: the sheath-bulk transition in RF modulated discharges.* Journal of Physics D: Applied Physics, 42(19):194009, oct 2009.

[27] H.G. Adler and A. Piel. *Stark-broadening of the helium lines 447 and 492 nm at low electron densities.* Journal of Quantitative Spectroscopy and Radiative Transfer, 45(1):11–31, jan 1991.

[28] M. A. Gigosos and M. Á González. *Stark broadening tables for the helium I 447.1 line.* Astronomy & Astrophysics, 503(1):293–299, aug 2009.

[29] Hans R. Griem. *Principles of Plasma Spectroscopy.* Cambridge Monographs on Plasma Physics. Cambridge University Press, 1997.

[30] A.J. Barnard and D.C. Stevenson. *Measurement of the HeI 4471 Å profile at an electron density of* $10^{15}\ cm^{-3}$. Journal of Quantitative Spectroscopy and Radiative Transfer, 15(1):123–125, jan 1975.

[31] William W Hicks, Roger A Hess, and William S Cooper. *Combined Zeeman and High-Frequency Stark Effects, with Applications to Neutral-Helium Lines Useful in Plasma Diagnostics.* Physical Review A, 5(2):490–507, feb 1972.

[32] A. Kramida, Yu. Ralchenko, J. Reader, and and NIST ASD Team. NIST Atomic Spectra Database (ver. 5.7.1), [Online]. Available: `https://physics.nist.gov/asd` [2020, February 13]. National Institute of Standards and Technology, Gaithersburg, MD., 2019.

[33] E. Martin. *Electric field measurements of the capacitively coupled magnetized RF sheath utilizing passive optical emission spectroscopy.* Doctor of philosophy, North Carolina State University, 2014.

[34] C. Deutsch, H. W. Drawin, and L. Herman. *Stark and Zeeman Effects on Neutral-Helium Lines.* Physical Review A, 3(6):1879–1890, jun 1971.

[35] Igor I. Sobelman. *The Atom in an External Electric Field.* In Atomic Spectra and Radiative Transitions, pages 173–188. Elsevier, 1979.

[36] E H Martin et al. *Electric field determination in the plasma-antenna boundary of a lower-hybrid wave launcher in Tore Supra through dynamic Stark-effect spectroscopy.* Plasma Physics and Controlled Fusion, 57(6):065011, 2015.

[37] M. M. Kuraica and N. Konjević. *Electric field measurement in the cathode fall region of a glow discharge in helium.* Applied Physics Letters, 70(12):1521–1523, mar 1997.

3
Research contribution

This chapter lays out the experimental methodology and diagnostic arrangements for two cases. One case demonstrates the implementation and the volume-integrated measurements of the sheath electric fields, while the other shows the arrangement with an added spatial coordinate. Section 3.1 addresses the optical arrangement and the spectroscopic data processing that are configured for the volume-integrated measurements of electric fields in the sheath of the DC-biased electrode placed on the main axis of the IShTAR's plasma column. This arrangement provides a proof of concept for the use of Stark spectroscopy in IShTAR. The section extends to include also the second configuration which introduces the installation of the in-vessel optics to measure the volume-integrated electric fields in the sheaths of the ICRF antenna in IShTAR. Section 3.2 describes the spatially-resolved sheath measurements with the use of polarization Stark spectroscopy, specialized multi-channel optics and local trace-gas puffing. Finally, the experimental results are discussed in Section 3.3, reflecting back at the qualitative sheath model developed in Section 2.1.

3.1 Volume-integrated electric field measurements in the sheath of the ICRF antenna

The content of this section largely follows publication A. Kostic, et al., "Development of a Spectroscopic Diagnostic Tool for Electric Field Measurements in IShTAR (Ion Cyclotron Sheath Test ARrangement)", Rev. Sci. Instrum., 89, 10D115 (2018), [3.1].

3.1.1 Experimental Method

View-locations and the optical set-up

In this section two installations within IShTAR are discussed. First, to test the feasibility of the method and re-adjust it for IShTAR's plasma and weak electric fields, a planar stainless-steel disc-shaped electrode is installed in the centre of the plasma column in the helicon source. The electrode is mounted through the gas-feed port in such a way that the main axis of IShTAR plasma source is perpendicular to the front surface of the electrode. The electrode is then biased with positive voltages up to 3.5 kV in DC regime. The schematics of this set up is given in Fig. 3.1. Light from the line of sight indicated in Fig. 3.1 is coupled to a 10 m-long optical fibre with a pure silica core of 400 µm core diameter and numerical aperture of 0.22[1], through an aspherical collimating lens with 6 mm diameter, 8.7 mm confocal length and an adjustable focal point[2]. The lens is connected directly to the fibre via an SMA-905 connector.

The second set-up was placed in IShTAR's main vacuum chamber, Fig. 3.2. Through a vacuum feed-through[3] a vacuum-compatible 2 m-long optical fibre with 400 µm core diameter and chrome-plated brass jacketing[4] was installed inside the vacuum chamber. The in-vessel optics is mounted on the holder 2 cm away from the left side of the ICRF antenna box. A collimating lens of the same kind as the one used in the "electrode set-up" was connected to the optical fibre via an SMA-905 connector and is focused onto the leading edge of the antenna box.

The optical emission spectra from these two view-points were recorded with an Andor^{TM} Shamrock750 spectrometer, of 750 mm focal length. The spectrometer is of Czerny-Turner optical arrangement and is equipped with three interchangeable 68 × 68 mm gratings with groove density of 600, 2400 and 3600 lines/mm, and a camera with a CCD sensor and an image intensifier tube[5] (a

[1] Avantes FC-UVIR-400-10-ME.
[2] Avantes COL-UV/VIS collimating lens.
[3] Avantes FC-VFT-UV400 feed-through.
[4] Avantes FC-UVIR-400-2-ME.
[5] Andor^{TM} iStar CCD 334T model.

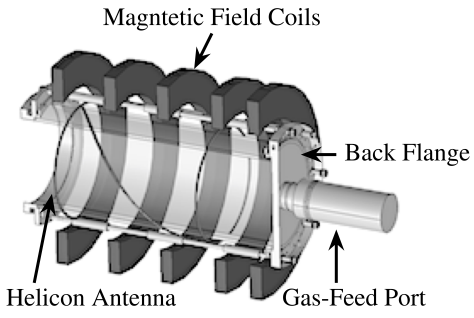

(a) IShTAR's helicon source

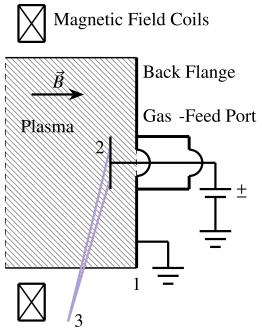

(b) Schematic view of the installed view-location

Figure 3.1: View location at the DC electrode in the helicon plasma source of IShTAR: 1 - back flange of the machine; 2 - planar electrode; 3 - optical fibre with focused collimating lens, the line of sight in indicated in purple.

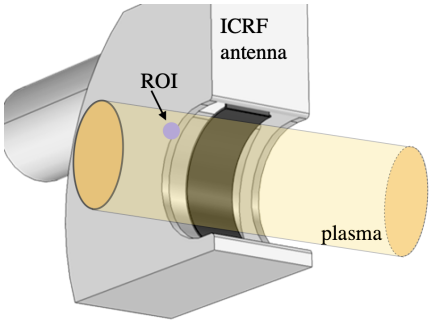

(a) IShTAR's ICRF antenna

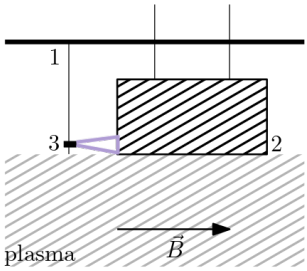

(b) Schematic view of the installed view-location

Figure 3.2: View-location on the ICRF antenna: The region where the lens is focused on is indicated in (a) in purple; on the schematic view of the set-up, (b) the schematic view of the ICRF antenna vicinity enlarged to show the fibre and the fibre holder ***(1)*** *mounted on the wall of the vacuum chamber* 2 cm *from ICRF antenna* ***(2)*** *with an indicated lens position* ***(3)*** *and line of sight represented in purple.*

Generation 2 intensifier with a micro-channel plate) with a 1024×1024 matrix of active pixels, and an effective pixel size of $13 \times 13\,\mu$m.

In order to be able to observe the changes induced by an electric field that occur on the recorded spectra, a grating with the highest groove density was used and tuned to center the desired wavelength on the horizontal axis of the CCD sensor, with a 2.33 nm bandpass. The centring of the particular wavelength is accomplished by rotating the turret on which the dispersion gratings are installed. The spectrometer has a pre-calibrated reading which relates the position of the stepper motor with the location of the spectral peak (precise position of the grating) which is accessed through the manufacturer's Andor Solis software. For finer adjustments the software also allows the corrections to be made to offset any shift between the displayed spectrum and the expected wavelength of the light emitted from the calibration spectral lamp. The analysis of calibration lamp spectra showed that the spectral resolution of this system is 0.0023 nm per pixel, with an instrumental broadening of 0.01 nm, which is elaborated in the next Chapter.

Features of 4^3D $\rightarrow$ 2^3P helium I spectral line profile With a given spectral resolution, recorded experimental spectra of He I 4^3D $\rightarrow$ 2^3P line (at 447.1 nm) in the absence of external electric field looks like the one shown in Fig. 3.3. The light-emitting source here is the helium calibration spectral lamp. What is indicated as "peak 1" and "peak 2" are in fact 6 transitions convoluted with a pseudo-Voigt profile, as an additive sum of Gaussian and Lorentzian profiles that arise predominately from the instrumental broadening and a contribution from an intensifier in front of the CCD sensor respectively.

Figure 3.4 illustrates how the synthetic spectral line associated with the He I 4^3D $\rightarrow$ 2^3P transition shifts when exposed to electric fields of up to $4\,\mathrm{kV\,cm^{-1}}$, which are the expected values in the experiments. The line profile shown in the figure is fully theoretical, as calculated by the EZSSS code following the steps outlined in the previous Chapter.

The geometry used for this calculation is shown in Fig. 3.5. In both measurement locations the electric and magnetic field vectors are parallel. The angle between the line of sight and the field vectors, θ_E and θ_A, which correspond to the line of sight at the electrode or at the antenna respectively, is defined according to Fig. 3.5, and the measured values were taken:

$$\begin{aligned} \theta_E &= 130^\circ (\pm 5^\circ); \\ \theta_A &= 180^\circ. \end{aligned} \tag{3.1}$$

Without the polarizing filter, in combination with low intensity of the electric field and with magnetic field either zero or so low it can be assumed zero[6],

[6] Magnetic field is "assumed zero" in this work when it is too low to affect the spectra.

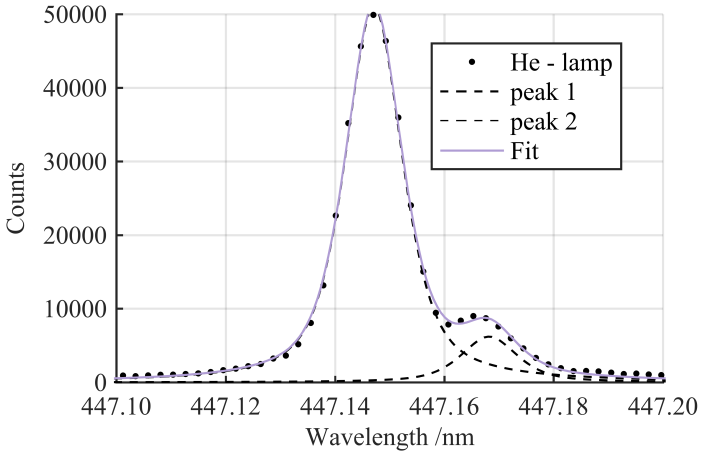

Figure 3.3: Spectral line profile of $4^3D \rightarrow 2^3P$ He I transition recorded from the He calibration lamp and fitted with pseudo-Voigt profile shows the two characteristic peaks.

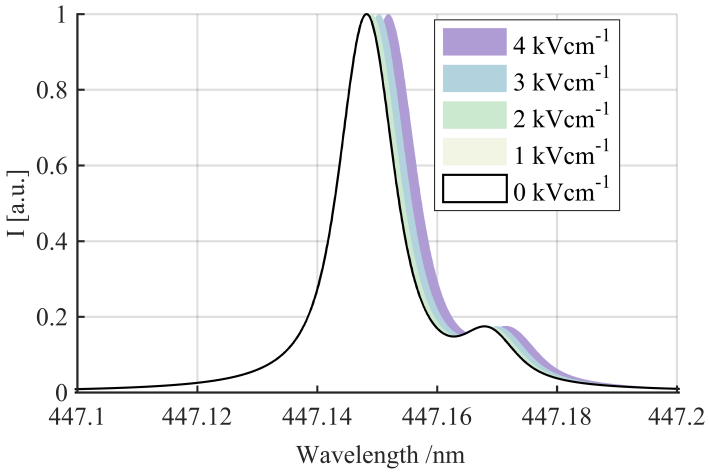

Figure 3.4: Synthetic spectra obtained with the EZSSS code shows the characteristic two-peak feature of the spectral line associated with He I $4^3D \rightarrow 2^3P$ transition and the Stark shift with increasing external electric fields used in the calculations.

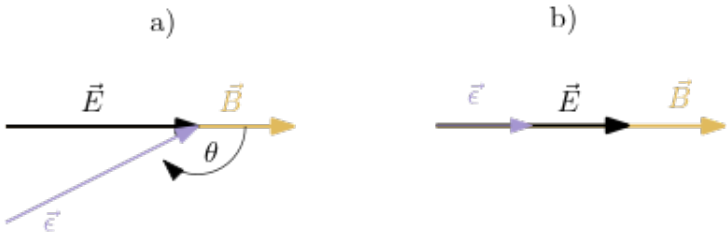

Figure 3.5: Vector geometry of the two experimental schemes used as an input for the EZSSS calculations. The experimental geometry considers the orientation of the electric and magnetic field vectors and the angle between the magnetic field vector and the line of sight of the light-collecting optics.

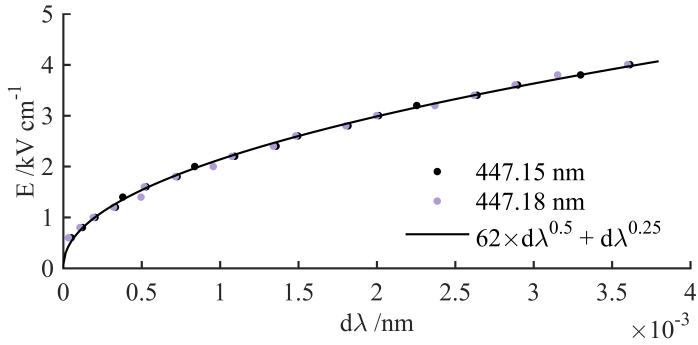

Figure 3.6: External electric field intensity as a function of Stark shifts of the two peaks characteristic for the spectral line profile of He I $4^3D \rightarrow 2^3P$ transition with respect to the unperturbed wavelength, for the geometry described in this section.

this difference in angle θ is negligible and produces virtually indistinguishable synthetic spectra.

When the EZSSS calculation is repeated with a smaller step, the shift of the spectral line with respect to its unperturbed wavelength shows a quadratic increase with increasing electric field strength. In Fig. 3.6 the electric field intensity is mapped as a function of the shift dλ of the synthetic line profile to obtain the fit function that is used to calculate the electric field from the measured shifts of lines recorded during the experiments. Fitting the mean of dλ for both components of the line profile, the following dependency is obtained:

$$E(\mathrm{d}\lambda)[\mathrm{kV\,cm^{-1}}] = 61.95 \times \mathrm{d}\lambda^{0.5}[\mathrm{nm}] + 1.013 \times \mathrm{d}\lambda^{0.25}[\mathrm{nm}] \tag{3.2}$$

where E is the electric field strength, and dλ - the shift of the line with respect to its unperturbed wavelength., $\lambda_0 = 447.147\,\mathrm{nm}$.

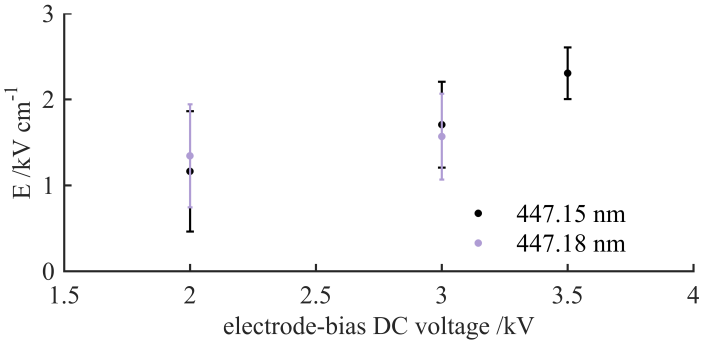

Figure 3.7: Electric field calculated based on Eq. 3.2 for the Stark shifts of the spectral lines measured in the sheath of the DC biased electrode, for different voltages applied to the electrode.

3.1.2 Results

The results presented in this section were acquired using time-averaged and volume-integrated optical emission spectra recorded passively along the line of sight from the two previously described view-locations. It has to be noted that the effect of the electric field is local, from the sheath region in front of the electrode or the ICRF antenna.

Electrode

For the experiments during which the emission was recorded from the electrode region (Fig. 3.1) plasma was created with the ICRF antenna and the discharge was sustained with the voltage applied on the electrode mounted in IShTAR's helicon source. The helicon antenna was not in operation. The magnetic field was also not imposed, as it was observed that its presence significantly lowered the optical signal. This effect is likely the manifestation of the Alfvén's theorem and the pinching effect as its consequence - increasing magnetic field through the Helmholtz coils reduces the visible area of the plasma, since in the plasma the field lines are frozen in place while the magnetic flux is conserved and the recoded light emission is line-integrated.

The emission was collected during the entire duration of the discharge with an exposure time of 1 s per scan, in a kinetic series of 15 scans per discharge. To compare and time-average the recorded data, the scans corresponding to the stable plasma phase were selected and isolated, which was during a reproducible interval of 9 s, yielding 10 scans per discharge.Once the reproducibility of the line was confirmed, the optical signal was averaged over 5 discharges per scenario. In each scenario the same base pressure and flow rate of helium gas

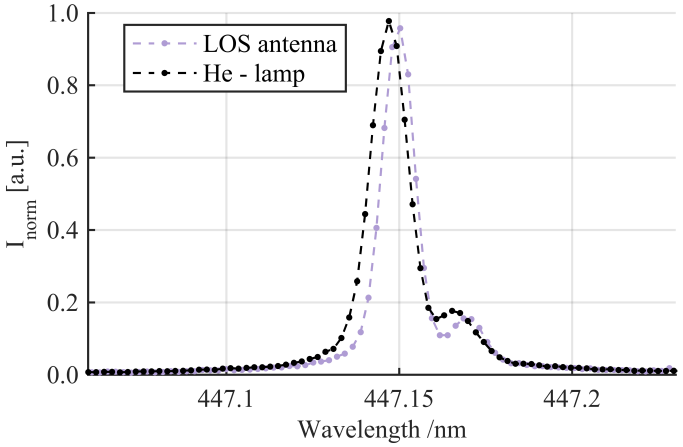

Figure 3.8: Ensemble-averaged spectra for 7 scans in 19 discharges at the ICRF antenna view-location, normalized for comparison with the He calibration lamp spectra to show the shift from the unperturbed spectra

were maintained, at p = 0.1 Pa and fr = 60 sccm respectively, while the voltage applied to the electrode was varied.

Fitting each time-averaged spectrum with a pseudo-Voigt profile provided the position of the two peaks (Chapter 4). Since these discharges were maintained with voltage applied on the electrode, for the unperturbed spectra the emission source was a helium spectral lamp used to calibrate the wavelength axes and centre the selected line on the detector matrix. Once those two were subtracted, the obtained dλ was inserted back in Eq. (3.2). Electric fields calculated this way, for each of the scenarios, is presented in Fig. 3.7. The error-bars in the given calculations were estimated using error propagation and analysis detailed in Chapter 4.

ICRF antenna

When the data was recorded at the ICRF antenna view-location, the plasma was created and maintained in the same manner as in the previously described set-up, except here the magnetic field was created with the secondary set of coils (the "Small Coils"). The maximal achievable power, in this plasma configuration, of 1 kW was delivered to the ICRF antenna that was operated at 5.94 MHz frequency. The base gas pressure was kept constant at p = 0.1 Pa.

The exposure time of the optical set-up was 1.5 s, and the data were recorded in kinetic series at an acquisition frequency of 0.66 Hz. Seven spectra, corresponding to a stable plasma, were isolated per discharge (Fig.3.8). At this view-

location 19 discharges were recorded. The post-processing of the data was the same as described in the subsection above.

The electric field strength obtained from the spectral analysis of the data recorded at the leading edge of ICRF antenna powered at 1 kW was $E = 3.4 \pm 0.3\,\mathrm{kV\,cm^{-1}}$.

3.2 Spatially resolved electric field measurements in the sheath of the ICRF antenna

The content of this section largely follows publication A. Kostic, et al., "Polarization Stark spectroscopy for spatially resolved measurements of electric fields in the sheaths of ICRF antenna", Rev. Sci. Instrum., 90, 123101 (2019), [3.2].

3.2.1 Experimental set up

Spectroscopic equipment and integration

Figure 3.9 shows a scheme of the spectroscopic equipment and its implementation in IShTAR, with the device's horizontal (axial) and vertical (radial) cross-section at the diagnostic location. Beside the device's cross-sections, the rest of the figure is divided in Section A: enclosing the "to the experiment" part of the diagnostic scheme, Section B: encircling what is called "the spectrometer part" and Section C where the cross-sections of the two ends of a custom-made bundle with 7 Ø400 µm-fibres are sketched.

A glass port, located next to the ICRF antenna box (Fig. 3.9), provides good view-lines for the electric field measurements across the sheath of the antenna box, parallel to the magnetic field lines. An optical head, with a focusing objective plano-convex Ø2", f =75 mm lens, images the area of interest (1.2 mm × 8.4 mm) onto the front face of the linear fibre bundle (1.55 mm line length). The optical head's custom-made design, depicted in Fig. 3.10 provides sufficient space to install additional optical components when necessary. An example is a linear polarizer mounted inside of the 60 mm cage rotation mount which allows for the selection of the polarization plane (σ or π, Section 2.3). The fibre bundle contains 7 silica/fluorine-doped silica step-index fibres, arranged at both ends in a linear configuration (commercially available from Thorlabs, as BFA200HS02). Each fibre within this bundle has a 0.22 numerical aperture and Ø200 µm core diameter. The location of the lines of sight, optical head design and the image projection from the 7 Ø200 µm fibres focused at the location of measurements are singled out in *Section A* of Fig. 3.9.

An Andor Shamrock 750 spectrometer is used to resolve the fine Stark shifts of the 447.147 nm line in electric fields of up to 15 kV/cm. This spectrometer, in the Czerny-Turner optical design with a focal length of 750 mm. It is equipped with three 68 × 68 mm gratings of 600, 1200 and 3600 lines/mm. For the purpose of this diagnostic, to obtain the highest spectral resolution this arrangement can provide, the grating with the highest number of lines per mm, labeled as the Grating 3 in *Section B* of the Fig. 3.9 is used. The slit size is set to 15 µm, the optimal balance achieved between the signal intensity and the sharpness of the image (the Full Width at the Half of the Maximum of the spectral line). The

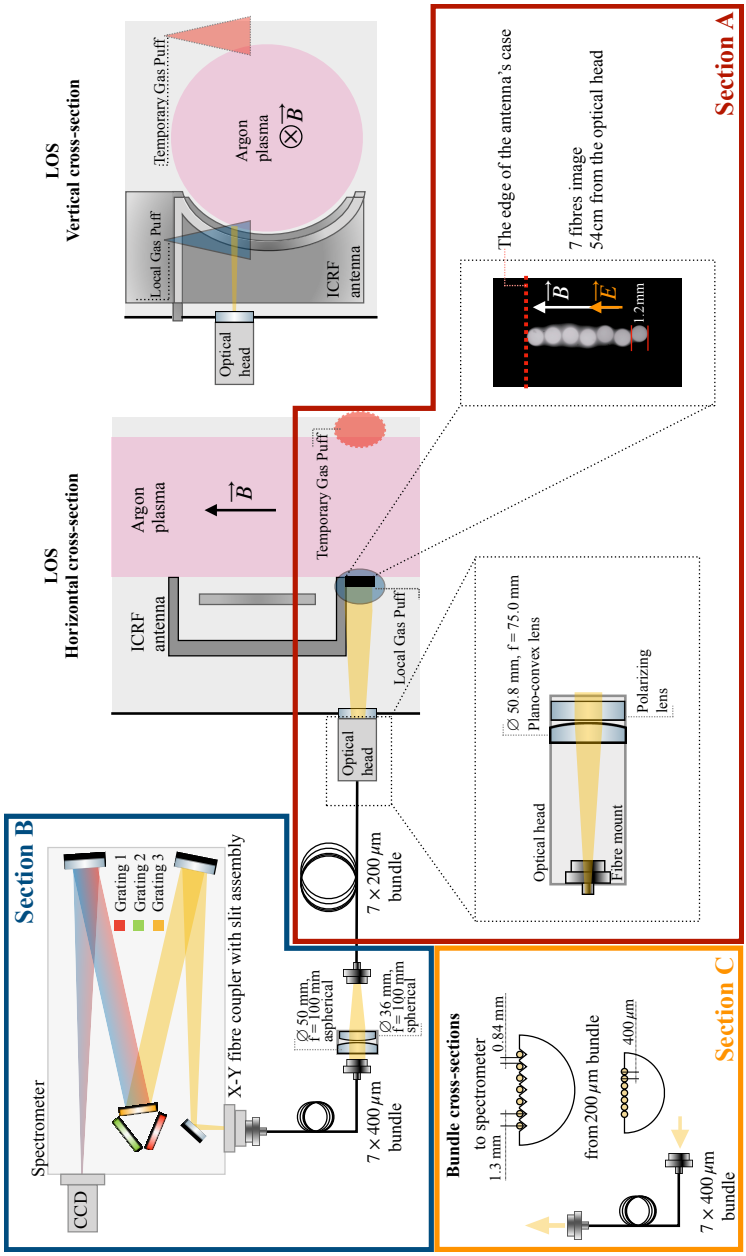

Figure 3.9: Schematics of spectroscopic system and implementation in the vicinity of IShTAR's ICRF antenna. The view lines are indicated in both the horizontal and vertical cross-section of the machine. Section A indicates the"to the experiment" part of the diagnostic scheme, Section B encircles"the spectrometer part" and in Section C the cross-sections of the two ends of a custom-made fibre bundle are given.

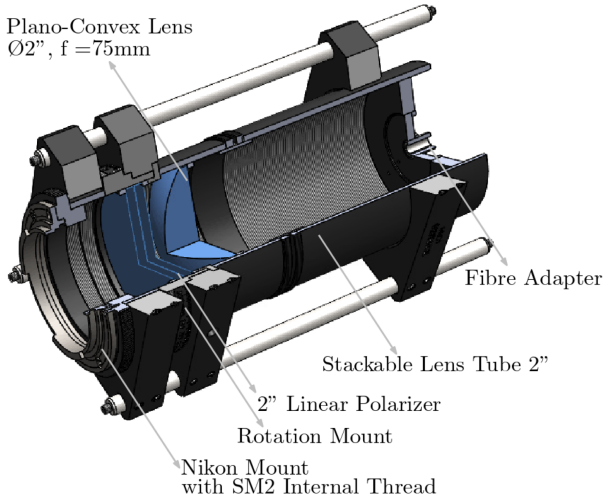

Figure 3.10: The components of the custom-made optical head.

instrumental function of the optical arrangement is 0.01 nm, or about 6 pixels.

Even though this optical arrangement of the Andor's 750 Shamrock spectrometer is providing very high spectral resolution, it introduces elongations of the signal in the vertical-pixel axis at the detector. Due to this elongation the individual images of the fibres within the bundle start to overlap on the detector's plane. To avoid the overlap of the optical signal, an additional optical set-up was installed between the free-end of the 1.55 mm fibre bundle and the entrance slit of the spectrometer, as depicted in *Section B* of Fig. 3.9. These additional optical components first double the fibre image from 200 µm to 400 µm, with a 36 mm spherical and a 50 mm quartz aspherical lens, both with a focal length of 100 mm. The enlarged image is then projected on the secondary, custom-made fibre bundle that consist of 7 Ø400 µm fibres also arranged in a linear-to-linear configuration but with an added spatial separation between the fibres on the end connected to the ferrule in front of the entrance slit of the spectrometer, as shown in *Section C* on the Fig. 3.9.

The optical signal is finally registered with the Andor's iStar 334 CCD detector with an 1024 × 1024 pixel array installed at the spectrometer's output port. The image that the detector "sees" when the grating is in the 0th order is shown in Fig. 3.11 (a), with the slit being completely open. Because the optical signals from individual fibres do not overlap, they can be binned within the corresponding vertical pixels of each fibre. When the grating is centred on 447.147 nm in first order, the optical signal that the CCD detector of the spectrometer sees, with the slit width set to 15 µm, is shown in Fig. 3.11 (b). The light source used

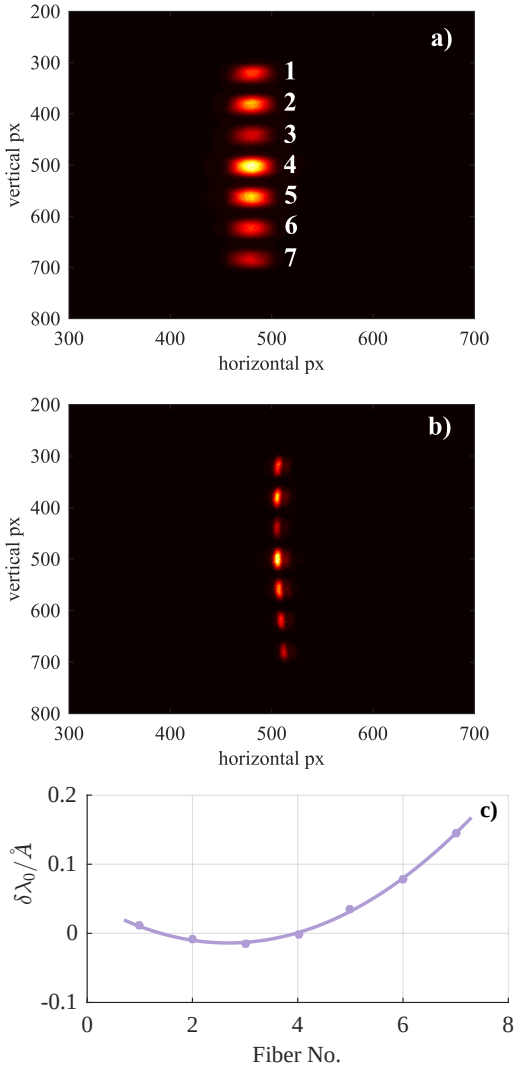

Figure 3.11: The image of the fibre bundle on the detector plane with the helium calibration lamp as the light source, (a) with the grating at the 0th order and the slit fully open, and (b) grating at the 1st order, fibre 4 centred on the 447.147 nm *line, slit width* 15 µm. *(c) Inherited parabolic displacement of the calibration signal on the detector. The equation describing the parabola is* $f(x) = 0.0085x^2 - 0.04557x + 0.04716$.

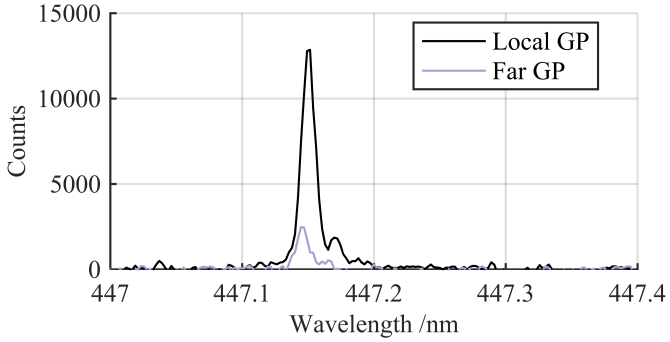

Figure 3.12: Comparing the raw spectra recorded with a local gas puff (black) and with a gas puff on the opposite side of the plasma column with respect to the location of interest (purple).

for the two images on this figure is a helium calibration lamp. It is important to stress here the typical parabolic shape with respect to the wavelength axis of the optical signal when the grating is in first order and when the full 2D plane of the detector is used, as it must be taken into account when evaluating the shifts due to the electric field.

The parabolic shape of the optical aberration with respect to the wavelength axis of the calibration lamp image is isolated in Fig. 3.11 (c), where each point represents a binned signal corresponding to a track associated with a particular fibre and its relative shift from the centred 447.147 nm, i.e fibre number 4. The shifts here are given in Å, and marked as $\delta\lambda_0$ to differentiate them from the Stark shifts. The effect does not change the resolution of the system, as is discussed in greater detail in Chapter 4.

Local helium gas puff For the purpose of this diagnostic, a localized helium gas puff is installed to decouple the optical signal originating in the sheath region near the ICRF antenna box from the bulk plasma contribution and ensure local measurements, while the main IShTAR plasma is created with argon.

After testing different percentages of the two gasses, the lowest helium gas flow rate (to avoid disturbing local plasma density and overall plasma performance) providing a decent optical signal for the 447.147 nm line, is set to 60 sccm, or 2.7×10^{19} helium atoms per second, with 10 sccm argon at base pressure $p = 0.25$ Pa. Helium is delivered through a gas tube installed above the area of interest.

Unlike in a tokamak environment where the neutral gas becomes ionized once it passes into the bulk plasma, neutral helium atoms in IShTAR remain in the device's main vacuum chamber, moving freely since they are not influenced

by the magnetic field. Therefore, in order to validate that the strongest optical signal will actually originate from the region of interest, a gas tube was put temporarily on the side opposing the antenna, with the primary argon plasma in between, as sketched in Fig. 3.9. For the same acquisition parameters and the plasma environment, the two spectra recorded with the regular location of the gas puff (Local GP, black line) and the displaced tube (Far GP, purple line) are compared in Fig. 3.12. Here it can be seen that even the contribution of a continuously puffed helium cloud behind the plasma, which could be the worst-case scenario, does not significantly affect the local measurements.

Figure 3.12 also conveniently demonstrates that the Stark shifts of the spectral lines of helium can occur only when the atoms are exposed to a strong background electric field, which is present only in the region of interest along the entire stretch of the lines of sight.

3.2.2 Data treatment and demonstrative results

To demonstrate the capabilities of the diagnostic, it was used to resolve the electrical fields across the sheath that forms around the ICRF antenna box in IShTAR. From the discharges that used this diagnostic, the focus is here on the two for which the time-traces of the operational parameters are shown in Fig. 3.13 (a). The only distinction between the compared discharges, as far as the operational parameters are concerned, was that the power was supplied to the ICRF antenna in one, but not in the other (referred to as *ICRF ON* and *ICRF OFF* discharges respectively). The left ordinate axis in Fig. 3.13 (a) represents the current through the two sets of coils, while the right ordinate axis corresponds to the RF power levels delivered to the helicon antenna. The grey-shaded area marks the stable-plasma phase. During the stable phase, the magnetic field created along the main axis of the machine was 93 mT at the area of interest, which is too low for the Zeeman effect (the magnetic-field analogue of the Stark effect) to be noticed on the recorded optical emission spectra.

When used, the ICRF antenna operated at 5.9 MHz and was matched in vacuum by a variable capacitor and inductor, which are tuned prior to a plasma discharge. The unmatched side of the transmission line is diagnosed by a voltage probe at about ~ 5 m from the antenna feedthrough and the coupled power to it by a directional coupler behind the matching components. These measurements combined provide a qualitative estimate of the voltage standing wave ratio in the line, and the time traces can be seen in Fig. 3.13(b) and (c). Three phases are clearly distinguishable: vacuum operation with 0.4 kW of coupled power and a voltage of 1.5 kV and plasma operation with 0.31 kW of coupled power in: low-power helicon at a voltage of 800 V and high-power helicon at 700 V. Two features are apparent from the measurements: a clear reduction of the voltage absolute value at the probe location when going from vacuum to

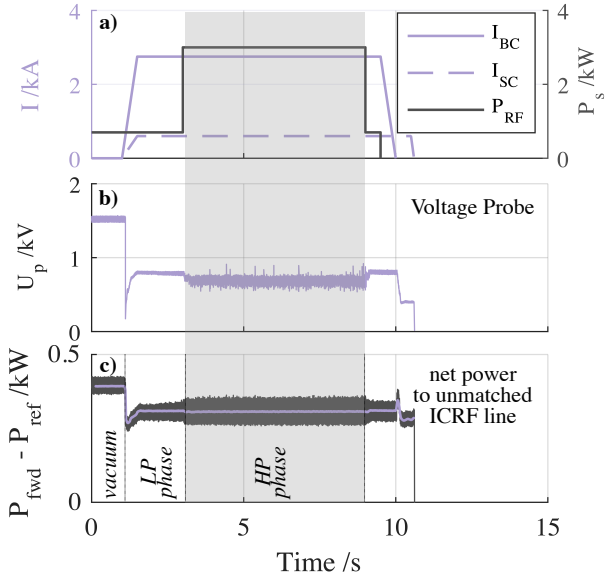

Figure 3.13: Time traces of the operational parameters. (a) I_{SC} and I_{BC} are referring to the current in the Small and the Big coils respectively. P_{RF} stands for the power delivered to the helicon antenna of the plasma source. The grey-shaded area marks the stable-plasma phase, with the overlapping flattops of the operational parameters, from $3-9$ *s of the discharge. (b) Voltage probe data characterising the ICRF ON discharge. (c) Net power to the unmatched transmission ICRF line. The reduced net power as delivered from the generator is likely due to the altered matching conditions in the presence of plasma in front of the antenna.*

helicon plasma operation (although the coupled power is also reduced), and the manifestation of turbulent structures when the ICRF antenna is operated in high-power helicon mode. Future upgrades of the ICRF transmission line diagnostics may allow for the complete measurement of the antenna loading impedance, but these are not implemented at the moment.

During the experiments, the spectra were recorded in a kinetic series of $11 \times 1\,\mathrm{s}$ of exposure time. The readout mode was set for a Multi-Track defined in such a manner that each track bins the vertical pixels associated with one fibre. Although the kinetic series cover the entire discharge duration, the analysis and the results are obtained only from the spectra recorded during the stable-plasma phase.

In post-processing, the data from the experiments and the calibration lamp is first cleaned by subtracting the corresponding dark spectra. All recorded signals are then normalised to unit area to allow a visual comparison of the spectra[7]. Normalised spectra from the calibration lamp, the discharge without and the discharge with an ICRF power are presented in Fig. 3.14. The dots are representing recorded data, while the full lines are the fitting routine's final output. The figure shows only 6 out of 7 fibres since the signal on the seventh fibre for the discharges with an ICRF antenna being ON is too noisy to fit the peak properly. Since this diagnostic method relies on the Stark shift of the line from its unperturbed wavelength to determine the strength of the electric field that caused it, for this analysis the unperturbed line is the one from the calibration lamp of helium. In Fig. 3.14, the Stark shifts are already visible, being more pronounced on the spectra recorded when the ICRF antenna was used during the discharges as compared to those when it was not. Fibres ordered from the one closest to the ICRF antenna box (**FB1**) to the one farthest, 6.6 mm, away (**FB6**) are labeled as **FB1-6** in the Fig. 3.14.

The central wavelength of the main peak in each spectrum is extracted from a pseudo-Voigt fit on the spectral line. The fitting routine, which is described in detail in Section 4.2, is performed for $N = 100$ trial runs and the best fit is saved, i.e. the one with the lowest fitting error. Since this fit is solely mathematical, a statistical weighting has been performed to maximise the precision[8], and the same procedure has been repeated to compare 50 best fits for each line fit. The most frequently occurring central wavelength is then chosen for the Stark shift estimates, with an accuracy of the fit of 10^{-6} nm.

The measured Stark shifts are finally introduced in Eq. 2.68. The electric fields evaluated as the final result of this diagnostic equipment are presented in Fig 3.15. The fields are resolved across the sheath and the horizontal axis, being the distance from the ICRF antenna case, is calibrated with respect to the centre

[7] The data post-processing is further elaborated in the next Chapter.
[8] The complete rationale behind this method is described in Chapter 4.

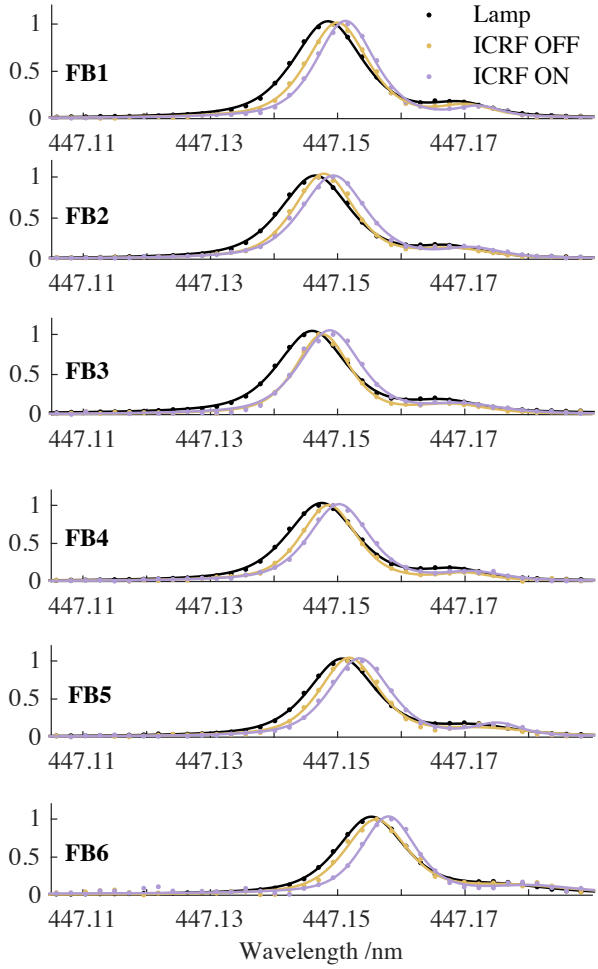

Figure 3.14: Normalized spectra from the helium calibration lamp (black), a discharge without (red) and a discharge with an ICRF antenna (blue) for the 6 fibres in a bundle from the one closest to the ICRF antenna box (FB1) to the one 8.4 mm *away from it.*

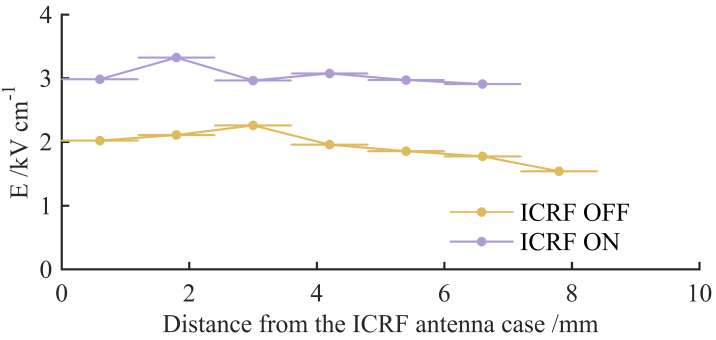

Figure 3.15: Electric field measured across the sheath of the antenna's box for the discharge without and with the ICRF antenna.

of the image of each fibre at the location of measurements with the horizontal error bars corresponding to their diameter.

The results for the discharge with the ICRF antenna being OFF are in yellow. Here the anticipated decrease of the electric field over the 8.4 mm broad region from the antenna's case is clearly visible. It must be noted that the initial estimates of the area to be scanned were based on the Langmuir probe measurements of radial electron density for different discharge configurations, which were of the order of $10^{15} - 10^{17}\,\mathrm{m}^{-3}$. However, the location of the electric field measurements is in the shadow created by the ICRF antenna casing, but also in the close proximity of a machine's metallic back flange, where the electron densities are greatly reduced. Consequently, the yellow curve in Fig. 3.15 would eventually have fallen to $0\,\mathrm{kV\,cm}^{-1}$, and this does not occur in the region covered by the lines of sight as the sheath is much wider than expected. In addition, when analysing this figure, it should be taken into consideration that even in the *ICRF OFF* scenario, the RF fields are still present in IShTAR's plasma due to the helicon source which is magnetically connected to the metallic surfaces in the main chamber where the measurements were carried out. This further complicates the simplistic (steady-state-like) calculation of sheath thickness and the estimate of electrical fields within it.

The results in purple are the electric fields across the sheath for the discharge which used the ICRF antenna. As anticipated, these fields are higher than in the previous scenario. The flattened behaviour of the evaluated data, but also the undeniable influence of the surrounding plasma environment on the electric field in the sheath is to be the subject of a study with the additional diagnostic tools in place, such as Langmuir probes close to the area of interest, aided with the appropriate theoretical models of RF sheath.

3.3 The summary of findings

The results presented in this chapter demonstrate how the Stark effect on the spectral lines of excited helium can be used to measure electric fields in the plasma sheaths, even for ekectric field strengths much weaker than 10 kV cm^{-1} in low pressure and low density plasmas.

First, experimental data was collected from two view-locations in IShTAR, where one was installed on the DC-biased electrode in the helicon plasma source, while the other was placed on the side of the ICRF antenna box in the main vacuum chamber. It is observed that the relative shifts of the 2 components of the spectral line profile, and thereby the electric field, increases with increasing voltage delivered to the DC-biased electrode. With the maximum power delivered to the ICRF antenna, which was of the order of 1 kW, the relative shift of the spectral line profile was larger in the sheaths of the ICRF antenna box than that observed in the sheaths of the DC-biased electrode. The corresponding electric field was found to be E $= 3.4 \pm 0.3$ kV cm^{-1}. This can be taken as a an indication of the ICRF power exciting the sheath.

Section 3.2 presents a diagnostic scheme based on polarization Stark spectroscopy to spatially resolve the electric field across the sheath of an ICRF antenna in magnetically confined plasmas. The diagnostic equipment described in this section comprises of a high resolution spectrometer in the Czerny-Turner optical arrangement and a pair of fibre-bundles resolving 8.4 mm in 7 points. The measurements are aided by a local helium gas puff. The diagnostic capabilities in non-helium plasmas are demonstrated by results obtained for argon plasma discharges whose operation parameters differ only in whether or not ICRF was used. As such, the presented diagnostic has a promising ability to assist the experimental research of the RF sheaths introduced by the ICRF antennas in tokamaks.

To gauge these findings, they can be compared with the predictions of the simple homogeneous DC sheath model developed in Section 2.3. According to that model, the electric field in the sheath of a DC-biased electrode can be estimated as

$$E = \frac{V_0 - V_p}{s}, \tag{3.3}$$

where V_0 is the applied DC voltage, s is the sheath boundary, defined with the Eq. 2.28, and the plasma potential is assumed to be $V_p \approx 0$. The results of Eq. 3.3 for three values of the electron density in the bulk plasma, n_0, are given in Fig. 3.16. Since the exact plasma density in front of the electrode could not be measured during the experiments, as discussed in Section 3.1, the values typical of the glow discharge plasmas were used to calculate the electric field in the sheath and compare those results with the data the diagnostic recorded

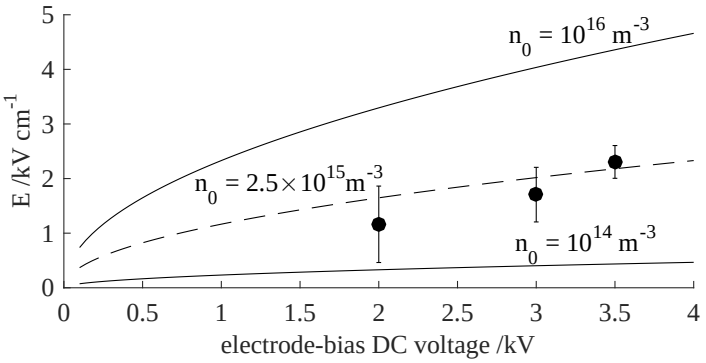

Figure 3.16: Electric field in the DC sheath, based on a crude model described in Section 2.3 for a range of values of the DC voltage at the planar electrode, for three different values of plasma density in the bulk and the comparison with the measured electric fields (dots, as in Fig. 3.7).

during the experiments. From the results of the simple analytical calculation, it can be seen that the electric field rises with the increasing voltage provided to the electrode. The experimental data measured with the developed electric field diagnostic is within the expected range.

Looking back at Fig. 2.5, for the range of typical values for currents and plasma density in both cases when the ICRF antenna was used in IShTAR, the sheath-integrated and spatially-resolved electric field measurements fall within the expected range of values. The measured spatial distribution of electric field strengths shows the predicted behaviour of decreasing with increasing distance from the antenna box. The vectorial direction of the DC electric field is deduced independently from the vector orientation when setting the geometry in the EZSSS code.

The case that can not be explained with the simple sheath model outlined in Chapter 2 concerns the high electric fields measured in the sheath of the ICRF antenna box when the antenna is not in operation. If the area of interest is assumed to be a fully isolated system as set out in the model, this scenario corresponds to the simple no-bias, no-RF-modulated floating potential case. However, as has been pointed out in earlier discussions, the high electric field strengths measured through the sheath of the passive ICRF antenna may be due to the presence of the helicon wave throughout IShTAR.

References

[1] A. Kostic, R. Dux, K. Crombé, A. Nikiforov, R. Ochoukov, I. Shesterikov, E. H. Martin, and J.-M. Noterdaeme. *Development of a spectroscopic diagnostic tool for electric field measurements in IShTAR (Ion cyclotron Sheath Test ARrangement).* Review of Scientific Instruments, 89(10):10D115, oct 2018.

[2] A. Kostic, K. Crombé, R. Dux, M. Griener, R. Ochoukov, I. Shesterikov, G. Suárez López, M. Usoltceva, R. Casagrande, E. H. Martin, and J.-M. Noterdaeme. *Polarization Stark spectroscopy for spatially resolved measurements of electric fields in the sheaths of ICRF antenna.* Review of Scientific Instruments, 90(12):123101, dec 2019.

4

Improving Accuracy, Precision and Resolution

The steps taken to enhance the accuracy, precision and resolution of the diagnostic are discussed in this chapter. These steps include the optimization of the hardware components and the use of an optimized solver to fit the experimental spectra in order to provide greater accuracy for reading the sub-pixel data. Such measures are required to access the electric fields that are less than $5\,\mathrm{kV\,cm^{-1}}$ in the vicinity of an ICRF antenna, using the diagnostic equipment and method discussed in this manuscript. In addition, a full analysis of the measurement uncertainties is addressed in the final section of the chapter.

4.1 Optimisation of the spectroscopic hardware and the wavelength axis

The equipment used to detect and quantify the Stark effect on helium atoms in the vicinity of an ICRF antenna follows the standard set-up used for optical emission spectroscopy [4.1], depicted in Fig. 4.1. The light from the Source is coupled to the fibre optic channels by an additional signal-collection optics. It is then transferred to the Disperser, which spatially spreads the constituent wavelengths over the Detector's plane.

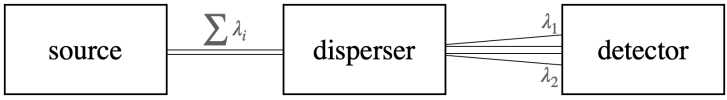

Figure 4.1: The basic constituents for the optical emission spectroscopy. Adapted from [4.1].

The Source, in this work, is the region of interest in the sheath (or plasma) near the surface of the antenna box, as in Section 3.2 or the DC-biased electrode, Section 3.1, where helium atoms subjected to the external electric fields are excited. The Source for what is referred to as the "unperturbed" wavelength is the helium calibration lamp. Fibre optics and signal collection optics were discussed earlier in the manuscript, in the relevant sections on diagnostic implementation. Here, more detail is given regarding the other elements of the diagnostic system, as they set the limit on the electric field strength that can be measured.

The Detector and the Disperser are installed as a part of the optical layout of the Andor's Shamrock 750 spectrometer. This is a Czerny-Turner optical layout with three mirrors, as shown in Fig. 4.2. The flipper mirror directs the light ray from the side entrance slit to the collimating mirror. The ray then falls on one of the three diffraction gratings, each 68 × 68 mm in size, mounted on the turret located on the axis of the instrument, S. The spectral range is changed with the rotation of the turret. The diffracted ray is reflected from the focusing mirror on the detector plane. The focal length of this spectrometer, $F = 750$ mm (measured [1] $F = 737.94$ mm) is the length between the focusing mirror and the detector plane.

The Detector is an areal CCD sensor with a matrix of 1024 × 1024 pixels, each 13 μm in width and height, making an effective active area of 13.3 × 13.3 mm. The CCD element is a part of the Andor's iSTAR 334T camera (which includes the detector's integrated drive and a readout electronics), mounted in the exit focal plane of the spectrometer.

[1] details in Sec. 4.3

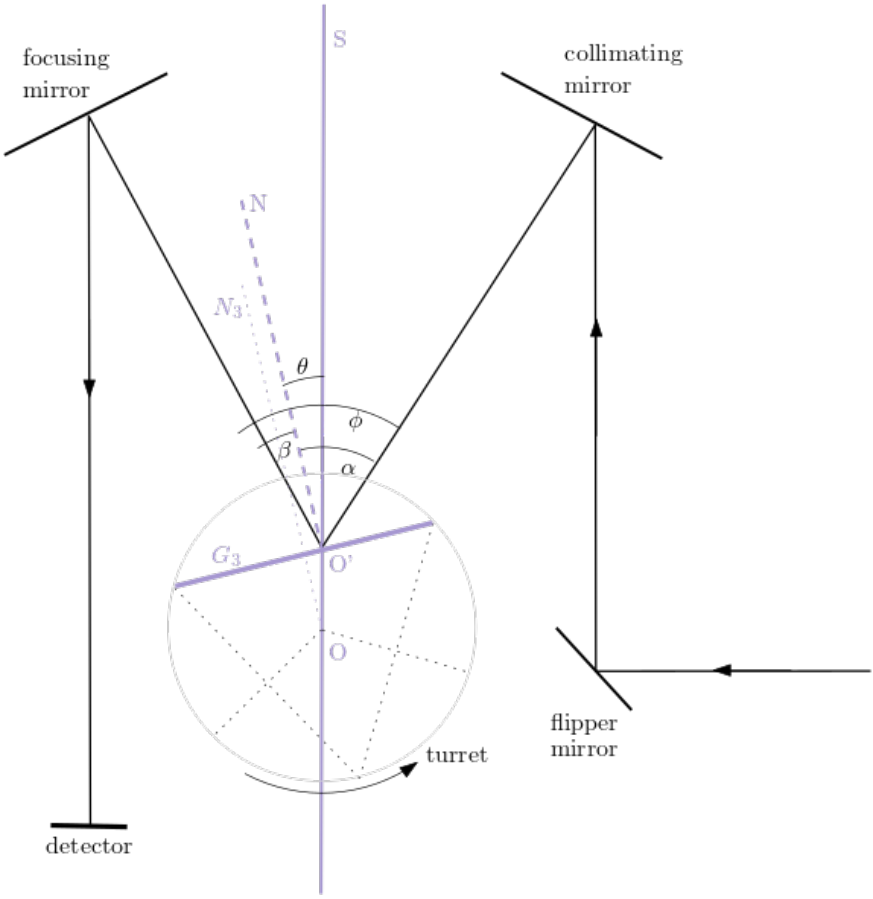

(a) Schematic view of the optical layout, indicating the angles used for estimating the dispersion.

(b) A photograph of the optical layout, with and indicated light ray path.

Figure 4.2: Czerny-Turner layout of the Shamrock spectromete.r

The "i" in the "iSTAR" stands for *intensifier*, meaning that, in addition to the CCD sensor, these cameras are equipped with the Generation 2 image-intensifier tube. The purpose of the intensifier tube is to amplify the low-level light signal and it is positioned in front of the CCD detector. The amplification is carried out by three elements within the intensifier tube. First, the diffracted light ray that falls on the focal plane of the spectrometer is converted into electrons at the photocathode. These photoelectrons then pass through the micro-channel plate, where they multiply and accelerate to the phosphor screen. The electrons striking the phosphor screen are converted back to the photons that arrive at the CCD detector matrix through the fibre optic plate. This whole process is controlled by the voltage applied to the photocathode with respect to the entrance of the micro-channel plate, generally referred to as the *gating*. If this voltage is positive, the electrons will not leave the cathode (the intensifier is effectively switched off), making the intensifier tube a rapid optical shutter. The iStar camera is completely controllable through the Andor Solis software, used to define the gate pulse (width, delay and step, in temporal units), the exposure time of the CCD sensor, the data recording method (a single spectrum, a number of consecutive spectra in a kinetic series or a number of accumulated spectra) and the readout mode (binning options, full or multi-track).

The spectra are saved as either a two- or an eight-column matrix, where the first data column is reserved for the horizontal pixels (that are remapped to wavelength), and the remaining column(s) are the "counts". Due to the intensifier tube preceding the CCD sensor, photons can only be counted for the very weak signal strength. "Counts" here denote the basic data units, or events, which are carried by a pixel as a measure of the collected light intensity, and originate from the digitization of the charge within each CCD pixel from the initial analog signal to a binary number. In addition, the presence of the intensifier tube in the optical path causes the Lorentzian wings on the final spectral line shape [4.2]. Since the spectral line of interest is well-isolated, and it is only the wavelength change of this spectral line that is monitored for the purpose of measuring the electric field, the noted influences of the intensifier tube on the final spectra are not presenting an issue.

The Disperser is the core part of the equipment in this work because it provides a spectral resolution that is high enough for the conventional spectrometer to be used instead of the laser-aided diagnostic. The lowest resolution limit for exploring the E(dλ) dependency, i.e. Fig. 2.10 or Fig. 3.6, is set by this element. Dispersion is achieved by diffraction of the light on the plane holographic grating with a groove density of $g = 3600\,\text{lines/mm}$, corresponding to the groove spacing of $d = 1/g = 278\,\text{nm}$.

Mapping pixels to wavelength

For the optical layout described above and depicted in Fig. 4.2, and the wavelength of the ray λ_0 that falls onto the grating under incidence angle α, the constructive interference of the light wave reflected from a large number of grooves occurs when:

$$ng\lambda_0 = \sin\alpha + \sin\beta, \tag{4.1}$$

where β is the angle of diffraction with respect to the grating normal (in Fig. 4.2 N is the translation of the N_3[2]) and n is an integer which counts the repetition of the interference pattern, i.e. the spectral order of diffraction (generally known as the grating order). The equation Eq. 4.1 is the grating equation.

To access the target wavelength, $\lambda_0 = 447.147\,\text{nm}$, the order of diffraction is set to $n = -1$. For the higher orders, for example $n = \pm 2$, λ_0 is at $\lambda_0 = 894.3\,\text{nm}$, which is out of the mechanical range of the grating. The turret is then mechanically rotated around the axis of the instrument to the pre-calibrated position corresponding to the desired optical range. Since the spectral line at $\lambda_0 = 447.147\,\text{nm}$ is the only one of interest for this study and no wavelength scan is necessary for the measurements, the turret is rotated until λ_0 from the helium calibration lamp is in the middle of the horizontal axis of the detector matrix. In the case of a multi-channel set-up, used for spatially resolved measurements of the electric field, the center of the horizontal axis of the detector matrix is reserved for the image projected by the fourth fibre in a bundle of seven, Fig. 3.11. In this work the lower-resolution gratings mounted on the turret, beside the one described here, were not used.

The spatial spread of the diffracted light ray on the detector plane, the (reciprocal) linear dispersion, under the constant angle of incidence is calculated as

$$\frac{d\lambda}{dx} = \frac{1}{F}\left(\frac{d\beta}{d\lambda}\right)^{-1} = \frac{\cos\beta}{Fgn}, \tag{4.2}$$

which is inversely proportional to the focal length of the spectrometer, F, and the angular dispersion of the grating, $\frac{d\beta}{d\lambda}$.

[2] In this arrangement, while the turret rotates around its vertical axis, O, the grating G_3 will slide off the axis of the system S. The incident and reflected beams are collimated and parallel, therefore the geometrical translation does not change the trigonometry used in this section.

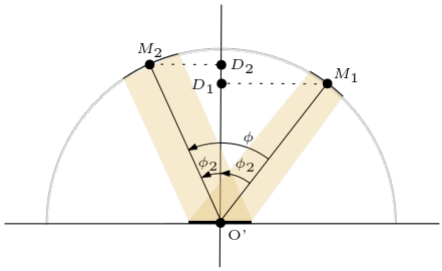

Figure 4.3: Trigonometry used to measure the opening angle.

As can be inferred from Fig. 4.2, the angle of diffraction is better expressed in terms of the system's angles. This is because the position of the mirrors and the detector are fixed, and the target wavelength is accessed only by the rotation of the turret. The angles of interest are then the grating inclusion angle, ϕ, which is a feature of the Czerny-Turner optical arrangement and originates from the lateral distance between the two mirrors and their distance from the grating [4.3], and the working angle (or the angle of rotation of the turret, or the scanning angle, depending on the literature used), θ, between the translated grating normal N and the axis of the system S:

$$\begin{aligned} \phi &= \alpha - \beta, \\ \theta &= \arcsin\left(\frac{ng\lambda_0}{2\cos(\phi/2)}\right), \\ \beta &= \theta - \phi/2. \end{aligned} \tag{4.3}$$

The inclusion angle ϕ is fixed and, as a feature of the equipment used, it can be deduced by measuring the location of each element, as depicted in Fig. 4.3. The figure shows the light beam reflected from the collimating mirror and the grating positioned in the $n = 0$ order, onto the focusing mirror. The inclusion angle is then the angle between the center of these two collimated beams, and can be separated into the part on the right side of the normal, $\measuredangle M_1 O' D_1$, and the part on the left side of the normal, $\measuredangle M_2 O' D_2$, where M_1 and M_2 are the center of the collimating and the focusing mirror respectively, D_1 and D_2 are the projections of these points on the normal, which in the case of the $n = 0$ order coincides with the system's main axis S, and O' is the same as in Fig. 4.2. Following the sketch on Fig. 4.3, the angle ϕ is then found according to the basic trigonometric rules:

$$\phi = \arctan\left(\frac{\left|\overline{D_1 M_1}\right|}{\left|\overline{D_1 O'}\right|}\right) + \arctan\left(\frac{\left|\overline{D_2 M_2}\right|}{\left|\overline{D_2 O'}\right|}\right). \tag{4.4}$$

For the equipment used, the inclusion angle is $\phi = 15.56°$, the working angle

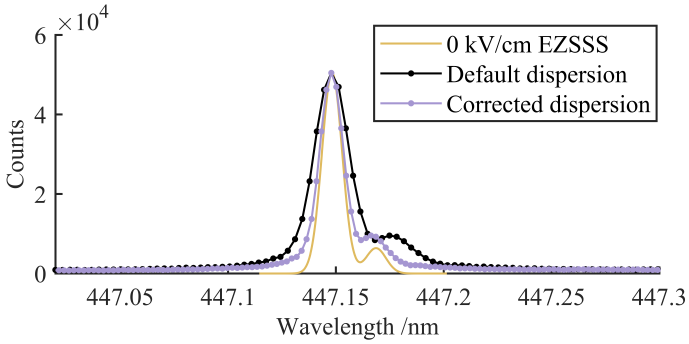

Figure 4.4: The comparison of the linear dispersion resulting from a pre-calibrated settings provided by the manufacturer and the linear dispersion corrected in the re-mapping procedure described in this section with the tabulated values of the same spectral line centered at the detector shows an improvement by about a factor of two.

for centring the $\lambda_0 = 447.147\,\text{nm}$ at the $n = -1$ order of dispersion is $\theta = 54.33°$, implying $\beta = -62.11°$. The negative sign refers to the fact that the angle of incidence and the angle of diffraction are on the opposite sides of the grating normal. These angles lead to the following linear dispersion:

$$\frac{d\lambda}{dx} = 0.1765\,\frac{\text{nm}}{\text{mm}}. \tag{4.5}$$

Taking into account the width of a pixel in a detector matrix, the spatial spread, if assumed linear, is

$$\frac{d\lambda}{dp} = \frac{d\lambda}{dx} \times 13\,\frac{\mu\text{m}}{\text{pixel}} = 0.0023\,\frac{\text{nm}}{\text{pixel}}, \tag{4.6}$$

and with that the horizontal axis is remapped from pixels, p_i to wavelength λ_i, according to:

$$\lambda_i = \lambda_0 + \frac{d\lambda}{dp}(p_i - p_0) + \frac{1}{2}\frac{d^2\lambda}{dp^2}(p_i - p_0)^2, \tag{4.7}$$

where $p_0 = 512$ is the pixel at the horizontal middle of the CCD sensor, corresponding to the wavelength centred on it by the spectrometer, λ_0.

The entrance slit

The entrance slit is the final hardware element that can affect the resolution of the system. The wider the slit, more light is transmitted inside of the spectrometer, at the expanse of the resolution. The optimal[3] width of the entrance slit for

[3]The full extent of the slit width optimization process for the system used for this work is given in [4.4].

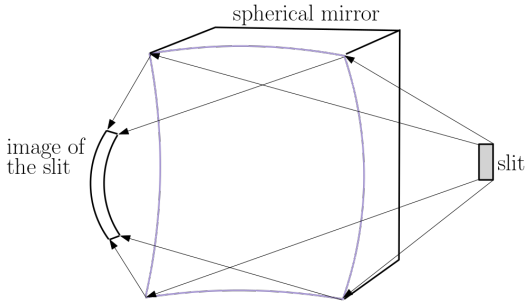

Figure 4.5: Optical aberration resulting from a spherical mirror. Adapted from [4.5].

the system is therefore set on 15 μm.

The improvement resulting from the described optimization and remapping is clearly visible when compared with the "default" wavelength axis, i.e. the dispersion given as the output of the Andor Solis recorded spectra, as is shown in Fig. 4.4.

Aberrations

The strongest aberrations, or distortions of the ideal image transfer over the optical path of the spectrometer, are encountered when recording with the multichannel installation, Section 3.2. The noted distortions are the elongations of the image from the channels along the vertical axis and the deviation on the horizontal axis of the detector matrix. They originate from the combination of the large focal length, the use of spherical mirrors to collimate and focus the rays inside of the spectrometer, and the straight entrance slit, as sketched in Fig. 4.5.

The elongation of the image can result in a strong, if not complete, overlap of the signal from the adjacent channels. In order to remedy this issue, additional optics are mounted on the light path prior to the slit, which add the spatial separation between the seven channels, as shown in Fig. 3.9.

The deviation in the projection on the horizontal axis of the detector, which manifests as a parabola in the vertical direction, is well visible in the Fig. 3.11. It is described with a fit function

$$\delta\lambda = 0.0085N^2 - 0.04557N + 0.04716, \tag{4.8}$$

where $\delta\lambda$ is the deviation from the centred wavelength λ_0 for each N (integer) fibre (channel) in a bundle.

4.2 Data analysis and the fitting procedure

The procedure used to fit the spectral line profile is the critical element of the sub-pixel accuracy when determining the wavelength of the experimentally recorded spectral lines. Based on the experimental data and the specified mathematical function that describes the line shape, the objective of the fitting routine is to optimize the line-shape parameters to minimize the difference between the model and the data. The routine used for this purpose is written in MATLAB and is largely based on Tom O'Haver's essay "A Pragmatic Introduction to Signal Processing" [4.6], and the examples given within it.

As pointed out several times in this manuscript, the line shape of the experimentally recorded $\lambda = 447.147\,\text{nm}$, either from the helium calibration lamp or the region of interest in IShTAR's plasma, is best represented with the Voigt function. This is because the intensifier tube in front of the CCD detector introduces Lorentzian wings on a predominately Gaussian-like spectral line shape, which originates from the Doppler and the Instrument broadening. However, the pseudo-Voigt approximation function, $p\mathcal{V}$, is used to fit the experimental data. This is an assumption primarily made due to the simplicity of the implementation, since it is a linear combination of Gaussian, $\mathcal{G}$, and Lorentzian, $\mathcal{L}$, functions instead of their convolution:

$$\begin{aligned} p\mathcal{V}_j(\lambda_j,\lambda_c,\mathrm{W},\eta) &= \frac{\eta}{100}\mathcal{G} + \left(1-\frac{\eta}{100}\right)\mathcal{L}, \\ \mathcal{G}_j(\lambda_j,\lambda_c,\mathrm{W}) &= \mathrm{e}^{-\ln 2\left(\frac{\lambda_j-\lambda_c}{\mathrm{W}/2}\right)^2}, \\ \mathcal{L}_j(\lambda_j,\lambda_c,\mathrm{W}) &= \frac{1}{1+\left(\frac{\lambda_j-\lambda_c}{\mathrm{W}/2}\right)^2}, \end{aligned} \tag{4.9}$$

where $\lambda_j, \lambda_c, \mathrm{W}$ stand for the j^{th} point on the wavelength axis, the wavelength at the maximum of the fitted peak and its Full Width at Half Maximum (FWHM) respectively. λ_c and W are the parameters that the fit provides as the output[4]. η is the percentage of the Gaussian character in the combination of the two functions, which is usually known before the main fitting routine starts (by fitting, for example, a calibration light profile with fixed λ_c and W and adjusting η until the best fit is achieved) and is then fixed for the set of data.

Because the fit-function is a blend of two non-linear functions, the traditional approach to curve fitting by transforming $\mathcal{G}$ and $\mathcal{L}$ into a form that allows for the linear polynomial fit (i.e. the linear least squares) is not preferable. In addition, after subtracting the reference dark spectrum from the experimental

[4] One of the steps in the data post-processing is to normalise the recorded spectra, for the visual comparison of the experimental and simulated spectra as the default output from the EZSSS is also normalised to unity. Thereby the height, or the amplitude, coefficient of the fit-function is omitted.

data, the resulting spectra may not necessary be positive everywhere for the linear least squares approach to work. Finally, tracing the error propagation under such transformation is hard and the noise (regardless of its level) is also affected. For these reasons a derivative-free iterative curve fitting method is used.

The iterations adjust the parameters λ_c and W of the mathematical model, Eq. 4.9, until the model fits the data with the prescribed accuracy, i.e. until the fitting error is minimal. This is achieved in the following way. First the input is defined. A 2D data matrix $[x, y]$ is created for each optical channel after minor corrections are performed on the experimental data sets. The first column is the wavelength axis, after the remapping procedure is applied (Eq. 4.7). y are the "Counts" after the subtraction of the signal recorded from the same location with the photocathode in the intensifier tube turned ON, but without the plasma nor the glow discharge of the calibration lamp (which is referred to as the *reference dark spectrum*), and the peaks are normalized to the unit area in the resulting spectrum. The $[x, y]$ matrix is specified along with the initial guess for λ_c and W for each of the N number of peaks (in this work there was no need to go above N=2) and fed to the code as a vector: $\Lambda^0 = [\lambda^0_{c1}, \mathrm{W}^0_1, \lambda^0_{c2}, \mathrm{W}^0_2, \cdots]$. The required accuracy, Ac, and the number of attempts the routine has to achieve it, Nt, must also be provided. From here, the optimization function is created, which in the first iteration step is a difference between the model function from the start parameters and the data sample.

The pseudo-code for creating the optimization function from the input arguments Λ^0, x, y and η is given in Algorithm box 4.2.1. This part of the fitting routine computes the model and, by comparing it to the supplied data, it returns the fitting error.

Algorithm 4.2.1: OBJECTIVE = OPTIMIZATIONFUNCTION(Λ^0, x, y, η)

% Build matrix [A] containing the model for each peak
for each i^{th} peak of N
do $A_i = p\mathcal{V}_i(x, \lambda_{ci}, \mathrm{W}_i, \eta)$;
% Solve Ah = y to get the peaks' heights h
$h = [A]^{-1} \times y$;
% Compute the sum of all N model peaks
$m = [A] \times h$;
% Compute the difference between the model m and the data y
objective = $\|m - y\|$;

To find the minimum of the Optimization Function, the iterative process replaces the worst solution with a new (potentially better) one at each step until the optimal solution is found. The parameters are adjusted in a type of a

pattern-like search called the Nelder-Mead simplex algorithm. The simplex is a "search area" created from random and starting point values. It is an object with $(n+1)$ vertices for the nD space (e.g. a triangle in a 2D search space) where each vertex is one result of the Optimization Function for different set of parameter values. The simplex "moves" through the search space according to the set of rules [4.7, 4.8] in a series of steps within each iteration (it reflects, expands, contracts and shrinks) while adjusting the parameters of the worst vertex towards its centroid - a geometric center of the all the vertices except the worst one. The optimization has converged if the simplex is small enough, i.e. the vertices are close enough, evaluated by comparing the output after each iteration of the optimizer with the lower bound on the step size - Tol[5]. This whole optimization procedure is implemented with the `fminsearch` solver in MATLAB[6].

The pseudo-code for the fitting procedure is given in the Algorithm box 4.2.2.

Algorithm 4.2.2: $\mathscr{M}$ = FITTINGFUNCTION$(x, y, N, \Lambda^0, \eta, \mathrm{Nt}, \mathrm{Ac}, \mathrm{Tol})$

while Nt not reached **loop**

{
% Optimze the OptimizationFunction for $\Lambda = [\lambda_{c1}, W_1, \lambda_{c2}, W_2, \cdots]$
Λ^T = `fminsearch`(@Λ(OptimizationFunction(Λ, x, y, η), Tol));
% Construct the trial model from $\Lambda^T = [\lambda_{c1}^T, W_1^T, \lambda_{c2}^T, W_2^T, \cdots]$
for each i^{th} peak of N
  do $A_i = p\mathscr{V}_i(x, \lambda_{ci}^T, \mathrm{W}_i^T, \eta)$;
$m^T = [A^T] \times h$;
% Compute the difference between the trial model and the data
FitError = $\left\| m^T - y \right\|$;
if FitError < Ac
  then {Height $\leftarrow h$; BestFitParameters $\leftarrow \Lambda^T$;}
}
end loop
% Construct the fit model from BestFitParameters $= [\lambda_{c1}^b, W_1^b, \lambda_{c2}^b, W_2^b, \cdots]$
for each i^{th} peak of N
  do $\mathscr{A}_i = p\mathscr{V}_i(x, \lambda_{ci}^b, \mathrm{W}_i^b, \eta)$;
$\mathscr{M} = [\mathscr{A}] \times$ Height;
return (BestFitParameters, $\mathscr{M}$)

The final output are the optimized λ_c and W of the two peaks in the line shape of the target spectral line of He I, and the complete model function $\mathscr{M}$ that is typically plotted in the graphical representation of the experimental results (e.g. in Fig. 3.3 and Fig. 3.14).

[5] Tol is requested, and has the meaning of $\left\| x_j - x_{j+1} \right\|$.

[6] https://de.mathworks.com/help/matlab/ref/fminsearch.html

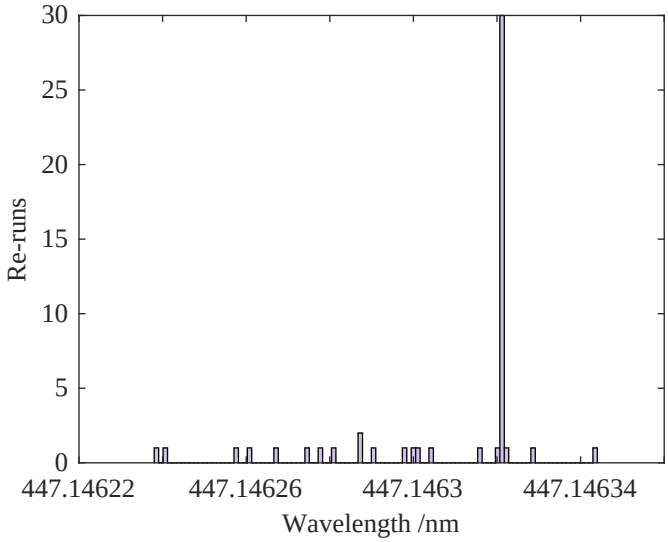

Figure 4.6: Histogram of occurrence of the calculated line position at the horizontal and vertical center of the CCD chip for 50 total re-runs of the fitting routine with Nt = 100 trials.

Weak convergence is one of the issues that this iterative method suffers from. The optimiser will always converge, but the iterations are likely to reach the limit in the number of trials before the estimated error is less than the one required. In addition, since the FitError is calculated in the y-direction (peak intensity) rather than the x direction (peak position), it is advisable that the routine is carried out several times and the final estimates of the peak position compared. This is mainly due to the fact that the goodness of the fit by this particular routine depends on the line-shape function (where η can be poorly predicted), signal-to-noise ratio and the number of data points treated by the fit.

As an example of the convergence stability test, the fitting procedure was performed 50 times on the spectral line of helium recorded from the calibration lamp as shown in Fig 3.3, for which the wavelength axis was already remapped and the reference dark spectrum subtracted. The histogram in Fig. 4.6 represents the number of occurrences of the calculated position of the dominant peak for 50 total re-runs of the fitting routine with Nt = 100 trials. The random character of the result is due to the small but random alteration in Λ_0 vector for each of the 50 re-runs. The position λ_c = 447.14632 nm was found in 30 re-runs. In comparison, all other results span across the window 447.14622 – 447.14635 nm and occur mostly once. However, this values are still less then the requested Tol = 0.001, and therefore the convergence was successful. The calculated value which occurs most often is taken for estimating the wavelength

shifts, and ultimately, the electric field.

4.3 Measurement error analysis

The study of the measurement uncertainties discussed in this section is based on the classical theory of error propagation, as found in [4.9] and [4.10].

The starting point for this analysis is the identification of the sources of the uncertainty. This is facilitated when the measurement procedure is broken down into simpler steps. The diagnostic method described in this thesis has three distinct phases. First the measurements of a *direct* quantity are made - a spectrum (wavelength vs. intensity of the collected light) is recorded. Second, the *intermediate* quantity is inferred from a parameter estimated from the data - a Stark shift is determined from the position of the emission spectral line peak that is obtained by fitting. From here, the next step is to calculate the electric field intensity based on a theoretical model for the Stark effect on the 447.15 nm line of He I and for a given experimental geometry. The electric field is the *measurand*. The key equations of the method, when applied for the work presented through this manuscript, are Eq. 2.68 and Eq. 3.2, which express the E(dλ) dependence in the form:

$$\mathrm{E}(\mathrm{d}\lambda) = C_1 \mathrm{d}\lambda + C_2 \mathrm{d}\lambda^{0.5} + C_3 \mathrm{d}\lambda^{0.25}, \tag{4.10}$$

where C_1, C_2 and C_3 represent the coefficients originating from the polynomial fit applied on the results of the synthetic spectra (Ch. 2) and should toggle different modelled behaviour used.

With these three steps in mind, and also in accordance with [4.11], the origins of the uncertainty are:

- Random error during the measurement,
- Systematic error during the measurement,
- Systematic error due to fitting, and
- Systematic error introduced by the model of the Stark effect.

Random error during measurements

The origins of the random error during the recording of the spectrum are related to the photon noise and the noise generated by the intensifier tube, which together lead to the error due to the "event recognition" on the counting detector. On the other hand, because the parameter which propagates the error to the

measurand is on the wavelength axis (horizontal), and the photon and intensifier noise contribute to the uncertainty in the intensity axis (vertical), the noise level does not require precise quantification.

However, with the improvement of the signal-to-noise ratio, the optimization of the systematic errors, in particular those due to the fitting of the spectra, can be greatly improved. To this end, a variety of steps are therefore taken, most of which have been elaborated in the preceding sections of this chapter. In addition, the discharges in IShTAR are long enough to allow for long exposure times when recording the spectra(Chapter 3). This leads to a better defined "event" that the sensor registers, as the random noise level relative to the spectral line intensity decreases with the amount of photons received. Furthermore, multiple long-exposure recordings are added together during the post-processing of the data, leading to the cancellation of the random events captured by the CCD sensor. Lastly, the reference dark spectrum is subtracted from each measurement. In order to ensure that the contribution from the intensifier tube is included in the reference, the tube is turned on during the recording of the dark spectra.

In order to prevent the light scattered inside the spectrometer from being recorded, a protective sheath was added to the grating turret, as seen in Fig. 4.2. This thin black velvet sheath is attached to the frame of the grating holder, extending it in such a way that it blocks the light from the spectrometer's collimating mirror to accidentally reflect off a different grating and onto the focusing mirror.

The final spectrum, pre-normalization, looks like in Fig. 3.12, and the number of the events (Counts) is mainly within the spectral line while the noise level is small in comparison ($\sigma_{\text{noise}} = 0.7\%$). However, this line of reasoning must be re-examined when shorter exposure times are required and when the low-level signal becomes incurable by the means stated above.

Systematic error during measurements

Systematic errors during the measurements of emission spectra are known to be a drift, or a bias, of the recorded data and thus restrict the precision of the method. The main source of such uncertainties in this work is the re-mapping of the horizontal axis of the CCD matrix, from pixels to wavelengths, i.e. the wavelength axis calibration.

Looking back at Eqs. 4.7, 4.6, 4.3 and 4.2, it is clear that the errors which propagate are the uncertainty in the estimated inclusion angle ϕ, and the uncertainty in the measured focal length F.

The uncertainty in the estimated best value for the inclusion angle ϕ, as given by Eq. 4.4, is calculated based on the error propagation rules. The best value of ϕ is estimated from the values of $\left|\overline{D_1M_1}\right|$, $\left|\overline{D_1O'}\right|$, $\left|\overline{D_2M_2}\right|$ and $\left|\overline{D_2O'}\right|$,

which are also derived from the directly measured quantities:

$$\begin{aligned}
\left|\overline{D_1M_1}\right| &= y_1 - y_{m1} \quad &= 0.0720 \pm 0.007\,\text{m},\\
\left|\overline{D_1O'}\right| &= x_1 - x_g \quad &= 0.5922 \pm 0.007\,\text{m},\\
\left|\overline{D_2M_2}\right| &= y_2 - y_{m2} \quad &= 0.0885 \pm 0.007\,\text{m},\\
\left|\overline{D_2O'}\right| &= x_2 - x_g \quad &= 0.5838 \pm 0.007\,\text{m}.
\end{aligned} \tag{4.11}$$

y_1, x_1 and y_2, x_2 are the coordinates of points D_1 and D_2 respectively, determined with a centimetre-graduation ruler in the coordinate system whose $(0,0)$-origin is set in the corner of the spectrometer nearest to the focusing mirror, Fig. 4.2, with the x-axis oriented along the long side of the spectrometer (length) and the y-axis along the shorter side of the spectrometer (width). y_{m1} and y_{m2} are the y-coordinates of points M_1 and M_2. x_g is the x-coordinate of the point O' determined in the same coordinate system. The best estimate for each quantity and its uncertainty, as the quadratic sum of the original error due to interpolation between the graduations on the ruler, are also listed in the Eq. 4.11.

The further propagation of the error in the length measurements to the uncertainty in ϕ, and the quantities that follow all the way to $\frac{d\lambda}{dp}$, is calculated in accordance with the general rule for estimating the uncertainty in a function of many variables. This rule states ([4.9]) that *"if the quantities $x, \cdots, z$ are measured with (independent and random) uncertainties $\delta x, \cdots, \delta z$ and the measured values are used to compute $q = q(x, \cdots, z)$, the uncertainty in q is*

$$\delta q = \sqrt{\left(\frac{\partial q}{\partial x}\delta x\right)^2 + \cdots + \left(\frac{\partial q}{\partial z}\delta z\right)^2}\,."\tag{4.12}$$

In order to evaluate the uncertainty in the estimated value from the measured values, the first step is therefore to calculate separately the partial uncertainty in the estimate that is due to uncertainty in the individually measured values, and then to combine these in quadrature.

Following these steps, one finds that the relative uncertainty in the inclusion angle $\phi = 15.56^\circ \pm 6\%$ propagates to the uncertainty in the dispersion angle (Eq. 4.3) $\beta = -62.11^\circ \pm 6\%$.

The focal length F is estimated from the best non-linear fit of the optical emission spectra recorded from different calibration lamp sources, with multiple lines.

For the purpose of the analysis presented here, two spectra with multiple known and tabulated (in the NIST spectroscopic tables) values for the spectral line wavelengths are recorded. One spectrum is the emission from the calibration lamp of helium, with the grating set at 413 nm central wavelength, and the other is from the calibration lamp of the argon and mercury mixture, centered

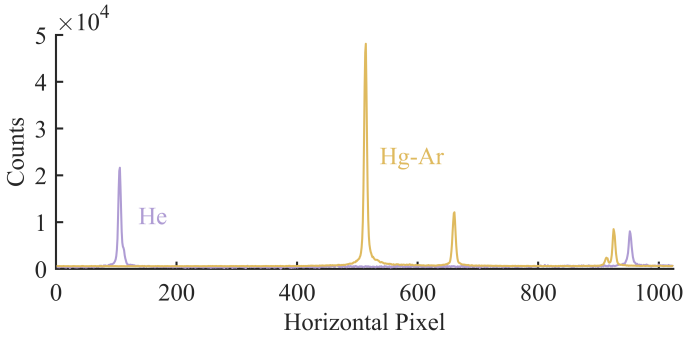

Figure 4.7: Emission spectra from helium (purple) and argon-mercury (yellow) calibration lamp are used for dispersion optimization.

at 365 nm, Fig. 4.7. The spectra are fitted with an iterative routine[7] which takes the inclusion angle ϕ as given (from the best estimate as per Eq. 4.4). The routine adjusts the focal length F, thereby changing the wavelength dispersion that remaps the horizontal pixels to the wavelength until the spectral line separation in nm matches the separation between these lines found from the NIST spectroscopic tables.

The non-linear fit yields an uncertainty in finding the center of the peak from the data being $\sigma_{px} = 0.3 \times$ pixel. Therefore, the relative uncertainty in the estimate of the focal length from such fit follows from the pixel difference between the two most separated lines in each spectrum, d_{px} ($d_{px}^{\text{He}} = 846.2$ pixels and $d_{px}^{\text{Hg-Ar}} = 410.4$ pixels):

$$\frac{\delta F}{F} = \sqrt{\frac{\sigma_{px}}{d_{px}}}. \tag{4.13}$$

The stability of the linear dispersion modified by this routine is monitored with a scan through the values of the inclusion angle. The results are shown in Fig. 4.8 where the red and the blue lines represent the F vs. ϕ scan for the helium and the argon-mercury spectrum respectively. The uncertainty intervals in F for each scan are also shown. As the inclusion angle is increased, the focal length decreases and the red and blue line are closer to each other. They overlap at around $\phi = 15.7°$ while the uncertainty intervals in F start overlapping at around $\phi = 15.3°$. The solid black line shows the weighted mean of the two F values[8].

[7] The code and the calculations provided in this paragraph are courtesy of Dr. Ralph Dux.

[8] The uncertainty in F from the helium spectrum is, as seen in the above equation, a little more than twice smaller from the uncertainty in F from the mercury spectrum. Therefore the weighted mean is closer to the former.

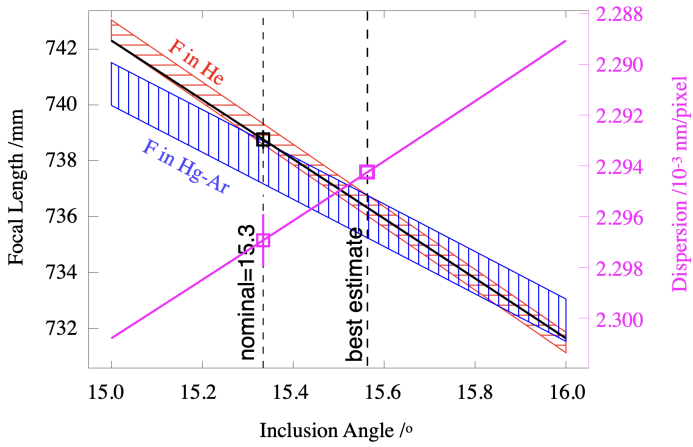

Figure 4.8: The optimization procedure for estimating the best value of the Focal Length from the two calibration lamp spectra with multiple lines, and the modified values for the linear dispersion for the scan over the inclusion angle.

The wavelength dispersion at 447.15 nm central wavelength is calculated by varying the inclusion angle and the weighted mean value of F. In Fig. 4.8 the results are shown with a magenta line and scale. The best estimate for wavelength dispersion at 447.15 nm is based on the best estimate for the inclusion angle from Eq. 4.4, $\phi_{best} = 15.56°$, and Eq. 4.6. The dispersion calculated from the nominal value of the inclusion angle, obtained from the above iterative fit, is also shown in the figure. The errorbar on the nominal and the best-value estimate only takes into account the uncertainty in the wavelength dispersion due to the uncertainty in the estimated focal length. However, the prevailing uncertainty is due to uncertainty in the inclusion angle, which is greater than the axes in this figure.

Following the general rule on the propagation of uncertainties, Eq. 4.12, one eventually arrives at the uncertainty in the wavelength dispersion:

$$\frac{d\lambda}{dp} = 0.0023 \pm 0.0003 \frac{\text{nm}}{\text{pixel}} = 0.0023 \frac{\text{nm}}{\text{pixel}} \pm 12\%.$$

Compared to the uncertainties in the other terms seen in Eq. 4.7, the uncertainty in the wavelength dispersion is by far the dominant one and is thus the key contributor in the uncertainty in the calibrated values on the wavelength axis. The uncertainty in λ_i is ±12%.

This random error in the calibration is the main systematic error in the measurement, which in general degrades the precision of the instrument and the method and, unlike the random measurement error, can not be reduced by making a large number of acquisitions.

Systematic error due to fitting

Another source of uncertainty in the estimate of wavelength, which leads to uncertainty in the estimate of the electric field strength, is the accuracy of model parameters provided as an output of the fitting routine described earlier, in Section 4.2. As was mentioned, and following the analysis outlined in [4.6], the the parameter errors depend on the accuracy of the model used to fit the data and the start parameter vector, since it is more likely that the number of trials will be reached before the fitting routine converges. Nevertheless, the error in the estimate of the peak position is far smaller in comparison with the error in the other parameter - the FWHM, and is usually less then 0.5% for a single run of the fitting routine.

This relative error of the fit is further reduced with the histogram analysis of the outputs and their recurrence rate over several re-runs of the fitting routine, as it is the value or the peak wavelength with the highest recurrence that is taken for the evaluation of the electric field strength. The uncertainty interval in the estimate of this fit parameter is taken to be the whole interval of values enclosed by the histogram, with the upper bound being the (user-)prescribed Tol optimisation value.

For the sets of data used in the work and presented in this manuscript Tol = 0.001, which leads to the maximum systematic error in the estimate of wavelength that is due to the fitting procedure to be 0.0002%.

Systematic error introduced by the model of the Stark effect

The uncertainty in the behaviour modelled with the curves in Fig. 3.6 and Fig. 2.10 is best described with the standard deviation of the best fit. The uncertainty interval is then given, as for example in Fig. 4.9, within an upper and lower confidence bound. Such interval captures the error due to the fit of the modelled behaviour but also the non-ideal behaviour of the modelled sample points which is due to the small uncertainty in the peak-recognition on the synthetic spectrum and the uncertainty that is due to the imprecisely defined geometry - both of which are here assumed to have been minimised.

The cumulative uncertainty in the estimate of the measurand, the intensity of electric field, is calculated in the following way. The dominant cause of uncertainty in the estimate of the peak's central wavelength is attributed to the systematic error due to calibration, which amounts to the uncertainty in λ_i of $\pm 12\%$. The easiest way to propagate this error to the error in E and also include the standard deviation of the coefficients of the fitted curve which represents the (inverse) model of the Stark effect E(dλ), Eq. 4.10, is to calculate the uncertainty interval in E as:

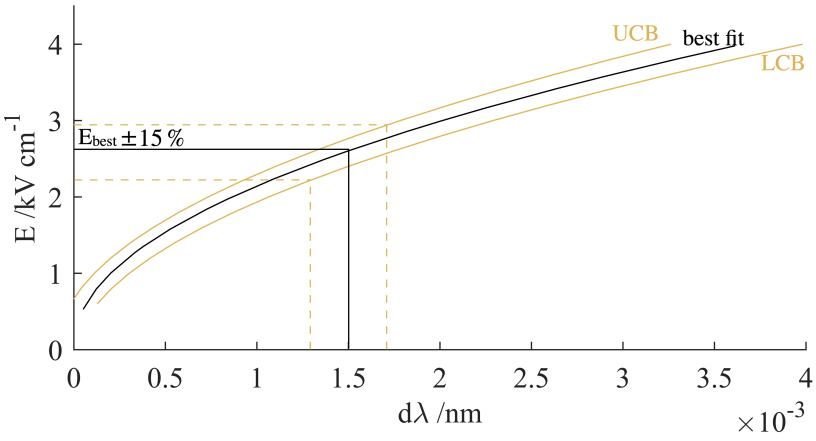

Figure 4.9: Uncertainty in electric field intensity, as estimated when taking into account the upper (UCB) and lower (LCB) σ confidence bounds of the fit coefficients and the uncertainty in the measured wavelength.

$$\mathrm{E}^{up} = \left(C_1^{best} + \sigma_{C_1}\right)\left(\mathrm{d}\lambda^{best} + \delta(\mathrm{d}\lambda)\right) + \left(C_2^{best} + \sigma_{C_2}\right)\left(\mathrm{d}\lambda^{best} + \delta(\mathrm{d}\lambda)\right)^{0.5} + \left(C_3^{best} + \sigma_{C_3}\right)\left(\mathrm{d}\lambda^{best} + \delta(\mathrm{d}\lambda)\right)^{0.25} \tag{4.14}$$

and

$$\mathrm{E}^{low} = \left(C_1^{best} - \sigma_{C_1}\right)\left(\mathrm{d}\lambda^{best} - \delta(\mathrm{d}\lambda)\right) + \left(C_2^{best} - \sigma_{C_2}\right)\left(\mathrm{d}\lambda^{best} - \delta(\mathrm{d}\lambda)\right)^{0.5} + \left(C_3^{best} - \sigma_{C_3}\right)\left(\mathrm{d}\lambda^{best} - \delta(\mathrm{d}\lambda)\right)^{0.25}, \tag{4.15}$$

where the confidence in the coefficients C_1, C_2 and C_3 is expressed with $\pm\sigma_{C_{1,2,3}}$, and the uncertainty in wavelength (or the wavelength shift) is given with $\pm\delta(\mathrm{d}\lambda$.

This should be done for each data in the calculation of the measurand. In an example shown in Fig. 4.9, the best estimate originates from the modelled data described by the best fitted curve (black full line) and for a given data point the upper and lower uncertainty bounds in E are found to be ±15% (yellow dashed line). It is noticeable form the depicted example that neglecting either the uncertainty in the wavelength shift estimate or the uncertainty in the modelled coefficients, leads to the underestimate of the final uncertainty in the measured electric field strength.

References

[1] Anne P. Thorne. *Spectrophysics.* Springer, Dordrecht, second edition, 1988.

[2] Raymond J. Fonck. *Multichannel Extreme UV Spectroscopy of High Temperature Plasmas.* In Multichannel Image Detectors, volume 2, chapter 14, pages 277–296. American Chemical Society, nov 1983.

[3] Wilfried Neumann. *Fundamentals of Dispersive Optical Spectroscopy Systems.* Society of Photo-Optical Instrumentation Engineers (SPIE), 2014.

[4] Tessa Verstrynge. *Spectroscopic diagnostics of IShTAR plasma.* Master's thesis, GhentUniversity, Belgium, 2018.

[5] Horriba.com (n.a.). *Spectrometers, Monochromators and Spectrographs.* `https://www.horiba.com/en_en/technology/measurement-and-control-techniques/spectroscopy/spectrometers-and-monochromators/spectrometer-monochromator/`. [Online; accessed 02.11.2020.].

[6] Tom O' Haver. *A Pragmatic Introduction to Signal Processing.* Independently published, October 2020 edition, 1997.

[7] J. A. Nelder and R. Mead. *A Simplex Method for Function Minimization.* The Computer Journal, 7(4):308–313, jan 1965.

[8] Jeffrey C. Lagarias, James A. Reeds, Margaret H. Wright, and Paul E. Wright. *Convergence Properties of the Nelder–Mead Simplex Method in Low Dimensions.* SIAM Journal on Optimization, 9(1):112–147, jan 1998.

[9] John R. Taylor. *An Introduction to Error Analysis: The Study of Uncertainties in Physical Measurements.* University Science Books, 2nd edition, 1997.

[10] *Eurachem/CITAC guide: Quantifying Uncertainty in Analytical Measurement.* `www.eurachem.org`. ISBN: 978-0-948926-30-3.

[11] R. Andrae. *Error estimation in astronomy: A guide.* arXiv: Instrumentation and Methods for Astrophysics, 2010.

5

Summary, conclusion and outlook

The goal of this doctoral thesis, titled "Electric field measurements in the vicinity of an ICRF antenna", was to propose, develop and implement an adequate diagnostic technique for determining the intensity of electric fields in the sheaths of the plasma facing structures of ICRF antennas. The data acquired with the method developed during this doctoral thesis was, until now, the essential missing ingredient to verify or redirect the theoretical description of the formation of sheaths in the vicinity of ICRF antennas. As such, this work will contribute to further optimizations of ICRF systems for tokamak plasma wave heating.

The method is based on the initial notion that the measurements of the sheath parameters must be non-invasive. Stark spectroscopy is one such technique that is widely used for measuring electric fields in plasmas. This technique exploits the well-known phenomena of atomic physics - the Stark effect, which is a manifestation of an electric field-induced shifting and splitting of atomic energy levels, leading to the wavelength shift of the spectral lines corresponding to the optical transitions between those. Stark shifts of the spectral lines of hydrogen and helium are well understood theoretically and thoroughly studied experimentally. Nevertheless, there was an interesting deficit in experimental studies in the domain of low-pressure and low-density plasmas, conditions encountered in the immediate vicinity of ICRF antennas in tokamaks and devices designed to study them (such as IShTAR). The most significant contribution of this work was the adaptation and application of Stark spectroscopy to these plasma environments.

A brief derivation of the basic requirements for the use of nuclear fusion

for the production of energy (Section 1.1) showed that the temperature of the plasma in a fusion reactor must be in the range between 10 and 20 keV for the ignition to occur. To meet this requirement external heating systems are needed. One of such method is heating with waves in the Ion Cyclotron Range of Frequencies (Section 1.3). While ICRF heating is reliable and effective in rising the plasma temperature, experimental evidence has shown that the impurity content in the core plasma increases during the ICRF heated discharges. The leading hypothesis is that often oscillating electric fields parallel to the magnetic field lines are rectified in the plasma sheath that forms at the plasma-facing components of the ICRF antenna, which leads to the build-up of a static electric field. This "rectified" static electric field exceeds the intensity of the electric field in the non-RF thermal sheaths, thereby accelerating ions to far greater energy than in the absence of ICRF-induced oscillations (Section 2.1). It is this rectified static electric field that is measured with the diagnostic developed for this thesis. The significance of this thesis for the ICRF community is that the experimentally measured electric fields in the ICRF sheaths serve as a direct link between the actual operation of the antenna and the theoretical models developed to describe the sheath formation.

The diagnostic method was developed and tested in IShTAR (Section 1.4), a linear device designed to mimic the tokamak environment of the ICRF antenna with simpler magnetic field topology and convenient access for diagnostics. Based on the properties of the optical emission spectra recorded from IShTAR's plasma with a high resolution spectrometer,the best suitable spectral line and a diagnostic parameter were chosen: the electric field diagnostic for ICRF sheaths determines the electric field intensity based on the wavelength shift of the spectral line of neutral helium atoms corresponding to the 4^3D - 2^3P transition (Section 2.2). The shifts are measured with respect to the "unperturbed" spectra recorded from the helium calibration lamp. The obtained values are introduced into the equation $E = F(d\lambda)$, which resulted from the theoretical treatment of the Stark effect with the perturbation theory method in the EZSSS synthetic spectra simulator (Section 2.3).

Three experimental configurations have been studied and were presented here in Sections 3.1 and 3.2. In the first configuration, the electric field was measured with a single channel with the view-lines terminating at the front surface of a DC-biased planar electrode. The electrode was immersed in IShTAR's plasma source along the main axis of the device. The configuration provided volume-integrated measurements of the electric fields in the sheaths on the electrode's surface. The results showed an anticipated increase of the electric field with the increased voltage applied to the electrode. For the second configuration, an optical fibre with a collimating lens was placed inside the main vacuum vessel of IShTAR and mounted on the holder 2 cm from the case of the

ICRF antenna box. This arrangement also provided volume-integrated measurements of the electric field. When the maximum available power was delivered to the ICRF antenna in IShTAR, the resulting electric field at the antenna's casing was $E = 3.4 \pm 0.3\,kV\,cm^{-1}$. The only non-speculative observation that can be made from these two configurations is that the electric field is higher when the ICRF antenna operates compared to the electric field intensities measured in the DC thermal sheaths of the planar electrode under the same plasma conditions, albeit restricted to the DC-bias of up to 3.5 kV and the power delivered to the ICRF antenna of 1 kW (Section 3.1). Better experimental scheme of comparing the two must be found to draw solid conclusions.

For the third set-up, additional optical elements were introduced to the diagnostic arrangement, namely the multi-channel optical head to allow for the spatially-resolved sheath measurements and a polarizer that filters all but the emission polarized in the direction of the electric field vector to increase the sensitivity of the measurements (Section 3.2). The results obtained from the location fixed at the antenna box were compared between the discharges that used the ICRF antenna and those that did not. They indicate that electric fields across the width of the sheath of the ICRF antenna are greater when the ICRF antenna is used during the discharge. The interpretation of the results is hindered however, by the fact that even when the ICRF antenna does not operate, the helicon antenna in the plasma source induces a wave in IShTAR's plasma the behaviour of which, and its effect on the sheath of magnetically connected material surfaces, is non-trivial.

The experimental data for all three cases was compared with a simple theoretical predictive model of the electric field intensity in the DC and the RF-modulated sheaths in plasma environments encountered in IShTAR's experiments, in Section 3.3.

The experimental results clearly demonstrate that the Stark spectroscopy was successfully adopted and used in a plasma environment found in the vicinity of ICRF antennas.

A significant aspect of the implementation of this diagnostic method was optical hardware optimization, which was required to improve the spectral resolution of the spectrometer and ultimately the resolution of the complete diagnostic, and the steps taken to reduce the random and systematic uncertainty of the method, which improved the accuracy and the precision of the electric field measurements. To this end, great care was taken with the calibration of the wavelength axis of the instrument and with identification, development and implementation of an appropriate fitting routine that extracts the wavelength of the recorded spectral lines with the necessary accuracy. This was discussed in Chapter 4.

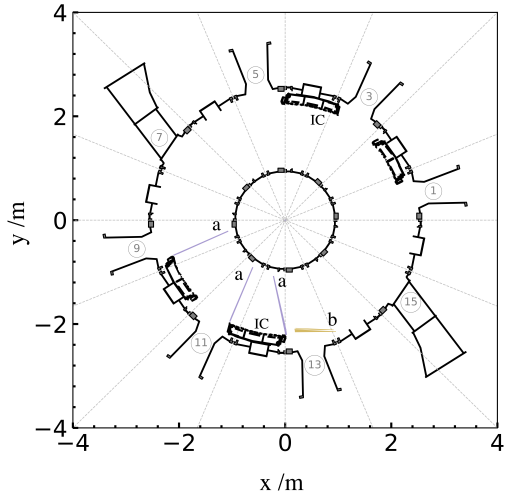

Figure 5.1: A scheme of the ASDEX Upgrade tokamak showing the toroidal location of the view-lines that may be used for electric field measurements in the vicinity of ICRF antenna. "a" (purple) are the view-lines that are used by the visible spectroscopy, which terminate on the plasma-faced side of several tiles of the ICRF antenna limiters. "b" (yellow) are the view-lines of active helium beam spectroscopy, which terminate on the leading edge of a single tile of an ICRF antenna limiter.

Outlook

The natural first suggestion in terms of diagnostic upgrade is to consider and study an option to add the temporal coordinate to the measurements. This implies testing the capabilities of the detector to record emission spectra in a way that allows for the so-called phase-resolved spectroscopy. A detector used through this thesis is a fast-gated intensified CCD camera Andor iStar with optical gating of < 2 ns and 5 MHz readout rate and built-in delay generator. This should provide a solid base to explore the possibility to synchronise the recording of the emission spectra to different phase-steps in the RF cycle of the ICRF antenna. The signal strength here depends on the number of accumulated spectra per a phase-step in a cycle, therefore the duration of the plasma discharge is one limiting factor in the applicability of this approach.

Nevertheless, if successfully adapted, the idea would be to observe the temporal changes in the sheath parameters, for example the sheath width, and evaluate the electric field strength across the sheath width through the full RF cycle of the ICRF antenna.

As designed on a linear device that only mimics the environment found in

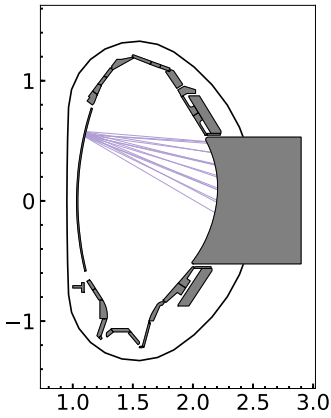

Figure 5.2: A scheme of the ASDEX Upgrade tokamak showing the poloidal location of the view-lines that may be used for electric field measurements in the vicinity of ICRF antenna.

the vicinity of the ICRF antennas in tokamaks, the true prospect for this diagnostic method is for it to be applied in a tokamak. With that aim, as promised in Section 1.5, the diagnostic was designed to be transferable to other devices in a plug and play manner. The main limitation here is the availability of the existing view lines which have to be aligned towards the limiters of an ICRF antenna.

In the ASDEX Upgrade tokamak there are two existing spectroscopic diagnostics that have their view lines ending on the ICRF limiters. Their toroidal and poloidal location are presented in Fig. 5.1 and Fig. 5.2, respectively. The toroidal locations of existing view lines that extend from the high field side towards the limiters of the ICRF antenna in sector 10, and towards the limiters on the both sides of the ICRF antenna in the sector 12, labelled as "a" in Fig. 5.1 and coloured in purple, belong to the visible spectroscopy and are poloidally distributed as shown in Fig. 5.2. The use of the diagnostic method developed in this thesis would be to provide the sheath-integrated measurements during pure helium discharges. The possibility must be explored to extend the method and use Stark effect on neutral lines of hydrogen. The electric field measured in these configurations could provide valuable insight into the RF sheath formation and rectification when different antenna optimization scenarios are compared.

The other option is to use the lines of sight that are sketched in sector 13, labelled as "b" and coloured in yellow in Fig. 5.1. These are part of the active helium beam diagnostic and therefore rely on the existing locally injected he-

lium gas.

A

Supplementary information

A.1 Averaged reactivity for fusion reactions

The reactivity for various fusion reactions, averaged over the Maxwellian distribution of relative particle velocities, as a function of temperature (in keV), is given in Fig. A.1.

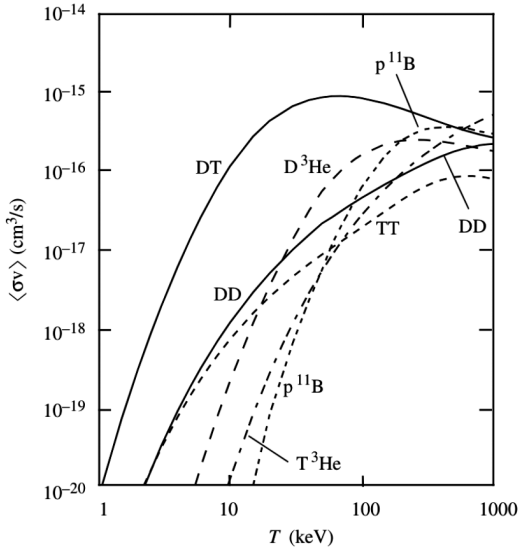

Figure A.1: Averaged reactivity for several fusion reactions as a function of temperature. From [A.1].

A.2 Bessel function of the first kind

The shape of the zeroth-order modified Bessel function of the first kind, $I_0(a)$, representing the behaviour of the RF-period-averaged electron flux through the sheath region RF-period. Consequently, the floating potential due to the RF bias for the two gases relevant for the material in this thesis is presented in Fig. A.2.

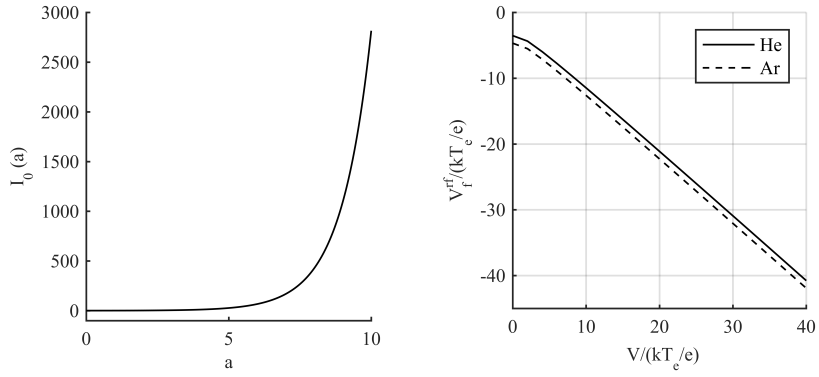

(a) Zeroth-order modified Bessel function of the first kind.

(b) Self bias

Figure A.2: The 0^{th}-order modified Bessel function of the 1^{st} kind and the the RF-modified floating potential for He and Ar.

References

[1] Jef Ongena. *Fusion: A true challenge for an enormous reward.* EPJ Web of Conferences, 98:05004, 01 2015.

B

List of publications resulting from or featuring this work

Journal Article

A. Kostic et al., "Polarization Stark spectroscopy for spatially resolved measurements of electric fields in the sheaths of ICRF antenna," Rev. Sci. Instrum., vol. 90, no. 12, p. 123101, Dec. 2019.

A. Kostic et al., "Development of a spectroscopic diagnostic tool for electric field measurements in IShTAR (Ion cyclotron Sheath Test ARrangement)," Rev. Sci. Instrum., vol. 89, no. 10, 2018.

I. Shesterikov et al., "IShTAR: A test facility to study the interaction between RF wave and edge plasmas," Rev. Sci. Instrum., vol. 90, no. 8, p. 083506, Aug. 2019.

Conference Paper

A. Kostic et al., ”Direct local electric field measurements in the sheaths of the ICRF antenna in IShTAR,” AIP Conference Proceedings, 2254, 050002 (2020).

A. Kostic et al., "Feasibility study of passive optical emission spectroscopy for the electric field measurements in IShTAR," EPJ WEB OF CONFERENCES, vol. 157, 2017.

K. Crombé et al., ”Plasma operation and electric field measurements in IShTAR,” 46th EPS Conference on Plasma Physics, EPS 2019, 2019, pp. 1-4.

K. Crombé et al., ”New diagnostics developments on IShTAR,” 45th EPS Conference on Plasma Physics, EPS 2018, 2018,pp. 1001-1004.

J.-M. Noterdaeme et al., ”Ion cyclotron range of frequency power: progress in operation and understanding for experiments with metallic walls,” 27th IAEA Fusion Energy Conference - IAEA CN-258, Gandhinagar, India, 2018, vol. IAEA CN-258.

K. Crombé et al., ”Helium operation of IShTAR in preparation of E-field measurements,” 44th EPS Conference on Plasma Physics, EPS 2017, 2017, pp. 3-6.

R. D’Inca et al., ”Characterization of the RF plasma in ISHTAR,” 43rd European Physical Society Conference on Plasma Physics, EPS 2016, 2016, pp. 4-7.

Master Thesis

T. Verstrynge, and Kristel Crombé, "Spectroscopic Diagnostics of Ishtar Plasma," A dissertation submitted in partial fulfilment of the requirements for the degree of Master in Physics and Astronomy, Ghent University Faculty of Science Department Physics and Astronomy, 2018.

Book Chapter

K. Crombé et al., "A Test Facility to Investigate Sheath Effects during Ion Cyclotron Resonance Heating," in Plasma Science and Technology - Basic Fundamentals and Modern Applications, Dr. Haikel Jelassi and Dr. Djamel Benredjem, Ed. IntechOpen, 2019, pp. 1-10.